HYD-48

ENERGY

DOE/ERA/HOT

COO-4434-14

ASSESSMENT OF THERMOCHEMICAL HYDROGEN PRODUCTION

Final Report, July 1, 1977—March 31, 1979

By
James R. Dafler
Stephen E. Foh
Tien S. Lee
James D. Schreiber

May 1979
Date Published

Work Performed Under Contract No. EC-77-C-02-4434

Institute of Gas Technology
IIT Center
Chicago, Illinois

U. S. DEPARTMENT OF ENERGY

Division of Energy Storage Systems

(6)

NOTICE

COO-4434-14
Distribution Category UC-94d

ASSESSMENT OF THERMOCHEMICAL HYDROGEN PRODUCTION

Project 61010 (Formerly 8994) Final Report

For the Period July 1, 1977, Through March 31, 1979

James R. Dafler
Stephen E. Foh
Tien S. Lee
James D. Schreiber

Prepared by
Institute of Gas Technology
IIT Center, 3424 S. State Street
Chicago, Illinois 60616

Date Published — May 1979

Prepared for the

UNITED STATES DEPARTMENT OF ENERGY

Under Contract No. EC-77-C-02-4434

EXECUTIVE SUMMARY

This report describes the work done at the Institute of Gas Technology (IGT) to assess thermochemical water-splitting processes. A total of eight tasks were performed under Contract No. EC-77-S-02-4434, including modifications A001 and A002. This program began in July 1977, was continued in March 1978, and was completed in March 1979.

Engineering analyses were done on two thermochemical hydrogen production cycles — IGT's Cycles B-1 and H-5. A load-line efficiency was calculated for these cycles to assess the efficiency of use of thermal energy from a primary source. The analyses and assessments were based on engineering and process unit operations representative of current technology.

For Cycle B-1 —

$$3FeCl_2(\ell) + 4H_2O(s) \rightarrow Fe_3O_4(s) + 6HCl(g) + H_2(g)$$

$$Fe_3O_4(s) + 8HCl(g) \rightarrow 2FeCl_3(s) + FeCl_2(s) + 4H_2O(g)$$

$$2FeCl_2(s,g) \rightarrow 2FeCl_2(s) + Cl_2(g)$$

$$Cl_2(g) + H_2O(g) \rightarrow 2HCl(g) + \tfrac{1}{2}O_2(g)$$

the load-line efficiency was 18.1%, which is in agreement with a similar result from the EURATOM Community Laboratories. For Cycle H-5 —

$$CuO(s) + SO_2(g) + 6H_2O(\ell) \rightarrow CuSO_4 \cdot 5H_2O(s) + H_2(g)$$

$$CuSO_4 \cdot 5H_2O(s) \rightarrow CuSO_4(s) + 5H_2O(g)$$

$$CuSO_4(s) \rightarrow CuO(s) + SO_3(g)$$

$$SO_3(g) \rightarrow SO_2(g) + \tfrac{1}{2}O_2(g)$$

the load-line efficiency was 37.4%.

The engineering analyses were based on energy and enthalpy balances for rationally designed flowsheets. Iterations based on unit process improvements were not done. Cycle B-1 is, overall, a complex process with energy-intensive gas-phase separations, while Cycle H-5 is much simpler, having far fewer gas-phase separations, overall, than Cycle B-1. Flowsheet iterations based on unit operation improvements and incorporating improved rate data will

certainly increase the calculated load-line efficiencies of both cycles. However, Cycle H-5 has a far more attractive baseline efficiency, and, of the two cycles, would be far more promising for future development.

The electrolysis of HBr(aq) on three substrates — platinum, porous graphite, and vitreous graphite — was investigated. This electrolysis is the hydrogen production step of a cycle under intense development at the EURATOM Laboratories.

In the studies reported here, platinum proved to be the most efficient electrode surface, with vitreous graphite showing no promise, and porous graphite showing only slightly better results. On platinum, cell voltages of under 1.0 volt were obtained at current densities up to 200 mA/cm^2.

This research also indicates that cathode polarization effects appear to be paramount. When an extended platinum cathode (at very low current) was used in conjunction with a platinum anode, the cell voltage, in stirred 47.5% HBr at 200 mA/cm^2 (at the anode), was less than 0.200 volt.

Using a formal methodology developed at IGT, the maximum attainable efficiency for the EURATOM Mark-13 cycle was calculated. This hybrid cycle —

$$SO_2(g) + Br_2(g) + 2H_2O(g) \rightarrow H_2SO_4(\ell) + 2HBr(g)$$

$$2HBr(g) \rightarrow H_2(g) + Br_2(\ell) \qquad \text{(electrolysis)}$$

$$H_2SO_4(g) \rightarrow H_2O(g) + SO_2(g) + \tfrac{1}{2}O_2(g)$$

generates hydrogen by electrolyzing HBr(aq), which is also the subject of this report. The calculation of the maximum attainable efficiency estimates the attainable upper limit of efficiency for the cycle treated and is based on conservative assumptions for heat use and equilibrium thermodynamics.

For current technology (attainment of 50% of Carnot efficiency for heat-to-work processes), the maximum attainable efficiency was 37.1%. For future technology (67% of Carnot efficiency for heat-to-work processes), the value for the maximum attainable efficiency was 44.1%.

The electrolytic oxidation of sulfurous acid (H_2SO_3) to sulfuric acid (H_2SO_4) and hydrogen is a step in the copper oxide-copper sulfate cycle, H-5. We measured the potentials of the half-cell reactions —

$$H_2SO_3 + H_2O \rightarrow H_2SO_4 + 2H^+ + 2e^- \quad \text{(positive electrode)}$$

$$2H^+ + 2e^- \rightarrow H_2 \quad \text{(negative electrode)}$$

as functions of sulfuric-acid concentration and impressed current in electrolyte saturated with SO_2 and compared with conventional water electrolysis (SO_2-free electrolyte). At the positive electrode, half-cell potential was measured at current levels up to 500 mA in 8%, 19%, 33%, and 50% (by weight) sulfuric-acid solutions. In all cases, the potential difference between the SO_2-free and SO_2-saturated solutions is about 1.3 volts. The potential of the positive electrode in SO_2-saturated solutions becomes less positive as the sulfuric-acid concentration decreases from 50% to 8%, although sulfur production in 8% H_2SO_4 indicates that side reactions may impose a lower limit on H_2SO_4 concentration. We calculated the Tafel slopes for the anodic oxidation of SO_2. In 8%, 19%, and 33% H_2SO_4, the Tafel slopes are all 88 mV per decade of applied current. In 50% H_2SO_4, the slope is much larger, 185 mV per decade, indicating that the half-cell reaction in concentrated acid is more complex. It appears that the optimum sulfuric-acid concentration is between 8% and 50%, but to determine a more exact optimum, more data are required.

Five new members of the metal-metal oxide class of cycles were derived. The maximum attainable efficiencies of these high-temperature, two-step cycles range from 64% to 86%. These cycles are based on such materials as zinc oxide, tin oxide, iron oxide, and manganese oxide. These cycles should be capable of producing hydrogen at elevated pressures to avoid or minimize the cost penalty for compression to pipeline pressures.

Six high-temperature metal oxide-metal sulfate cycles were derived. These cycles were ranked according to the relative solubilities of the sulfate and oxide species in water and by the degree to which the sulfate will form stable hydrates. The hydrogen-producing steps in all six (hybrid) cycles can be driven electrochemically (presumably in aqueous electrolytes). Therefore, the relative solubilities of the metal sulfate (product) and metal oxide

(reactant) species are important: The solubility ratio of product to reactant should be as low as possible. Because the quantity of heat required to dehydrate a metal sulfate is directly proportional to the degree of hydration, the sulfates that form lower order hydrates are attractive. Based on these criteria, a strontium oxide-strontium sulfate cycle and a calcium oxide-calcium sulfate cycle appear to be the most attractive candidates for further development. The maximum attainable efficiencies of these cycles range from 40% to 44% if their hydrogen-producing steps are run electrochemically at ambient temperature. If the hydrogen-producing steps of these two cycles are thermally driven at higher temperature, their maximum attainable efficiencies are much more attractive: 67% to 74%.

We tabulated performance and capital costs data for a wide range of solar primary heat sources. Solar heat source designs of both the nontracking (flat plate and evacuated tube, capable of producing low-to-medium temperatures) and tracking (parabolic dish and central receiver, capable of producing medium-to-high temperatures) were analyzed. The capital costs obtained for solar heat sources are at least three times greater than those for high-temperature nuclear designs, on a cost per thermal capacity basis. (However, the solar cost estimates were obtained for designs that are roughly an order of magnitude smaller in thermal capacity than the nuclear designs.)

Economies-of-scale may narrow the difference between solar and nuclear heat costs as larger solar capacities are considered. Also, high-temperature solar technology is quite immature in its current state, and relative cost improvements are likely as that technology develops. Overall, we expect capital cost requirements for solar primary heat sources to drop, but when or whether they will become competitive with nuclear capital costs cannot be predicted at this time.

A promising, high-temperature strontium oxide-strontium sulfate cycle, Z-33, was derived in 1978. The temperature that thermodynamics data predicts is required to decompose strontium sulfate (> 2000 K) is above the maximum temperature achievable in our laboratory furnaces (1775 K). Therefore, we were not able to directly test the workability of this step in Cycle Z-33. Instead, we measured the rate of decomposition of $SrSO_4$ at temperatures up to

1775 K and extrapolated that data to indirectly determine workability at 2000 K. We conclude that this step is workable at the temperature predicted by thermodynamics data.

TABLE OF CONTENTS

TABLE OF CONTENTS, Cont.

LIST OF FIGURES

LIST OF FIGURES, Cont.

LIST OF TABLES

LIST OF TABLES, Cont.

TASK 1. EVALUATION OF LOAD-LINE EFFICIENCIES

We investigated, in conceptual process form, the operating conditions and energy consumption for the Institute of Gas Technology's Cycles B-1 and H-5. Cycle B-1 is IGT's most developed cycle, one that is fully demonstrated with recycled materials and for which reaction rates, measured with recycled reactant materials, are known. Cycle H-5, although likewise demonstrated, is newer and less developed, but is more promising in terms of energy efficiency and practical operability. The flowsheet for the conceptualized processes of Cycles B-1 and H-5 have been completed, and the load-line efficiencies* have been calculated. For the individual steps of both cycles, we have used operating conditions indicated as workable by laboratory experiments(with some extrapolations to high pressures).

We wish to emphasize that the engineering and process unit operations for these cycles are based on current technology and state-of-the-art practices in the chemical process industry. These operations (and the processes) could be improved, through appropriate research, to require the consumption of less energy. Additionally, the processes of these cycles might be made more energy-efficient directly through further laboratory experiments to define more favorable operating conditions.

Cycle B-1

Cycle B-1, represented by Reactions 1 through 4,

$$3FeCl_2(\ell) + 4H_2O(g) \rightarrow Fe_3O_4(s) + 6HCl(g) + H_2(g) \quad (1)$$

$$Fe_3O_4(s) + 8HCl(g) \rightarrow 2FeCl_3(s) + FeCl_2(s) + 4H_2O(g) \quad (2)$$

$$2FeCl_3(s,g) \rightarrow 2FeCl_2(s) + Cl_2(g) \quad (3)$$

$$Cl_2(g) + H_2O(g) \rightarrow 2HCl(g) + 1/2\ O_2(g) \quad (4)$$

is the most developed thermochemical water-splitting cycle in the IGT research program, and it is one of the published cycles that has been demonstrated in the laboratory.[1] Rates of the pertinent reactions have been measured at IGT, and reactor volume requirements for good conversions are reasonable. The next step in the assessment of a water-splitting process is to prepare a process

---

* The load-line efficiency is the efficiency of use of the prime heat energy from the energy source (the coolant stream of a nuclear HTR or a combination of solar furnace heat and coolant stream heat).

flowsheet to identify portions of the process that will benefit most from concentrated research and development efforts.

We developed the flowsheet for Cycle B-1 using the following guidelines:

- Process heat is supplied by the intermediate (secondary) coolant stream from a very high temperature nuclear reactor (VHTR), in which the primary coolant temperature cascades from 1200 to 700 K (1700° to 800°F). Additional higher temperature heat may be supplied by a solar collector that supplies isothermal heat at 1350 K (1970°F).

- In heat exchangers, a minimum temperature difference of 50 K (90°F) is required between heating and cooling streams. The highest temperature attainable in the process is then 1150 K (1610°F) from the VHTR, and 1300 K (1880°F) from a solar source.

- Cooling water is available at 298 K (77°F).

- No heat is lost to the environment except that which is removed by the cooling water.

- In laboratory studies at IGT, near-equilibrium conversions had been obtained from Reactions 1, 2, and 4, (page 1) so we assumed equilibrium conversions for these reactions in the Cycle B-1 flowsheet. Because of the low equilibrium conversions from Reaction 3, reaction conditions far from equilibrium have been studied at IGT, and for the process flowsheet, we use the highest conversion found at IGT.

A process designed to produce hydrogen for pipeline transmission at 50 to 100 atm must yield hydrogen at pressure to avoid capital and energy penalties[2] for compression to transmission levels.[3] Cox[4] has calculated the cost of compression to 50 atm as a function of compression ratio for various electrical costs (Figure 1). The trade-off for operating Reaction 1 at elevated pressure is shown in Figure 2, which is a plot of the equilibrium H_2O/H_2 product mole ratio versus temperature for pressures up to 100 atm. On the basis of this plot, we chose an operating pressure of 30 atm for the hydrogen-producing reaction. This operating pressure represents a compromise between transmission-level pressures that require high mass fluxes and low pressures with low mass fluxes, but with high compression cost.

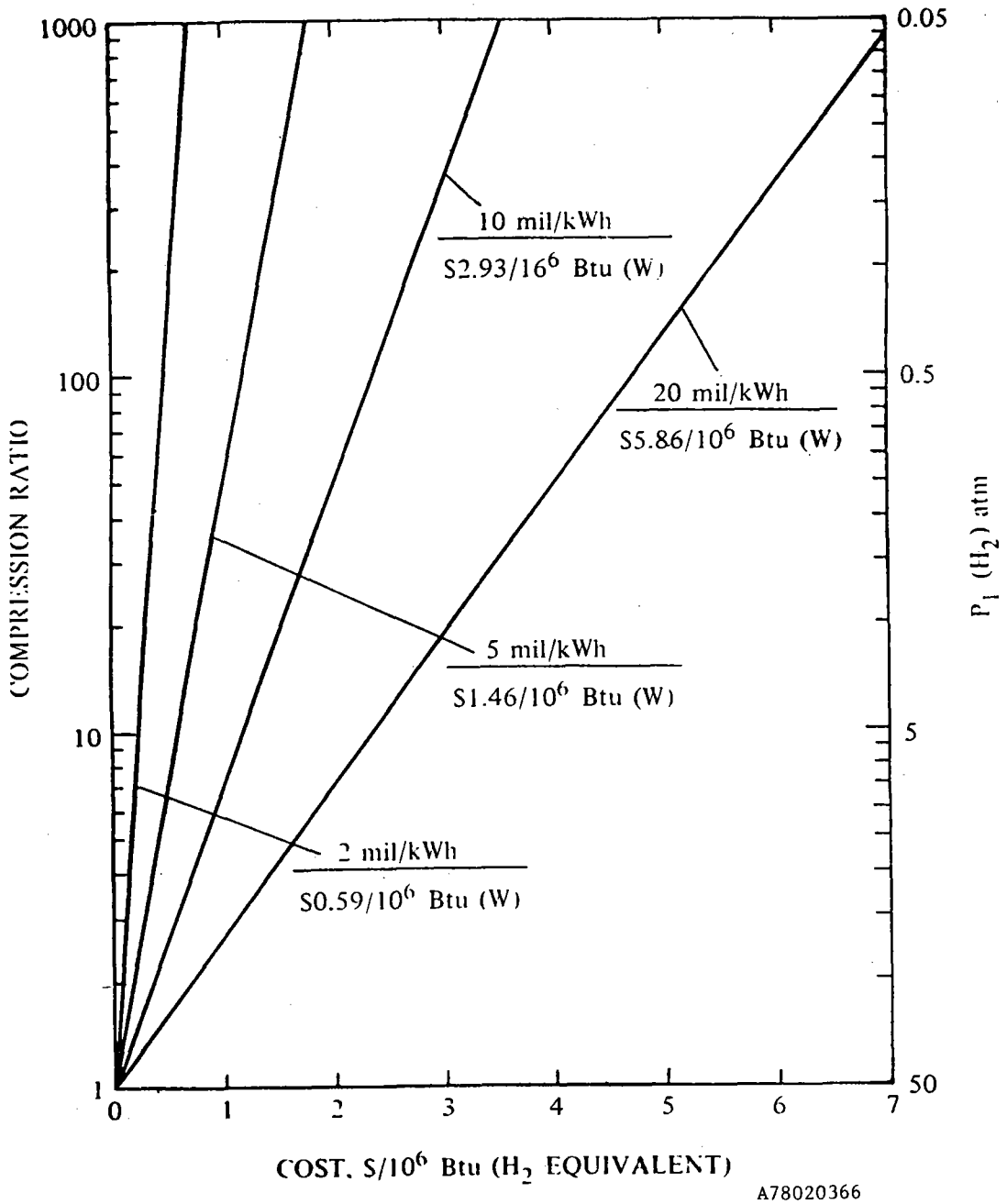

Figure 1. COST OF HYDROGEN COMPRESSION [4]
This figure allows the estimation of compression costs for pipeline injection if electrical power costs can be assumed.

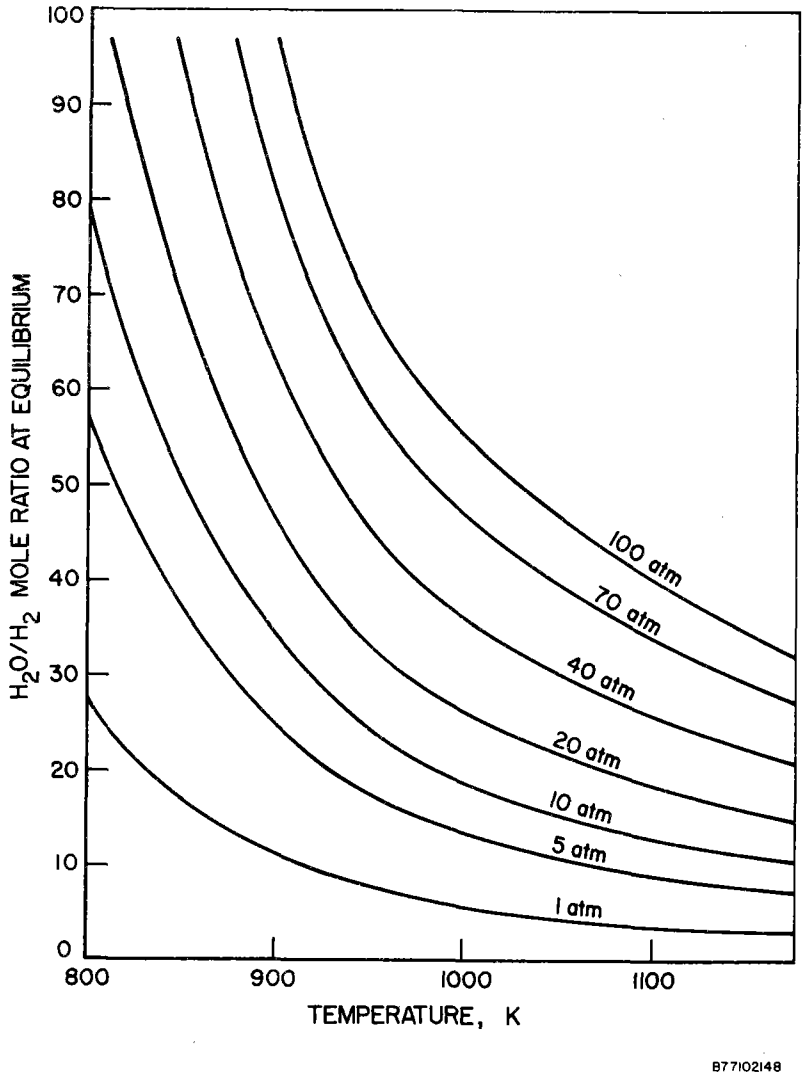

Figure 2. FERROUS CHLORIDE-STEAM REACTION: EQUILIBRIUM H_2O/H_2 MOLE RATIO AS A FUNCTION OF TEMPERATURE (HCl/H_2O Feed Ratio = 0.00)

Only significant pressure changes have been taken into account; these are indicated in the modified, finished flowsheet by pump, turbine, and valve symbols. Such details as control valves and equipment needed for transporting fluids and solids have been omitted because they would have very little effect on the load-line efficiency. In determining the inlet and outlet temperatures and pressures, we assumed that pumps, compressors, and turbines operate isentropically and expansion valves operate isenthalpically. We then calculated the actual shaft work for compression and pumping as 1.25 times the isentropic

work required (that is, the pumps and compressors are 80% efficient). The amount of shaft work obtained by expansion through turbines was calculated as 80% of the isentropic (or ideal) work obtained from them. When work has to be generated from heat, we assumed the efficiency of the conversion to be two-thirds of the Carnot efficiency.

Although the oxygen produced by the process could possibly be marketed, we assumed in the conceptualized process that it is simply vented to the atmosphere.

Many of the materials used in this process, HCl for example, are highly corrosive. We did not consider the problem of corrosiveness here; instead, we determined the conditions under which the process produced the highest yield of hydrogen while requiring the least amount of energy.

All mass flows and energy requirements reported here are based on the production of one gram-mole of hydrogen.

Base-Case Flowsheet

We prepared a base-case flowsheet for Cycle B-1 designed to show those areas requiring the most research effort. The base-case scheme was kept as simple as possible by assuming atmospheric-pressure reaction conditions and 298 K ($77^{\circ}F$), 1-atm, condensed-phase separations of all HCl-H_2O gas mixtures. Figure 3 is a schematic diagram of the flowsheet, and Table 1 provides a summary of molar flow rates based on the production of 1 gram-mole of hydrogen.

A large part of the process shown in Figure 3 involves separations. The gaseous products of Reaction 1 enter condenser C-1, where the water is condensed. HCl is absorbed by the water to form a saturated solution at 298 K and 1 atm, containing 25.9 mole percent HCl. This condensate, stream 2, is combined with similar solutions from scrubbing towers T-1 and T-2 and condenser C-3 and fed to the distillation column, D-1. The gaseous stream leaving C-1, stream 3, contains H_2 in the gas phase.

The distillation column D-1, operating at atmospheric pressure, produces a distillate containing 95 mole percent HCl (stream 5), which is fed to Reaction 2, and the bottoms, having the azeotropic composition of 11.1 mole

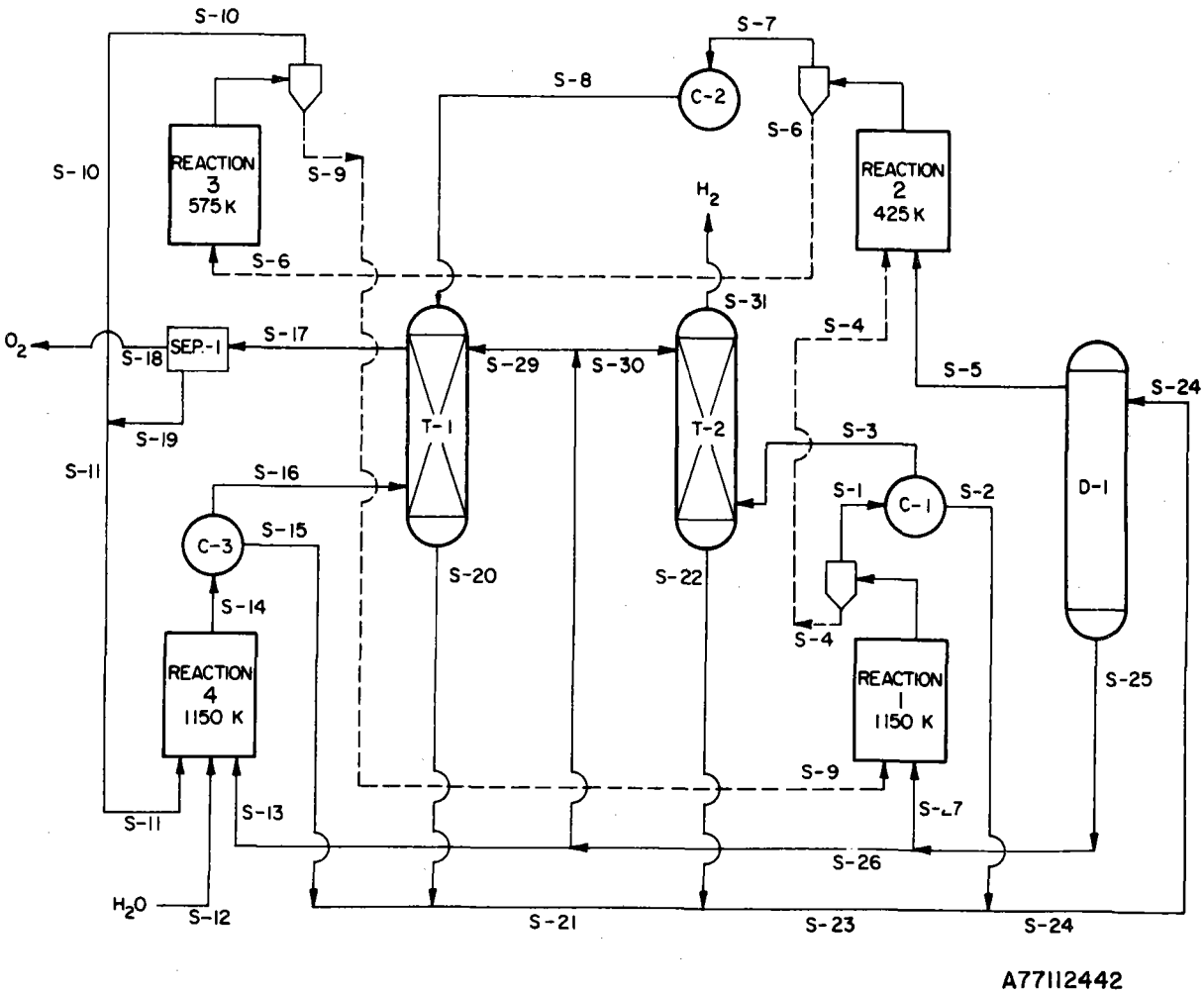

Figure 3. SCHEMATIC DIAGRAM OF THE BASE-CASE FLOWSHEET FOR CYCLE B-1

Table 1. MOLAR FLOW RATES FOR THE CYCLE B-1 FLOWSHEET (Shown in Figure 3)

Stream	Composition, moles		Temperature at Source, K
S-1	1 H_2	(g)	1150
	6.942 HCl	(g)	
	3.535 H_2O	(g)	
S-2	3.535 H_2O	(ℓ)	298
	1.233 HCl	(aq)	
S-3	1 H_2	(g)	298
	5.709 HCl	(g)	
S-4	1 Fe_3O_4	(s)	1150
S-5	9.036 HCl	(g)	333
	0.476 H_2O	(g)	
S-6	2 $FeCl_3$	(s)	425
	1 $FeCl_2$	(s)	
S-7	4.476 H_2O	(g)	425
	1.036 HCl	(g)	
S-8	4.476 H_2O	(ℓ)	298
	1.036 HCl	(aq)	
S-9	3 $FeCl_2$	(s)	575
S-10	1 Cl_2	(g)	575
S-11	1.067 Cl_2	(g)	~575
S-12	1 H_2O	(ℓ)	298
S-13	3.270 H_2O	(ℓ)	381
	0.409 HCl	(aq)	
S-14	0.50 O_2	(g)	1150
	0.0675 Cl_2	(g)	
	2.409 HCl	(g)	
	3.270 H_2O	(g)	
S-15	3.270 H_2O	(ℓ)	298
	1.141 HCl	(aq)	
S-16	0.50 O_2	(g)	298
	0.0674 Cl_2	(g)	
	1.268 HCl	(g)	

A78020359

Stream	Composition, moles		Temperature at Source, K
S-17	0.50 O_2	(g)	298
	0.0674 Cl_2	(g)	
S-18	0.50 O_2	(g)	298
S-19	0.0674 Cl_2	(g)	298
S-20	7.791 H_2O	(ℓ)	298
	2.718 HCl	(aq)	
S-21	11.016 H_2O	(ℓ)	298
	3.859 HCl	(aq)	
S-22	25.496 H_2O	(ℓ)	298
	8.896 HCl	(aq)	
S-23	36.557 H_2O	(ℓ)	298
	12.755 HCl	(aq)	
S-24	40.092 H_2O	(ℓ)	298
	13.988 HCl	(aq)	
S-25	39.616 H_2O	(ℓ)	381
	4.952 HCl	(aq)	
S-26	32.081 H_2O	(ℓ)	381
	4.010 HCl	(aq)	
S-27	7.535 H_2O	(ℓ)	381
	0.942 HCl	(aq)	
S-28	28.811 H_2O	(ℓ)	381
	3.601 HCl	(aq)	
S-29	3.315 H_2O	(ℓ)	298
	0.414 HCl	(aq)	
S-30	25.496 H_2O	(ℓ)	298
	3.187 HCl	(aq)	
S-31	1 H_2	(g)	298

A78020360

percent HCl (stream 25). The still bottoms are used as feed to Reactions 1 and 4 and as the scrubbing medium in scrubbers T-1 and T-2.

The gaseous products of Reaction 2 are condensed in C-2 to form a dilute $HCl-H_2O$ solution, which is then used as a scrubbing medium (along with a portion of the still bottoms, stream 29) in T-1.

Both scrubbers T-1 and T-2 operate at 298 K and 1 atm. The liquid streams leaving T-1 and T-2, streams 20 and 22, are both saturated $HCl-H_2O$ solutions, containing 25.9 mole percent HCl.

The $FeCl_2$-$FeCl_3$ product stream from Reaction 2, stream 6, is fed to Reaction 3, assumed for the base-case flowsheet to go to completion. The solid product, $FeCl_2$, is fed to Reaction 1 via stream 9. The Cl_2, in stream 10, is fed to Reaction 4.

Water is introduced into the process as feed to Reaction 4 (stream 12). The products of Reaction 4 enter condenser C-3 where a saturated $HCl-H_2O$ solution is formed (stream 15). The gaseous stream leaving C-3, stream 16, contains O_2, Cl_2, and HCl. The HCl is scrubbed in T-1, leaving a stream (17) containing O_2 and Cl_2, which are separated in an undefined separation scheme, SEP-1. The Cl_2 (stream 19) is combined with stream 10 and recycled to Reaction 4. The O_2 is vented to the atmosphere.

The bulk of the process, then, involves constant recycling of two types of aqueous HCl streams: 1)the still bottoms, which contain 11.1 mole percent HCl (azeotrope), and 2) the condenser and scrubbing tower effluents, which are saturated (25.9 mole percent HCl) at 298 K ($77^{\circ}F$) and 1 atm.

Table 1 indicates that the mass fluxes for the base case are too large to be practical. The dominant factors are 1) the aqueous HCl liquid streams involved in the H_2O-HCl separation, mixed to form stream 24; and 2) the large quantities of excess steam required for Reaction 1. An enthalpy balance around the base-case flowsheet has identified the largest internal heat-transfer burdens. The largest contributor to this load is the distillation of liquid at D-1. Since the need for major revisions to the base case was apparent from the rather substantial heat and mass-transfer requirements, we did not determine a load-line efficiency.

Analysis of the base-case flowsheet identified the two areas that will most benefit from intensive engineering analysis: the $HCl-H_2O$ separation scheme and the steam-rich conditions for the $FeCl_2$ hydrolysis (H_2-production) reaction. Particularly troublesome is the $HCl-H_2O$ azeotrope in liquid stream 25 because the presence of 11.1 mole percent HCl increases the heat and the mass fluxes in two ways: 1) It limits the absorption capacity of the scrubbing solution, and 2) it adversely affects the equilibria of Reactions 1 and 4, thereby increasing their feed requirements.

Modifications to the Base Case

We investigated physical adsorption and pressurized distillation as alternative $HCl-H_2O$ separation schemes. Molecular sieves are definitely not compatible with the acidic nature of our $HCl-H_2O$ streams. While silica gel will absorb water in the presence of HCl, it desorbs at temperatures around 425 K (305°F); we would not be able to avoid the large temperature swings that account for about half the heat load of the condensed-phase separation scheme. Furthermore, the heat of absorption (or desorption) of H_2O on silica gel is about 50% greater than the heat of vaporization of H_2O. It appears that the efficiency of a process using silica gel to effect the separation of HCl and H_2O would be less than the efficiency of the base-case condensed-phase separation.

Other absorbents suffer from similar faults, all requiring fairly low temperatures for efficient absorption. Although activated carbon is unusual in that the heat of absorption of H_2O is less than the heat of vaporization of H_2O, it absorbs insignificant quantities of H_2O.

At elevated pressures the mole fraction of HCl in the azeotrope is reduced and the heat of vaporization of H_2O drops. Figure 4 is a plot of mole fraction HCl in the azeotrope as a function of system pressure. At 70 atm, the azeotrope contains less than 1 mole percent HCl as compared with 11.1 mole percent at 1 atm; in addition, the heat of vaporization of H_2O is about 66% of its value at 1 atm. However, the work done in raising the pressure from 1 to 70 atm is equal to the savings in latent heat (34%), so if only the distillation were carried out at 70 atm while the rest of the process remained at 1 atm, there would be no reduction in the heat required for the separation of HCl and H_2O. But as long as a major portion of the process operates at high pressure, the heat requirements to effect a given degree of separation will be

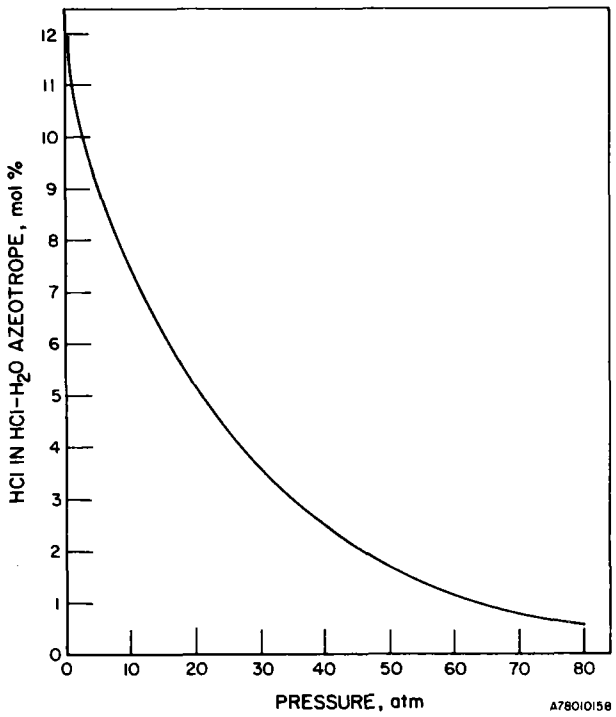

Figure 4. $HCl-H_2O$ AZEOTROPE COMPOSITION AS A FUNCTION OF PRESSURE

less at high pressures. Because a more complete separation of the $HCl-H_2O$ stream is possible at elevated pressures, high-pressure distillation reduces the required heat and mass flow rates for the overall process.

Pressurized operation of all reactions of Cycle B-1 was studied to determine effects on equilibrium yields. The yields from Reaction 2 are increased by pressure. The low operating temperature [about 475 K (395°F)], however, limits to about 15 atm the pressure at which the reaction may be operated without condensing the steam. For hydrolysis of $FeCl_2$ (Reaction 1), the equilibrium mole fraction of hydrogen falls off rapidly with increasing pressure. Since HCl is a product of Reaction 1, its presence as an impurity in the feed lowers the fraction of hydrogen in the product. As indicated earlier, we have used a pressure figure of 30 atm for H_2 production. Although the effect of producing H_2 is minimized by the purer feed available from pressurized distillation, higher temperature process heat is required than is available from a VHTR. The maximum equilibrium mole fraction of H_2 is obtained at about

1300 K (1880°F). To operate at this temperature, Reaction 1 requires a process heat "assist" from a solar source.

The major modifications to the base case, then, are 1) operation of the hydrogen-producing step (Reaction 1) at 30 atm and 1300 K (1880°F) instead of 1 atm and 1150 K (1610°F); 2) operation of Reaction 2 at 15 atm and 475 K (395°F) instead of 1 atm and 425 K (305°F); and 3) distillation of HCl-H_2O mixtures at 70 atm instead of 1 atm, giving bottoms containing 1 mole percent HCl and distillate containing 99.5 mole percent HCl. In addition, a scheme was devised for separating the large amounts of dimer [Fe_2Cl_6(g)] from Cl_2(g) and recycling the Fe_2Cl_6. Also, details of the separation of Cl_2 and O_2, indicated in the base-case flowsheet, Figure 3, by the "black box," SEP-1, were developed.

The Modified Flowsheet

As in the base case, the process in its final form (Figure 5) consists of the four reactions and various schemes for separating and recycling the products of each reaction, with the separations making up the bulk of the process.

Hydrogen is separated from the gaseous product from Reaction 1 (stream 1) by cooling the stream to 343 K (158°F) and condensing the H_2O in C-1. The HCl is absorbed by the water to form a saturated solution of HCl in H_2O, thereby removing both HCl and H_2O from the gaseous phase. (Since the hydrogen produced by this process must be essentially pure, the stream will actually require further cleaning to remove residual H_2O and HCl.)

The HCl solution from condenser C-1 is combined with similar solutions from scrubbing tower T-1 and condenser C-6 in mixer M-2, compressed to 70-atm pressure at P-5, and fed to the distillation column D-1.

The bottoms from D-1, stream 39, containing 1 mole percent HCl, are passed through turbine V-1 to extract work while reducing the pressure to 30 atm. A portion of the liquid in the stream is flashed into vapor as it passes through the turbine. This vapor and the bulk of the remaining liquid are fed to boiler H-1, where the liquid is boiled, and the vapors are heated to 1300 K (1880°F) before being fed to Reaction 1 ($FeCl_2$ hydrolysis).

The remainder of the still bottoms, stream 41, is passed through another turbine, V-3, to reduce the pressure to 1 atm. The vapor-liquid mixture is heated to 1150 K (1650°F) in H-2 and fed to Reaction 4 (Reverse Deacon Reaction).

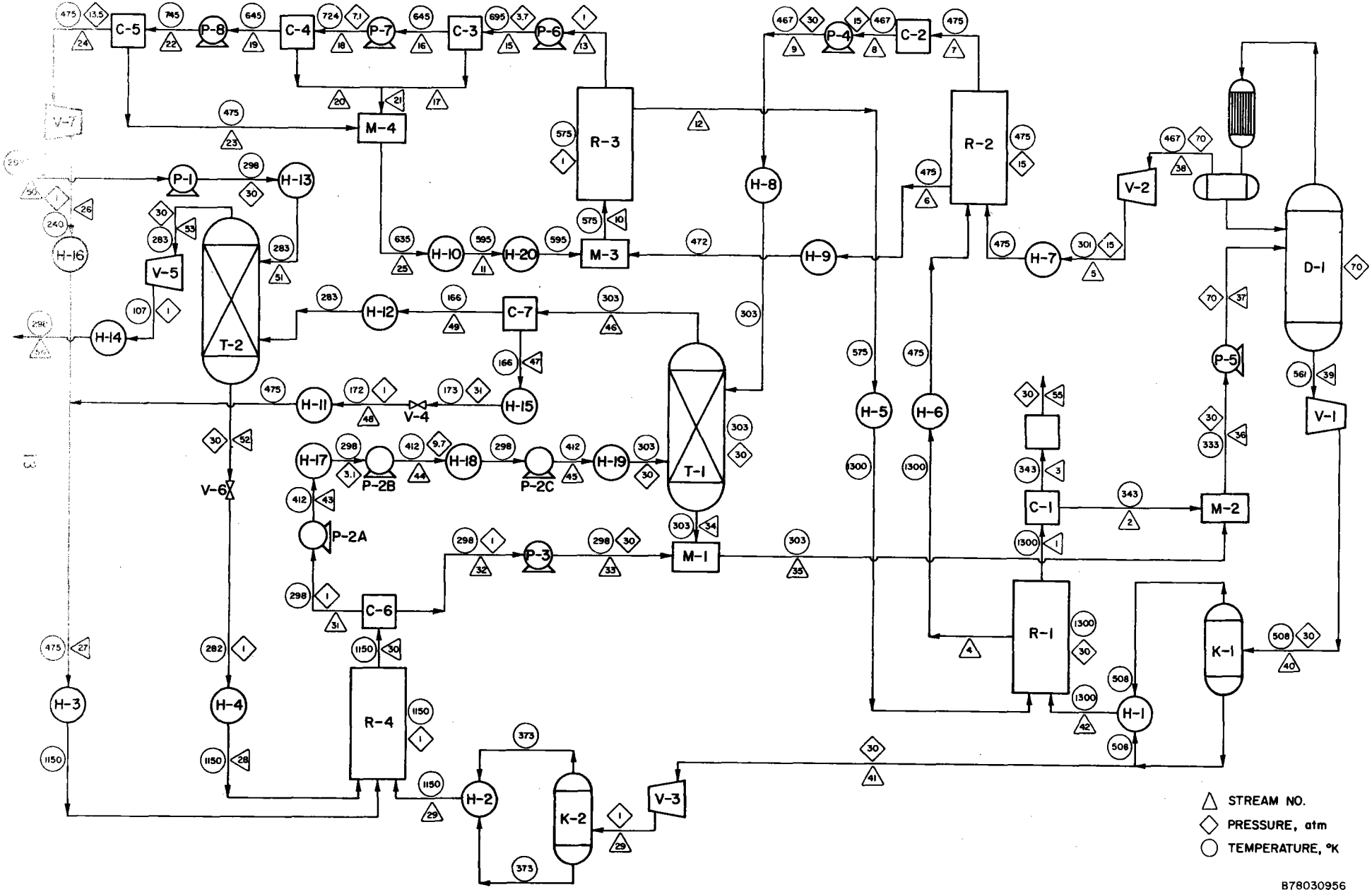

Figure 5. FINAL FLOWSHEET FOR CYCLE B-1

While virtually anhydrous HCl can be obtained from a still operated at 70 atm, we specified a more conservative distillate concentration of 99.5 mole percent HCl. The distillate is passed through turbine V-2 to extract work while reducing the pressure to 15 atm. In doing so, the temperature of the distillate drops from 467 to 301 K (381° to 82°F), and it must be reheated in H-7 to 475 K (395°F) before being fed to Reaction 2. The gaseous products of Reaction 2 are condensed to form a dilute HCl-H_2O solution, which, after being pumped up to 30 atm pressure at P-4 and cooled to 303 K (865°F) in H-8, is used in scrubber T-1 to remove the HCl remaining in the gaseous product stream from Reaction 4.

The solid products of Reaction 2 in stream 6, consisting of 2 moles of $FeCl_3$ and 1 mole of $FeCl_2$, are sent to Reaction 3, where the $FeCl_3$ is decomposed to $FeCl_2$ and Cl_2. The decomposition is complicated by the formation of a stable gaseous dimer, Fe_2Cl_6. At 1-atm pressure, the equilibrium ratio of Fe_2Cl_6 to Cl_2 is about 18; however, laboratory studies at IGT have shown it is possible to reduce this ratio to about 9. This value was used rather than the equilibrium ratio. Recycling of the Fe_2Cl_6 involves condensation to form solid $FeCl_3$, separation of the solid from the gaseous Cl_2, and resublimation of the $FeCl_3$ to form Fe_2Cl_6. Since the condensation and sublimation both involve large amounts of heat, it is desirable to use the heat of condensation in the sublimation step. A scheme was devised in which the gaseous mixture of Cl_2 and Fe_2Cl_6 is alternately compressed and cooled, the cooling being done at a sufficiently high temperature that the heat released as the Fe_2Cl_6 condenses (and separates from gaseous Cl_2) can be used to sublime $FeCl_3$ at 1-atm pressure. It is necessary for the condensation to be done under pressure to maintain the minimum temperature difference (ΔT_m) across the heat exchangers [a difference of 50 K (90°F)]. Then all of the heat of condensation of Fe_2Cl_6 (282.2 kcal) is used directly to sublime all the excess $FeCl_3$ to be used in Reaction 3 at the expense of 51.4 kcal of compressor work.

After the third compressor stage in this scheme, the pressure is 13.5 atm; after cooling to 475 K (395°F) in C-5, all the Fe_2Cl_6 is condensed, and the Cl_2 is then passed through turbine V-7, giving back some of the compression work and cooling the Cl_2 to 240 K (−27°F) at 1 atm. Combined with the Cl_2 separated from O_2, this stream is heated to 1150 K (1610°F) in H-3 and fed to Reaction 4.

The products of Reaction 4 are cooled to 298 K (77°F) in C-6, condensing the H_2O, which is saturated with HCl. This solution eventually finds its way to the still. The remaining gaseous stream, containing HCl, O_2, and Cl_2, is compressed and cooled in three stages to 30 atm and fed to the scrubber T-1, where HCl is scrubbed. The remaining gas mixture of O_2 and Cl_2 is cooled to 166 K (−161°F), freezing out all except 0.001 g-mole of Cl_2. The solid chlorine is melted, and after reducing the pressure to 1 atm, the chlorine is boiled and combined with the Cl_2 from Reaction 3. The O_2 containing the trace of Cl_2 is warmed to 298 K (77°F) and scrubbed with the process feed water in T-2 to remove the Cl_2. Chlorinated H_2O is then decompressed, boiled, and fed to Reaction 4. The O_2 is passed through a turbine, reducing its pressure to 1 atm and temperature to 107 K (−267°F). It is reheated to 298 K (77°F) and vented as waste product.

In spite of our modifications to the base case, the molar flow rates are still large. Again, this is due primarily to the large quantities of excess steam required for Reaction 1. Since it is necessary to produce the hydrogen at a minimum of 30 atm pressure, while the feed stream is nearly pure and the operating temperature such that excess steam requirements are minimized, nothing can be done to reduce the mass flux in this portion of the process without increasing the work requirements for compressing H_2.

Although the molar flow rate through the still is less now than in the base case, the heat load is greater because of the higher degree of separation. It is now the heat of solution of HCl in H_2O, rather than the heat of vaporization of H_2O, that accounts for the bulk of the heat requirements of the still.

The largest contributor to the total process heat requirement is Reaction 3. Less than a third of the 51 kcal of compressor work required for recycling Fe_2Cl_6 is available from work recovered within the process. The rest must be generated from heat, a process that is at most 49% efficient even when high-temperature solar heat is used. A total of 112 kcal of heat at 1300 K (1880°F) is needed to generate the work used by this process, most of which is consumed in recycling Fe_2Cl_6.

Load-Line Efficiency Calculation

In performing an enthalpy balance around the final flowsheet, the operating conditions and heat load of each unit in the process was determined. To check

the accuracy of the enthalpy balance, the hydrogen was converted to its reference state [298 K (77°F), 1 atm]. The ideal pump and compressor work requirements were added to the total heat requirement, giving a value of 978.861 kcal, and the ideal work made available from turbines was added to the total amount of heat available, giving a value of 910.918 kcal. These two numbers should differ by the enthalpy of formation of water, 68.317 kcal. They actually differ by 67.943, so the error in our enthalpy balance is 0.374 kcal or 0.6%.

To obtain the highest efficiency, the streams that have heat available (that is, streams that must be cooled) must be matched with streams that require heat. Any stream that requires heat but cannot get it from a stream that is being cooled will have to obtain it from the primary heat source, either the VHTR coolant stream or the solar collector. Any stream that must be cooled but cannot transfer heat to a stream requiring it must transfer its heat to the environment; that heat is then wasted.

Unmatched heat available at temperatures greater than 348 K (167°F) is used to generate work at an efficiency equal to two-thirds of the Carnot efficiency. Some unmatched streams require cooling below about 250 K (−9°F) and will need to be refrigerated. This work will have to be generated from heat.

Since a minimum ΔT of 50 K (90°F) is required between streams in heat exchangers, any stream requiring heat at 1150 K (1610°F) or higher must get it from the solar collector. Unmatched heat requirements at lower temperatures are matched with the VHTR coolant. Table 2 summarizes the distribution of heat from the primary heat sources.

Table 3 summarizes the amount of heat wasted and required and the amount of work that needs to be produced from heat. Although we could generate work from heat supplied by the VHTR, a higher Carnot efficiency is possible if we use the isothermal solar heat at 1300 K (1880°F). If waste heat is disposed of at 298 K, then the minimum temperature available to a heat engine is 348 K (taking into account the 50 K ΔT), so the Carnot efficiency is $T_H/(T_H - T_C)$ = 1300/(1300 −348) = 73.2%. Two-thirds of this, or 48.8%, is the overall heat to work efficiency. To generate the necessary 54.529 kcal of work then requires 111.692 kcal of heat at 1300 K (1880°F). The total solar heat required at

Table 2. PRIMARY HEAT SOURCE REQUIREMENTS

	Q, kcal	T, K	
T≥ 1150			
R 3-1	44.522	1300	To be supplied by isothermal heat source at 1350 K
H-5	10.989	1150-1300	
R 3-4	14.191	1150	
H-1	8.544	1250-1300	
	78.246		
T < 1150			
H-5	11.461	994-1150	To be supplied by coolant stream of VHTR cascading from 1250 to 750 K
H-5	24.640	950	
R 3-3	4.786	575	
D-1B	37.616	436-512	
H-1	109.296	508	
H-11	0.032	447-475	
H-16	0.236	446-475	
	188.067		

A78020230

Table 3. LOAD-LINE EFFICIENCY CALCULATIONS FOR CYCLE B-1

Waste Heat	-202.466 kcal
Heat Required from PHS	
T ≥ 1150	78.246
T < 1150	188.067
	266.313 kcal
Work Available	
From unmatched heat*	-3.380
From pressure drops†	-12.374
	-15.754 kcal
Work Required‡	
For refrigeration	1.190
For pumps and compressors	69.093
	70.283 kcal
Net Work Required	54.529 kcal

* Work computed at two-thirds of Carnot efficiency.

$$W = 2/3\ Q\left(\frac{T_H - T_C}{T_H}\right).$$

† Turbines are 80% efficient.

‡ Compressors are 80% efficient.

A78020358

1300 K is 189.938 kcal, while the VHTR supplies 188.067 kcal. Then the total primary heat required is 378.005 kcal, so the load-line efficiency is 68.317/378.005 = 18.1%.

The 18.1% load-line efficiency calculated from the modified, finished flowsheet of Cycle B-1 compares well with the 18% process efficiency reported by EURATOM for a similar cycle.[5] Several cycles, notably the sulfuric acid cycle of Westinghouse (WAES)[6] and the Prime cycle from General Atomic[7] have been analyzed, and efficiencies in the 40% to 50% range projected. (These figures have been optimized through several iterations, as opposed to the single iteration performed here.) However, our engineering taskwork was based on several assumptions that are more conservative than those used elsewhere.

We have recognized and addressed our analysis to the necessity of producing hydrogen under pressure to avoid the severe energy and capital expenses associated with compressing large volumes of hydrogen from atmospheric pressure to pipeline pressure (estimated at about 70 atm).[2] The process flowsheet for Cycle B-1 specifies hydrogen production at 30 atm in Reaction 1 at the expense of extra separations work due to a reduced hydrogen concentration at elevated pressures.

We assumed a conservative minimum temperature difference (ΔT_m) of 50 K (90°F) across all heat exchangers, which is larger than that used in some commercial applications. An example of energy savings achieved by lowering ΔT_m to 25 K (45°F) is the separation of Fe_2Cl_6 from the Cl_2 product from Reaction 3. Here, sublimed Fe_2Cl_6 is removed by condensation. The Fe_2Cl_6-Cl_2 mixture is compressed to condense Fe_2Cl_6 at a temperature 50 K higher than the temperature at which it is sublimed. In this manner, we were able to supply the heat of sublimation (282 kcal/mole H_2)with heat liberated during condensation. At ΔT_m equal to 50 K, this scheme requires about 52 kcal of work for compression. If ΔT_m is reduced to 25 K, a lower pressure is required, and work for compression is reduced to about 41 kcal. Also, our realistic assumption of 80% efficient turboexpanders and shaftpower-to-compression appears more conservative than values used by others.

In summary, the final flowsheet upon which load-line efficiency calculations were based has not been optimized by any formal procedure due to time and funding limitations. Without a formal optimization procedure, it was necessary to make assumptions (some examples are discussed above) that are

generally appropriate, but which might be unnecessarily conservative in specific cases. Optimization of specific portions of the final flowsheet would undoubtedly result in a higher load-line efficiency than 18.1%.

Cycle H-5

Cycle H-5 is a copper oxide-copper sulfate cycle, and is summarized below:

$$CuO(s) + SO_2(g) + 6H_2O(\ell) \rightarrow CuSO_4 \cdot 5H_2O(s) + H_2(g) \quad (5)$$

$$CuSO_4 \cdot 5H_2O(s) \rightarrow CuSO_4(s) + 5H_2O(g) \quad (6)$$

$$CuSO_4(s) \rightarrow CuO(s) + SO_3(g) \quad (7)$$

$$SO_3(g) \rightarrow SO_2(g) + 1/2\ O_2(g) \quad (8)$$

This cycle is written to describe the formation of copper sulfate pentahydrate during the electrolysis of aqueous SO_2 containing CuO(s). All the reactions in Cycle H-5 were recently demonstrated with recycled materials. The cycle was chosen earlier for engineering analysis to determine a load-line efficiency.

We developed a base-case flowsheet for Cycle H-5 using the guidelines previously discussed (pages 2 - 5) for the analysis of Cycle B-1. Cycle H-5 is, from an engineering standpoint, simpler than Cycle B-1 because:

- There are fewer gas-phase separations.
- Using conventional reduced-temperature techniques, separations will be less energy-intensive. Because most of the primary gas phase products (SO_2, O_2, H_2O) are cycled to low-temperature applications SO_2 and H_2O to the electrolyzer, O_2 vented to the atmosphere), reheating after separation will be minimized.
- The overall process scheme is simpler, if compared to Cycle B-1.

Although Reaction 5 has been demonstrated electrochemically, the optimum electrolyzer configuration has not yet been determined. For cycle flowsheet analysis, we assume a cell capable of producing solid copper sulfate pentahydrate (saturated solution) and hydrogen at pressures of at least 30 atm.

Base-Case Flowsheet

A base-case flowsheet for Cycle H-5 was constructed to identify those areas which would benefit most from intensive research. The base-case scheme was kept as simple as possible by assuming atmospheric operation of Reactions 5, 7, and 8, and a maximum process temperature of 1150 K (1610°F). The primary

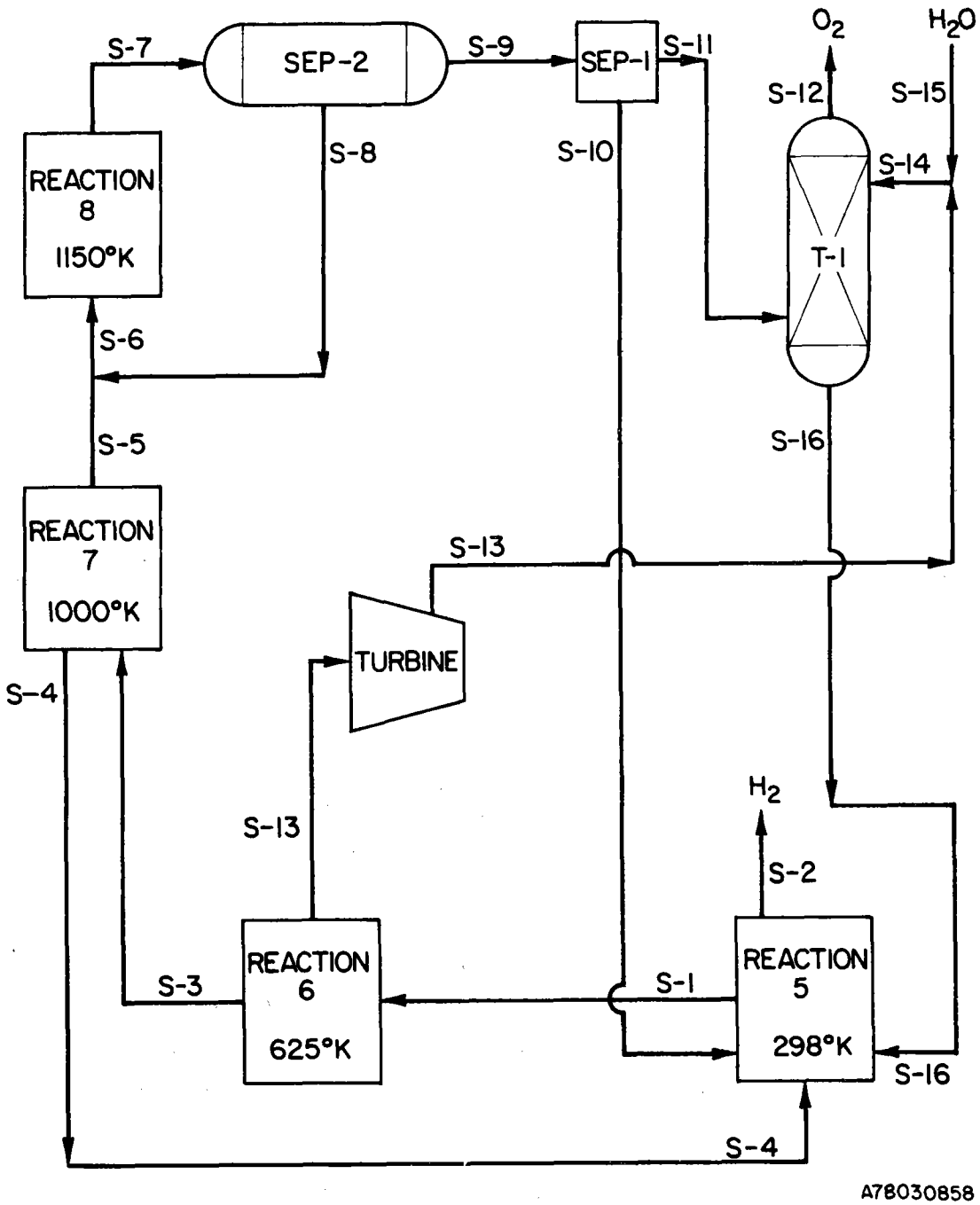

Figure 6. SCHEMATIC DIAGRAM OF THE BASE-CASE FLOWSHEET FOR CYCLE H-5

Table 4. MOLAR FLOW RATES FOR THE H-5 FLOWSHEET

Stream	Composition, moles	Temperature at Source, K
S-1	1.094 $CuSO_4 \cdot 5H_2O$	298
S-2	1.000 H_2	298
S-3	1.094 $CuSO_4$	625
S-4	1.094 CuO	1000
S-5	0.615 SO_2 0.479 SO_3 0.239 O_2	1000
S-6	0.615 SO_2 0.668 SO_3 0.359 O_2	1000
S-7	1.000 SO_2 0.283 SO_3 0.500 O_2	1150
S-8	0.189 SO_3	273
S-9	1.000 SO_2 0.094 SO_3 0.500 O_2	273
S-10	0.996 SO_2 0.094 SO_3	Undefined
S-11	0.500 O_2 0.004 SO_2	Undefined
S-12	0.500 O_2	298
S-13	5.470 H_2O	625
S-14	6.470 H_2O	298
S-15	1.000 H_2O	298
S-16	6.470 H_2O 0.004 SO_2	298

A78030784

gas-phase separation involves the effluent from Reaction 8; we did not define this separation precisely. Figure 6 is a schematic of the base-case flowsheet. Molar flow rates of all compounds, indicated in Table 4, are based on the production of 1 gram-mole of hydrogen.

The electrolyzer/crystallizer is not completely defined, but for the base-case flowsheet, we assume that electrolysis proceeds as written to produce H_2 and a concentrated copper sulfate solution, which is crystallized to $CuSO_4 \cdot 5H_2O$. The electrolyzer product, $CuSO_4 \cdot 5H_2O$, is dehydrated at elevated temperatures to provide pressurized steam for power recovery to supply some of the work required by the electrolyzer. Dry $CuSO_4$ is decomposed at 1000 K (1340°F). The gas stream (S-5) leaving this reactor is assumed to be an equilibrium mixture of SO_3, SO_2, and O_2 at 1000 K. (Reactions 7 and 8 are not discrete.) The O_2 content of this stream is adjusted by catalytic decomposition of SO_3 at 1150 K (1610°F) (Reaction 8). The components of the gaseous effluent from this reaction are separated as follows:

- The bulk of the SO_3 is removed by condensation at 273 K (32°F) in SEP-2 and, after vaporization, recycled to Reaction 8 to be decomposed.
- SO_2-O_2 mixtures are successively compressed and intercooled to condense most of the SO_2, which is recycled to the electrolyzer.
- The O_2 product is scrubbed in T-1 by the H_2O feed and condensed steam from the turbine to remove the remaining traces of SO_2, which are recycled with the water to the electrolyzer.

Analysis of the base-case flowsheet for Cycle H-5 identified two portions of the process that would have the most effect on a load-line efficiency calculated from a modified flowsheet. First, work requirements for gas-phase separations can be large; this point was demonstrated in our earlier analysis of the load-line efficiency for Cycle B-1. The primary gas-phase separation in Cycle H-5 involves the effluent from the SO_3 decomposition. To modify the base-case flowsheet, the reaction conditions were investigated to reduce the SO_3 content of the effluent, and the SO_2-O_2 separation was defined to minimize work requirements. Second, the dehydration of copper sulfate pentahydrate is energy-intensive. If SO_3 is returned to the electrolyzer in the SO_2 recycle stream, or if undecomposed $CuSO_4$ is returned in the CuO recycle, the burden on the dehydration step is increased with no corresponding increase in hydrogen production. Modifications to the base-case flowsheet were made so that the minimum number of moles of pentahydrate will be decomposed per mole of hydrogen produced.

Modifications to the Base-Case

Modifications to the base case were made in the following four areas:

1. The temperature and pressure of the copper sulfate decomposition and the sulfur trioxide decomposition (Reactions 7 and 8) were changed to reduce the SO_3 content of the effluent from Reaction 8.

2. A separate step to separate SO_3 from SO_2 and O_2 was dropped because we were able to virtually eliminate SO_3 by modifying reaction conditions.

3. The SO_2-O_2 separation scheme was defined.

4. The conditions for Reaction 6 were adjusted to maximize the amount of useful heat recoverable from the condensing steam produced by that reaction.

Modification of the temperature and pressure conditions for the copper sulfate and sulfur trioxide decompositions (Reactions 7 and 8, respectively) were designed to minimize the equilibrium SO_3 concentration in the effluent from Reaction 8 (Stream 7). Figure 7 is a plot of the mole fraction of SO_3 at equilibrium versus the temperature of Reaction 8. The SO_3 mole fraction decreases with increasing temperature and decreasing pressure. In the modified flowsheet for Cycle H-5, the maximum temperature available from a solar heat source (1300 K, 1880°F) was assumed for Reaction 8. We allowed the pressure for Reactions 7 and 8 to be determined by the equilibrium pressure of SO_3, SO_2, and O_2 generated in Reaction 7. At 1000 K (1340°F), the Gibbs free-energy change for Reaction 7 is 9.5 kcal/mole, and the equilibrium pressure is 0.095 atm absolute. A higher temperature for Reaction 7 would result in higher pressure of gaseous products, which is undesirable. A lower temperature would result in a lower reaction rate — also undesirable. From laboratory observations, it appears that 1000 K is optimum with respect to both reaction rate and system pressure. We assumed that the gaseous effluent from Reaction 7 (Stream 5) is an equilibrium mixture of SO_3, SO_2, and O_2. From Figure 7, the mole fraction of SO_3 in the gaseous product of Reaction 8 at 1300 K and reduced pressure (0.095 atm) is about 0.014. Although it is not desirable to recycle SO_3 to the electrolyzer (Reaction 5), the concentration of SO_3 in stream 7 is low enough that the energy expenditure required to separate and recycle it is higher than the energy penalty for returning it to the electrolyzer with the SO_2 recycle (stream 10). Therefore, as a result of modified reaction conditions

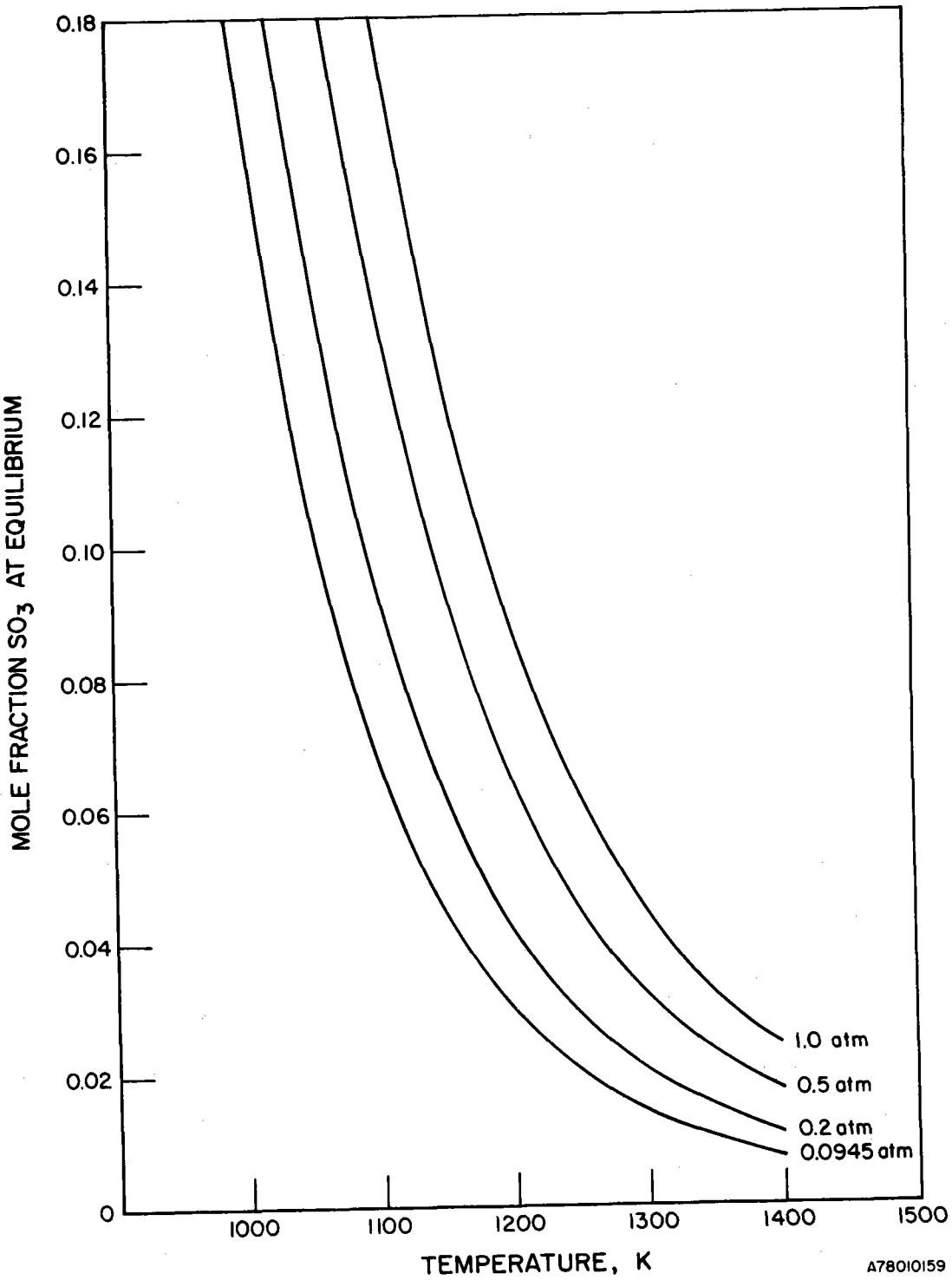

Figure 7. EQUILIBRIUM SO_3 MOLE FRACTION VERSUS TEMPERATURE AND PRESSURE

for Reactions 7 and 8, the final flowsheet does not include the SO_3 separation and recycle (SEP-2 and stream 8) present in the base-case flowsheet.

In the base-case flowsheet, gross separation of SO_2 from product O_2 is accomplished in SEP-1 (undefined) and final SO_2 content adjusted by means of a water scrub in T-1. We have defined a series of two separations with a relatively small work requirement for compression. The stream leaving Reaction 8, comprised of SO_3 (1.4 mole percent, SO_2 (65.7 mole percent), and O_2 (32.9 mole percent), is treated as follows in SEP-1.

- The gas mixture is cooled to 348 K (167°F).
- The cooled mixture is compressed in a single stage from 0.095 atm to 0.307 atm. The temperature at the compressor exit is 467K (382°F).
- The mixture is cooled at 348 K.
- The cooled mixture is compressed in a second stage to 1 atm. The temperature at the compressor exit is 467 K.
- Final cooling and refrigeration lowers the temperature to 233 K (−40°F).

At 1 atm and 233 K, 87 mole % of the SO_2 (and essentially 100% of the SO_3) in the gas stream condenses as a liquid. A knockout drum separates the liquid phase (for direct recycle to the electrolyzer) from a gas phase containing the O_2 product (80 mole percent) and remaining gaseous SO_2 (20 mole percent). Final separation of SO_2 from O_2 is done by water-scrubbing. The water absorbent is made up of the process feed water and the recycled water from Reaction 6 to the electrolyzer. Equilibrium data for the SO_2-H_2O system indicate that the water available for scrubbing is sufficient to reduce the final SO_2 concentration in the oxygen product to 1-2 ppm. The spent scrubbing solution, containing absorbed SO_2, is recycled directly to the electrolyzer. Work requirements for the two compression stages are a modest 3 kcal (basis: 1 gram-mole of hydrogen produced). In addition, some heat is available from the heat exchangers which cool the gas stream between compression stages.

Dehydration of copper sulfate pentahydrate, Reaction 6, actually takes place in three steps[8]:

$$CuSO_4 \cdot 5H_2O \rightarrow CuSO_4 \cdot 3H_2O + 2H_2O \quad (6a)$$

$$CuSO_4 \cdot 3H_2O \rightarrow CuSO_4 \cdot H_2O + 2H_2O \quad (6b)$$

$$CuSO_4 \cdot H_2O \rightarrow CuSO_4 + H_2O \quad (6c)$$

When each reaction (Reactions 6a, 6b, 6c) is allowed to produced an equilibrium water vapor pressure of one atmosphere, the reactions occur at temperatures of 375, 383, and 481 K. The steam thereby produced condenses at 373 K, releasing 48.6 kcal of latent heat per mole of $CuSO_4 \cdot 5H_2O$. Since the bulk of this process (Cycle H-5) takes place at either very high temperatures (1000 to 1300 K) or at low temperatures (~298 K), almost all of the 48.6 kcal of 373 K heat is wasted. We investigated two schemes which would allow us to use at least a portion of this heat.

In the base-case flowsheet, Reaction 6 is operated at a higher temperature (~625 K) in order to produce a high pressure steam which can be blown down through a series of condensing turbines to generate work. However, it is apparent that any work obtained from the turbines is due to the additional heat input to the dehydration reaction that is necessary to produce the higher pressure steam. Therefore, high-pressure steam production via Reaction 6 is advisable only if an excess of moderately high temperature heat is still available from within the cycle after process heat streams are matched to maximize heat transfer. This did not turn out to be the case and therefore the proposal to operate Reaction 6 to produce steam for generating work was abandoned.

In the modified flowsheet (Figure 8), Reactions 6b and 6c are conducted at 425 and 526 K, thereby producing an equilibrium water vapor pressure of 4.94 atm. At this pressure, steam condensed at 425 K or 50 K higher than the temperature for Reaction 6a. Since our requirement of a 50 KΔT across heat exchangers will be satisfied, the heat of reaction of 6a could now be supplied by the latent heat of the steam produced by Reactions 6b and 6c, instead of by the primary heat source. In addition, only the latent heat of the steam produced by Reaction 6a is now wasted.

Reaction 5 has been operated in the laboratory at room temperature with an applied voltage ranging from 0.45 to 0.80 volt. The lower value (0.45 volt), used in calculating the energy balance, translates into a work requirement

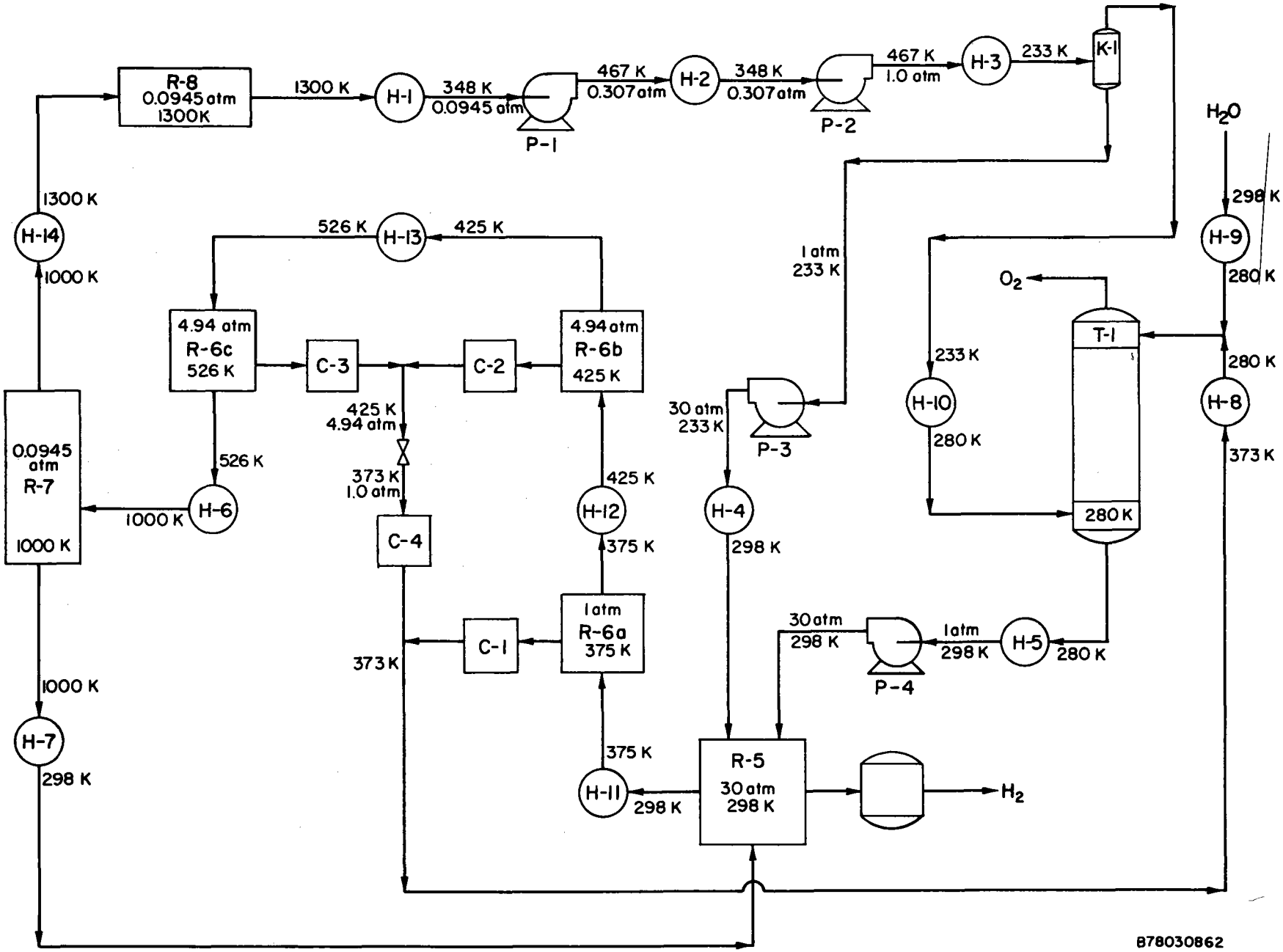

Figure 8. MODIFIED FLOWSHEET FOR CYCLE H-5

(Gibbs free-energy change, ΔG_{Rx}) for Reaction 5 of 20.755 kcal/mol. The reaction is conducted at 30-atm pressure. Some final cleanup of the H_2 product stream using molecular sieves to remove residual SO_3 and H_2O will probably be necessary, although the quantities of these contaminants is expected to be minute.

Load-Line Efficiency Calculation

An enthalpy balance around the modified flowsheet was performed in the same manner as for Cycle B-1. Total heat and ideal work requirements for Cycle H-5 are 187.583 kcal per mole of H_2 produced. The total amount of heat available, plus the ideal work available if the H_2 were expanded to the reference pressure of 1 atm, is 122.421 kcal. These two numbers differ by 65.162 kcal, or 3.155 kcal less than the enthalpy of formation of water, which is 68.317 kcal, giving us an error of 4.6% in our enthalpy balance.

With the stipulation that a minimum ΔT of 50 K (90°F) be required between streams in heat exchangers, streams having heat available were matched, to the greatest possible extent, with streams requiring heat. Any heat requirements not met in this manner are fulfilled by the primary heat source, either the VHTR coolant stream or the solar collector. Table 5 summarizes the distribution of heat from the primary heat sources. Unmatched streams which must be cooled transfer their heat to the environment as waste heat. Unmatched streams that require cooling below 348 K (167°F) need to be refrigerated; this work has been generated from heat.

Table 6 summarizes the waste heat, the heat required for work, and the process heat that is to be derived from the principal heat sources. As in Cycle B-1, work is generated from isothermal solar heat at 1300 K (1880°F), at an overall efficiency of 48.8%. To generate the necessary 32.616 kcal of work requires 66.808 kcal of heat. Adding to this the 123.419 kcal of process heat gives the total heat requirement for Cycle H-5 of 190.227 kcal. Then the load-line efficiency is 68.317/190.227 = 35.9%.

Because the Cycle H-5 flowsheet is relatively simple, we were able to examine the effect of our use of a conservative 50 K (90°F) minimum temperature difference across heat exchangers. Using ΔT_m = 25 K (45°F), a few minor changes were made in process conditions, and the stream matching procedure was repeated. Although process heat requirements increased slightly

Table 5. PRIMARY HEAT SOURCE REQUIREMENTS

	Q, kcal	T, K
T ≥ 1150		
R-8	4.865	1300
H-14	1.267	1230-1300
Work	66.808	1300
	72.940	
T < 1150		
R-2B	25.274	425
R-2C	18.271	526
R-3	69.072	1000
H-6	4.670	768-798, 894-1000
	117.287	

Table 6. LOAD-LINE EFFICIENCY CALCULATIONS FOR CYCLE H-5

	kcal
Waste Heat	46.844
Work Required*	
For Refrigeration	8.760
For Pumps and Compressors	3.101
For Electrolyzers	20.755
Total	32.616
Heat Required From PHS	
T ≥ 1150 K	72.940
T < 1150 K	117.287
Total	190.227

* Primary compression 80% efficient.

to 124,767 kcal, work requirements were reduced to 29.283 kcal, due primarily to lower refrigeration requirements. Since heat could now be rejected at 323 K (122^{o}F) instead of at 348 K (167^{o}F), the overall heat-to-work efficiency was raised to 50.1%, and the amount of heat required to generate work for the process was reduced to 58.446 kcal. Total heat requirements for Cycle H-5 with ΔT_m = 25 K (45^{o}F) are 183.213 kcal, giving a load-line efficiency of 37.3% — an increase of 1.4%.

The EURATOM Mark-13 Cycle

The room-temperature electrode potential for the hydrogen production step of the EURATOM Mark-13 cycle is 1.08 volts when all solvated species are at unit activity and the bromine pressure is 0.28 atm.[9] Such a voltage is impractical for a hybrid thermochemical cycle since it represents a work input to the cycle of 49.8 kcal/mole H_2 (at 100% heat-to-work efficiencies). At 40% heat-to-work efficiency, the work input is 122.9 kcal/mole H_2.

The cycle proposed by Schuetz[9] is given below:

$$2H_2O(\ell) + SO_2(g) + Br_2(\ell) \rightarrow H_2SO_4(aq) + 2HBr(g) \quad (9)$$

$$H_2SO_4(aq) \rightarrow H_2O(g) + SO_2(g) + 1/2\ O_2(g) \quad (10)$$

$$2HBr(aq) \rightarrow H_2(g) + Br_2(\ell) \quad (11)$$

As Schuetz correctly points out, the cell voltage for the hydrogen production step (Reaction 11) falls rapidly as the activities of the solvated species increase. The Nernst correction to the standard electrode potential, E^o, is most strongly dependent on the concentrations (more properly the activities) of hydrogen ion, H^+, and bromide ion, Br^-, so that as the concentration of HBr increases the cell voltage for HBr electrolysis decreases. The actual cell potential is calculated from the Nernst equation-

$$E_{actual} = E^o + (RT/2F)[\log \{P(H_2)/P^o(H_2)\} + \log \{P(Br_2)/P^o(Br_2)\} - 2 \log a(HBr)] \quad (12)$$

where R is the gas constant, T the absolute temperature, F the Faraday, a the activity, P the vapor pressure and P^o is the vapor pressure at reference conditions. Under ordinary conditions, $P(H_2)/P^o(H_2)$ and $P(Br_2)/P^o(Br_2)$ are near unity, so that E_{actual} depends most strongly on a(HBr), the HBr activity, with $dE/da(HBr) < 0$.

Faita, Mussini, and Oggioni,[10] using the electrochemical system Pt/Ag/AgBr//HBr //H_2 (1 atm)/Pt (anode//electrolyte//cathode), determined the thermodynamic functions for HBr(aq) in the range of concentrations of 0.477% to 30.005% (0.0555 molal to 4.441 molal). If these figures are used to calculate the cell voltage as a function of the molality, m, the standard potential for the HBr azeotrope, (HBr ~47.5%) is ~0.8 volt.

The data of Faita et al. is useful in that they show that E falls continuously as m(HBr), or a(HBr) increases. The thermodynamic data are probably flawed, however, since they calculated HBr data from emf measurements on an AgBr electrode. The HBr electrolysis data is complicated by a second equilibrium —

$$Br^- + Br_2 \rightarrow Br_3^- \qquad (13)$$

which does not affect the solubility-concentration equilibrium of the AgBr electrode —

$$AgBr \rightarrow Ag^+ + Br^- \qquad (14)$$

Schuetz[9,11] has consistently achieved electrolysis of HBr at cell voltages lower than 1.08 volts, and the potential attractiveness of this cycle is apparent if the operating voltage can be kept below 0.5 volt, while supporting high current densities. Schuetz reported high current densities for platinum and platinized platinum electrode surfaces. He also reported that the Br_2-enriched HBr(aq) attacked the high surface area Pt electrodes. Schuetz's later reports indicate that current densities of the order of 200-300 mA/cm^2 can be obtained on graphite (and Pt) at anode potentials of the order 500 to 640 mV.

He recognized that Br_2(aq) at the anode tended to raise the anode potential (as predicted by the Nernst equation), but catholysis of the free bromine is also a possible difficulty in that —

$$Br_2 + 2e^- \rightarrow 2Br^-. \qquad (15)$$

This would have the virtual effect of electrolyte deactivation, because of the mixed potential that resulted. The aim of the ISPRA Mark-13 investigators is, clearly, to achieve operating voltages of less than 1.0 volt. This appears to be too high a limiting operating voltage to achieve high energy efficiency for this cycle.

Figure of Merit – Hybrid Cycles

In a multistep, thermochemical water-splitting cycle, the efficiency, η, is generally regarded as[12,13] —

$$\eta = HHV(H_2)/(Q_i + w'/\eta_w) \qquad (16)$$

where $HHV(H_2)$ is the higher heating value of one mole of H_2 at STP, Q_i is the process heat input, w' is the work required by the cycle, and η_w is the efficiency of converting primary heat source energy to work. If we isolate the

hybrid step in the Mark-13 cycle, and calculate a figure of merit, Z_E, for the electrolysis of HBr, it can be defined as Z_E = heating value-out/heating value-in. In this scheme we assumed that HHV(H_2) is the heating value-out and also the minimum heating value-in — the enthalpy of formation of the hydrogen is assumed to be the minimum of supplied process heat over all the steps. The figure of merit must also account for the work input for electrolyzing the HBr, so that —

$$Z_E \equiv HHV(H_2)/[HHV(H_2) + zFV/\eta_w] \qquad (17)$$

with zF = 23.052 kcal/volt equivalent. For one mole of hydrogen, two equivalents of electricity are required, so that $Z_E = 68.32/(68.32 + 46.104\ V/\eta_w)$.

If a figure of merit of at least 0.50 is desired, then 46.104 V/η_w can be no larger than 68.32, or V = 1.482 volt for perfect heat-to-work conversion. If, however, we deal with real generator schemes, $\eta_w \approx 0.40$, and the limiting upper voltage is constrained below 0.593 volt. This is a serious constraint since it is, essentially, perfectly general (given the assumptions). It means for any hybrid cycle that operates at 0.593 volt, the system figure of merit will be no more than 50% if there is no waste heat and there are no unmatched heat streams in the system. Riekert has treated the efficiency of energy utilization in detail elsewhere,[14] but the problem this electrochemical constraint represents may be seen in Figure 9, where the figure of merit, Z_E, is plotted as a function of cell voltage for a set of η_w-values.

Electrolysis of HBr

Electrolysis experiments were begun after some simple preliminary work to see whether intercalation (interlayer) compounds were formed in the graphites under study. Samples of fuel cell graphite and of a porous graphite cloth were subjected to aging in HBr (48%). X-ray diffraction on a before-and-after basis showed no evidence of intercalation (d-space shifts, line shifts, etc.). Blackman, Saunders and Ubbelohde[15] did not find intercalation in concentrated HBr, but the materials they used also contained free $Br_2(\ell)$. Vitreous graphite is expected to resist this process, and Pt will not be "aged." In carbon electrodes used for the chlor-alkali process, intercalation is known to occur, but to very slight harmful effect. The effects of intercalation, if harmful, needed to be determined in the C(s)/HBr(aq) system.

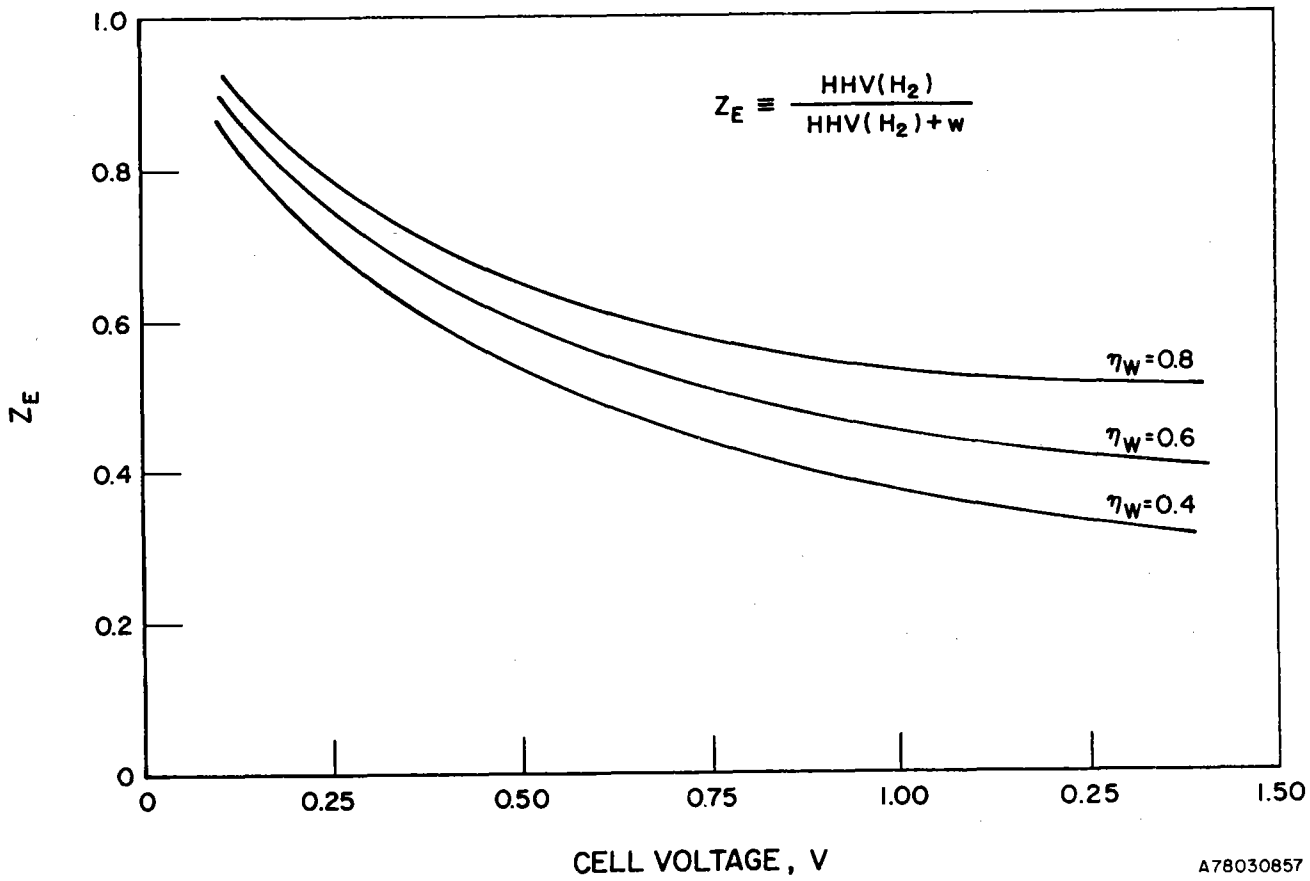

Figure 9. THE FIGURE OF MERIT OF HYBRID CYCLES AS A FUNCTION OF CELL VOLTAGE

Concentrated HBr from most suppliers is contaminated with Br_2, which represents a positive polarization problem in the electrolysis. The voltage of the cathode reaction of Br_2(aq) is 1.08 volt so the cell voltage is driven up if Br_2 is present in quantities large enough to react extensively. Our chemical supplier had no easy solution to the Br_2 contamination problem, but some of the literature indicates the Br_2 can be removed by vacuum distillation[16] or by sorption on activated charcoal.[17]

Some effort to obtain lower Br_2 concentrations and to define those concentrations that are present as contamination should be assayed for future electrolysis. The role of the dissolved Br_2 in the higher electrode polarization values will remain ill-defined as long as the HBr azeotrope is contaminated, or until we can perform the electrolyses in Br_2-free HBr.

For all the polarization curves [E = E(i)] that follow, we calculated a regression expression for the linear region of the curve where possible. Figures based on the data are drawn so that the linear region encompasses only the data used to generate the regression line. In each case, the intercept represents a "practical decomposition potential" for that system, and the slope (the coefficient of i, the current density) is a resistance-related characteristic of the electrode/electrolyte system. Regressions are not quoted where the correlation coefficient ("goodness" of the line), C_f, was less than 0.9200.

Electrolysis on Porous Graphite

A series of galvanostatic polarization experiments were done on graphite surfaces (C_x) in concentrated HBr (47.5%) contaminated with dissolved Br_2. In the experiments, we measured the equilibrium cell voltage as a function of impressed current. The electrolysis was done in a 300 K thermostat (water-filled) with electrode separation effected by 3.2-mm sheets of porous polyvinylidene difluoride (PVFF). A preliminary experiment to begin to define the performance envelope for HBr electrolysis on graphite was done first. The voltages were prohibitively high, perhaps because of Br_2 contamination. Table 7 gives the results of cell voltage measurements as a function of current.

Table 7. CURRENT-VOLTAGE CHARACTERISTICS OF HBr ELECTROLYSIS ON POROUS GRAPHITE at 300 K

Cell Voltage, volts	Total Current, mA	Current Density, mA/cm^2
1.685	282	27.0
1.730	325	31.1
1.765	367	35.1
1.854	452	43.2
1.944	566	54.2
2.06	693	66.3

At currents much less than 280 mA, the system voltage dropped precipitously, and measurements were unsteady. This electrolysis was done in unstirred HBr azeotrope with an electrode separation of 3.2 mm. These are preliminary results only, but the data are remarkably linear. We subjected the current-voltage data to a simple linear regression and developed the relation (for $V \geq 1.685$) —

$$V = 9.46 \times 10^{-2} i + 1.434 \quad \text{(volts)} \tag{18}$$

with a correlation coefficient, C_f, of 0.9992.

Galvanostatic electrolysis was used throughout because it best models the projected system as it will be utilized. In some experiments, to isolate anode effects, the cathode was replaced by a shiny platinum gauze of large area. This has the effect of making the anode polarization the system-limiting measurement. Table 8 summarizes the equilibrium cell voltage for a system, $C_x//HBr//C_x$, polarized between a current density of about 6 mA/cm^2 and about 158 mA/cm^2 (anode current densities). The polarization curve (Figure 10) is linear in the region $i > 50$ mA/cm^2, with the least-squares line ($C_f = 0.9992$) given by —

$$V = 0.00303\ i + 0.842 \text{ volt.} \tag{19}$$

For this system, a current density of 300 mA/cm^2 would be achieved at a voltage of 1.75 volts.

Table 8. SYSTEM VOLTAGES FOR HBr ELECTROLYSIS ON GRAPHITE
(T = 300 K, Separation 3.2 mm, Quiet Electrolyte)

i, mA/cm^2	V, volts
5.7	0.088
9.48	0.125
12.63	0.225
15.8	0.305
22.1	0.847
31.6	0.906
50.5	0.988
69.5	1.055
88.4	1.116
107.4	1.172
126.3	1.228
142.1	1.271
157.9	1.317

The strong role of cathode polarization is shown in Figure 11, where cell voltages for the C_x//HBr//C_x system are plotted on a common axis with those for the C_x//HBr//Pt system. The overvoltage for hydrogen association on graphite is quite high, and the increase in system voltage may be contributed to by catholysis of dissolved Br_2:

$$Br_2 + 2e^- \rightarrow 2Br^- \qquad (15)$$

Latimer[18] gives the difference in hydrogen overvoltage at these current densities as about 0.7 volts. His values are based on 1M H_2SO_4, but at all current densities the hydrogen overvoltage on C_x is much higher than on smooth platinum. There is an additional anomaly in Figure 11. Since the electrolyte is the same, the slopes of the linear parts of the polarization curves (the ohmic regions) should be the same. (It represents a resistivity measure.) In the case of Figure 11, the slopes differ as shown in Table 9.

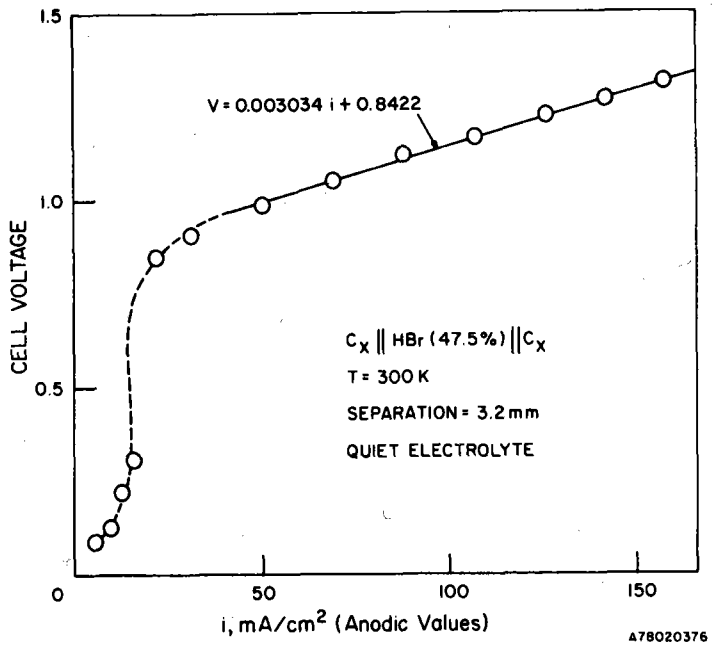

Figure 10. POLARIZATION OF GRAPHITE IN HBr (aq)

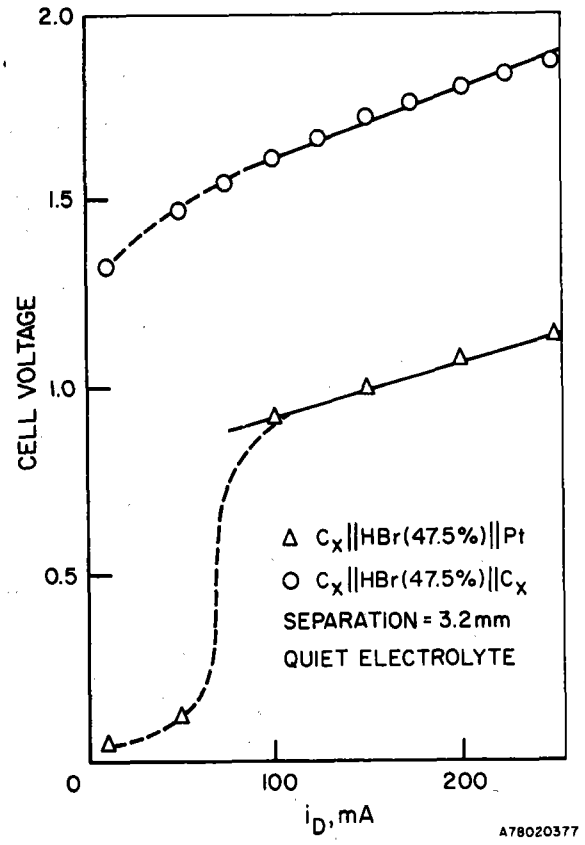

Figure 11. ANODE ISOLATION: POLARIZATION IN CELLS WITH DIFFERENT CATHODES

Table 9. CHARACTERISTICS OF THE OHMIC POLARIZATIONS

System	Slope, ohms	Intercept, V	C_f
C_x//HBr//C_x	1.79	1.44	0.9819
C_x//HBr//Pt	1.44	0.773	0.9982

Electrolyses were also done on graphite cloth (Union Carbide, WCA grade), but the electrolyzer voltages were quite high. At current densities varying between 2.7 mA/cm^2 and 77.5 mA/cm^2, a cell with graphite cloth anode and cathode had a cell voltage that varied from 1.701 to 2.67 volts. If the cathode was replaced by a large area Pt-gauze electrode (to isolate the anode polarization), the cell voltage at ~77.5 mA/cm^2 was, once again, ~2.7 volt. It did not appear useful to pursue electrolysis on this material.

A final experiment with porous graphite was done to confirm the increased polarization if a(HBr) decreases. A 37.0% solution of HBr was made up by diluting the azeotrope with H_2SO_4 solution (sp gr = 1.200). This solution was polarized from 5.7 mA/cm^2 to 158 mA/cm^2. The data are summarized in Table 10 and compared almost point-by-point to similar electrolysis in the azeotrope (47.5%).

Table 10. SYSTEM VOLTAGES FOR ELECTROLYSIS IN HBr AT TWO CONCENTRATIONS — QUIET ELECTROLYSIS
(T = 300 K, Separation 3.2 mm)

	V, volts	
i, mA/cm^2	47.5%	37.1%
5.7	0.088	0.110
9.48	0.125	--
12.7	0.225	0.740
22.1	0.847	0.912
50.5	0.988	--
53.6	--	1.055
126.3	1.228	1.299
142.1	1.271	--
148.4	--	1.364
157.9	1.317	1.393

Electrolysis on Pt

Electrolysis experiments on platinum surfaces were done in quiet and stirred electrolyte. Smooth Pt electrodes were polarized between ~6.4 mA/cm^2 and 200 mA/cm^2, and the data analyzed. In Table 11, the data for the Pt//HBr (47.2%) //Pt system with electrodes of equal area are shown.

With the same polarization at both electrodes, the effect of stirring is not very large, but certainly is significant. If, on the other hand, the cathode polarization is markedly decreased, by replacing the cathode with a large area platinum gauze, Pt*, the effects are quite dramatic, demonstrating again that cathode polarization is of considerable importance. The data for high anode polarization is shown in Table 12. The cathode area is unknown in these experiments, but it is assumed that the cathode current densities are less than 15 mA/cm^2.

Table 11. SYSTEM VOLTAGES FOR ELECTROLYSIS ON PLATINUM — Pt//Hbr(47.5%//Pt (T = 300 K, Separation 5.1 mm)

i, mA/cm^2	V, volts	
	Quiet	Stirred
6.4	0.744	--
20.0	0.790	--
40.0	0.834	0.797
60.0	0.864	--
80.0	0.894	0.859
100.0	0.919	--
120.0	0.943	0.910
160.0	0.985	0.955
200.0	1.025	0.997

Table 12. SYSTEM VOLTAGES FOR ELECTROLYSIS ON PLATINUM — Pt//HBr (47.5%) //Pt*
(T = 300 K, Separation 3.2 mm)

i, mA/cm^2	V, volts	
	Quiet	Stirred
6.4	0.076	0.020
20.0	0.082	--
28.0	0.113	--
40.0	--	0.064
60.0	0.759	--
80.0	0.785	0.099
100.0	0.803	
120.0	0.819	0.130
160.0	0.849	0.160
200.0	0.878	0.188

The differences for these two cases can be seen in Figures 12 and 13. It is clear that stirring can be useful only in those electrolysis regions where the diffusion layer at the electrode surface is thin (lower values of i). In the case of HBr electrolysis, a second phase is evolved at both electrodes — $H_2(g)$ at the cathode and $Br_2(\ell)$ at the anode. Stirring can more easily sweep away the hydrogen formed at the cathode, while the $Br_2(\ell)$ formed at the anode, being quite dense (ρ = 3.1 gm/cm^3), is less likely to be swept out by anything but very intense stirring.

By operating the system Pt*//HBr (47.2%) //Pt, we can confirm this. Table 13 is a summary of the electrolysis data for quiet and stirred electrolysis where the cathode polarization is high.

Figure 14 shows what little effect stirring has on anode performance. If compared to Figure 12, it clearly indicates that cathode polarization controls the cell voltage, since, in both cases where the cathode polarization is high, the cell voltage is such that $0.895 \leq V(200\ mA/cm^2) \leq 1.025$. When the cathode polarization is very low (Figure 12), $V(200\ mA/cm^2)$ = 0.878 volt.

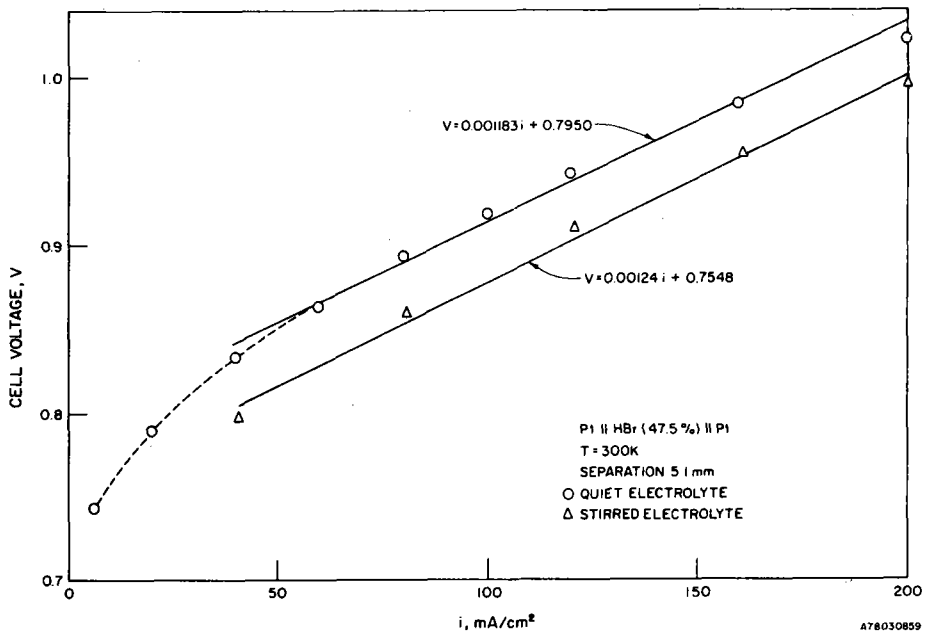

Figure 12. POLARIZATION CURVES FOR SMOOTH PLATINUM

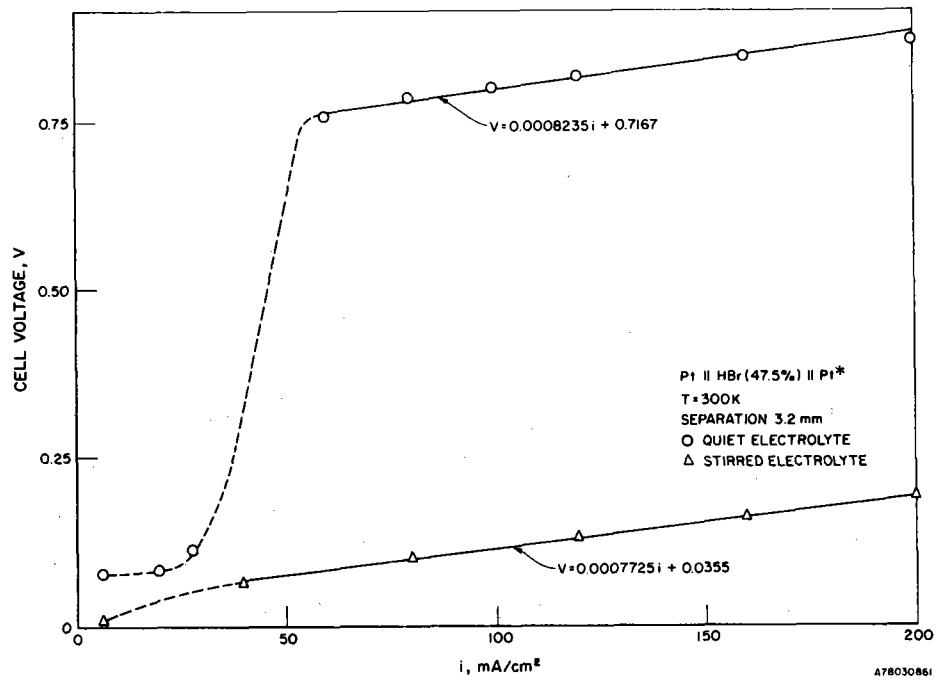

Figure 13. POLARIZATION OF SMOOTH PLATINUM — ANODE ISOLATION

Table 13. SYSTEM VOLTAGES FOR ELECTROLYSIS ON PLATINUM — Pt*//HBr (47.5%)//Pt

i, mA/cm^2	V, volts	
	Quiet	Stirred
6.4	0.693	--
8.8	--	0.679
20.0	--	0.715
28.0	0.731	--
60.0	0.769	0.764
88.0	0.798	--
100.0	--	0.802
112.0	0.822	--
140.0	--	0.837
148.0	0.854	--
172.0	0.874	--
180.0	--	0.869
200.0	0.895	0.887

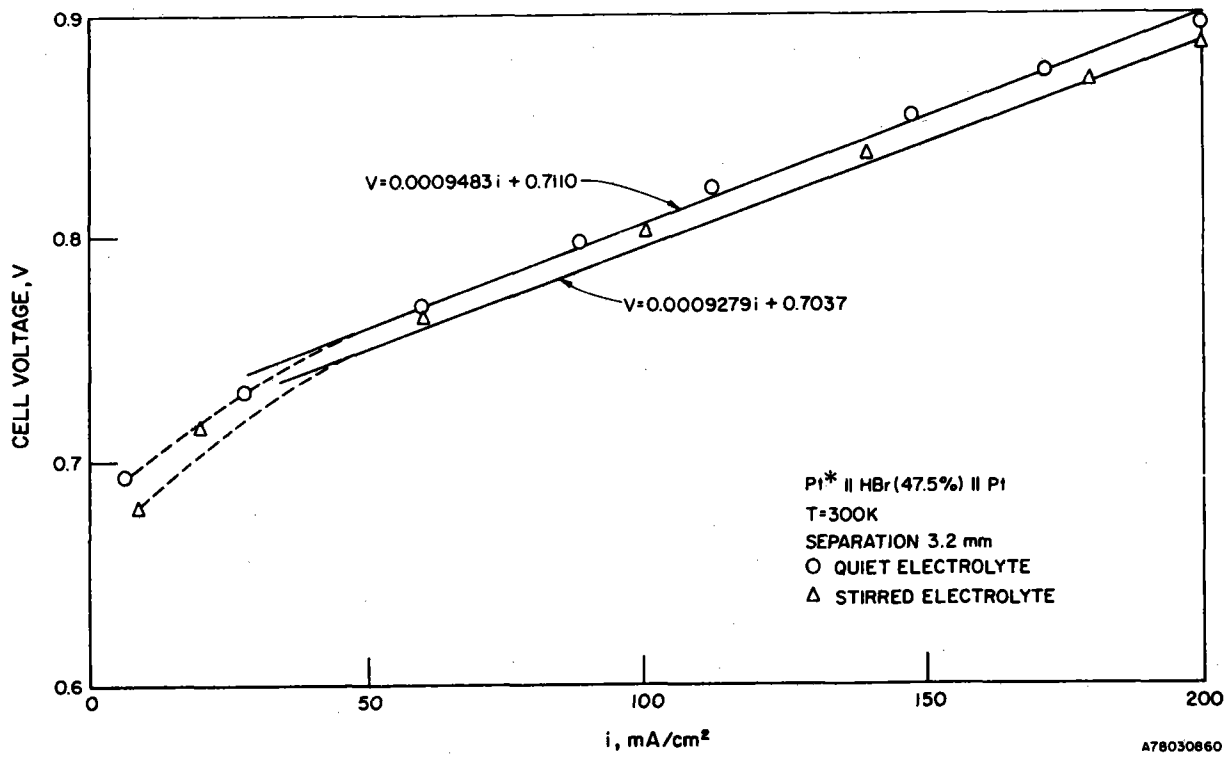

Figure 14. POLARIZATION OF SMOOTH PLATINUM — CATHODE ISOLATION

The evidence from electrolyte stirring experiments indicates that the cathode is more likely to benefit from electrolyte movement than the anode. It also indicates that anode overvoltage probably is not a problem in this system.

A mechanism for anode polarization has previously been suggested. In concentrated Br^- media, the equilibrium,

$$Br^- + Br_2 \rightarrow Br_3^- \qquad (13)$$

is significant and essential (to keep the $Br_2(aq)$ concentration low). Bejarano and Gileadi[19] showed, in the (I_2, I^-) system, that the rate of oxidation of I^- was controlled by a diffusion step. At the electrode surface, the free I_2 depleted available I^- ions, so that the equilibrium —

$$I_2 + I^- \rightarrow I_3^- \qquad (20)$$

was dependent on the rate of I^- ion diffusion from the bulk of the electrolyte to the surface and the free I_2.

The situation for Br^- ion oxidation is, clearly, analogous. Figure 15 shows a one-dimensional conceptualization of the anode/electrolyte interface. The reactions for Br^- ion oxidation and tribromide ion formation are indicated. The thickness of the diffusion region, δ, determines the rate of diffusion of Br^- to the electrode for oxidation. It also determines the rate of diffusion of $Br_2(\ell)$ to a region where the concentration of Br^- ion is great enough to affect formation of Br_3^-. Conceptually, stirring can decrease the thickness of the "stagnant," Br^- ion-free region (δ) and can decrease the transfer time for both Br^- and $Br_2(\ell)$.

Electrolysis on Vitreous Carbon

Electrolysis on vitreous carbon was limited to a critical experiment to determine the relative system voltage and to determine whether it attained low values if glassy carbon was the electrode. A Pt electrode of 1.25 cm^2 area and a glassy carbon beaker, made by the Fluocarbon Co. of Anaheim, California, were used to compare system voltages for $Br_2(\ell)$ and $H_2(g)$ deposition on the carbon surface. A discharge current of 250 mA was used in the comparison. The data are summarized in Table 14.

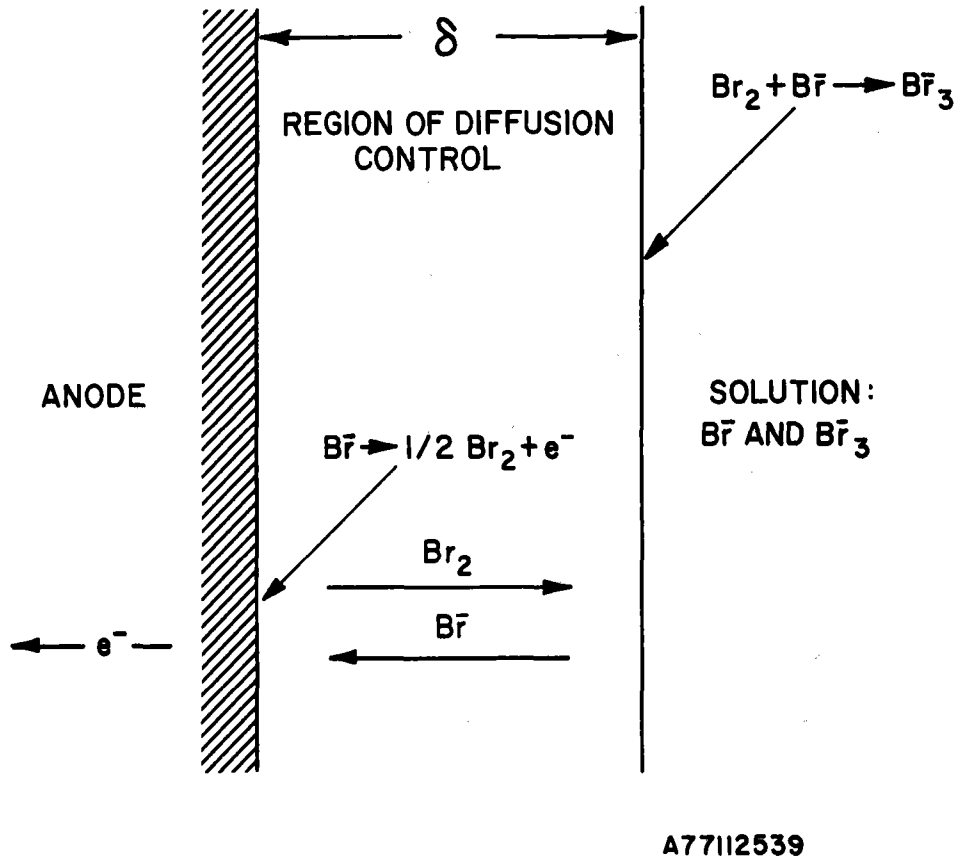

Figure 15. CONCEPTUALIZATION OF AN ANODE LAYER ON A STEADILY DRIVEN OXIDIZING ELECTRODE IN CONCENTRATED HBr

Table 14. SYSTEM VOLTAGES FOR ELECTROLYSIS ON VITREOUS CARBON — (C_v//HBr//Pt):(Pt//HBr//C_v)
(T = 300 K, Separation ~10 mm, Quiet Electrolyte)

Current Density, mA/cm^2		
Anode	Cathode	V, volts
4.7	200.0	1.044
200.0	4.7	1.911
7.2	200.0	1.049
200.0	7.2	1.960
11.5	200.0	1.051
200.0	11.5	2.040

These data show that vitreous carbon is not a promising electrode material. It is much worse than porous graphite for either anode or cathode service, but so clearly inferior to Pt that it should be rejected. In either case, if we apply linear regression analyses to the data from Table 14, we get a decomposition voltage of 1.040 volts for the system C_v//HBr(47.5%)//Pt and 1.823 volts for the system Pt//HBr(47.5%)//C_v, revealing, once more, that the polarization of the cathode (the high decomposition voltage) is the determining factor in HBr electrolysis. Definitive values will not be available until potentiostatic electrolysis is researched, but it is clear that the overvoltage for H_2 evolution on vitreous carbon is much too high to permit the use of this material for efficient HBr electrolysis.

TASK 3. MAXIMUM ATTAINABLE THERMAL EFFICIENCY OF A SPECIFIC BROMINE HYBRID CYCLE

Calculation of "Maximum Attainable" Efficiencies

Much has been published on the subject of efficiency (figure of merit or energy consumption) for thermochemical water-splitting cycles. For details consult the works of Funk et al.,[12,13] Abraham and Schreiner,[20] Chao,[21] Pangborn and Sharer,[22,23] and Fueki[24]. In the IGT program, the "maximum attainable" efficiency for a proposed cycle is calculated by a procedure that accounts for all major heat and work inputs for cycle operation.

$$\text{Efficiency} \equiv \frac{HHV(H_2)}{(\text{process heat input}) + \frac{\text{work input}}{\eta_w}} \qquad (16)$$

where —

$HHV(H_2)$ = high heating value of hydrogen produced = 68.32 kcal/mole

η_w = efficiency of generating work from heat.

This method and similar ones that estimate the upper limit or maximum attainable efficiency are based on cycle operating conditions predicted by thermodynamics. They may be refined by using laboratory operating conditions, but they are not process efficiencies. Attainable efficiencies are used for comparing cycles on a common basis.

The step-by-step procedure used to calculate process heat inputs is shown below.

- Optimum operating temperatures are calculated from available free energy data. Optimum conditions correspond to the temperatures at which the free-energy changes for each reaction are zero or negative. The reaction enthalpies at these temperatures are then calculated from available data.
- A process material flow diagram is constructed and the enthalpies required to heat reactants (to reaction temperatures) and the enthalpies available from cooling reaction products are calculated.

- If the stream temperatures allow, enthalpy available from product streams and exothermic reactions is matched against enthalpy required for reactant streams and endothermic reactions to minimize external heat inputs. The matching procedure is optimized by inspection. The total process heat requirements are the unmatched enthalpy requirements.

Driving forces for chemical reactions are assumed to be the primary work inputs and are calculated for the cases outlined below.

- Electrochemical steps are assumed to be 80% efficient and operated with 125% of the ideal free-energy requirement (as electricity).

- Thermochemical steps with two or more gases involved are supplied with the reversible work required for gas separation. An equilibrium composition is calculated from Equation 21 —

$$\Delta G_{Rx} = -RT \ln K_p \qquad (21)$$

where

ΔG_{Rx} = Gibbs free-energy change for the reaction (at T)

K_p = equilibrium constant assuming unit fugacity of solids and liquids.

Equation 21 is then used to calculate the reversible work of separation —

$$\Delta G_{sep} = RT \sum_i n_i \ln y_i$$

where

ΔG_{sep} = reversible work required for gas separation

R = gas constant (per mole)

T = absolute temperature at which separation is made

n_i = moles of component i present (at equilibrium)

y_i = mole fraction of component i (at equilibrium).

- Thermochemical steps with less than two gases involved are assumed to be driven by an undefined mechanism with a work input equal to the reaction free-energy change if that change is positive. If the reaction free-energy change is zero or negative, the reaction is assumed to proceed spontaneously without a work input.

We have now determined both the process heat input and the work input for a given cycle; only the value of η_w (from Equation 16 — the efficiency of

generating work from heat) needs to be specified in order to calculate a maximum attainable efficiency from Equation 16. We have used two conventions to determine values for η_w. The first corresponds to current technology and assumes a heat-to-work efficiency that is 50% of the Carnot efficiency.

$$\eta_w = 0.5\ [(T_1 - T_2)/T_1] \tag{23}$$

where T_1 is the highest temperature of process heat acceptance and T_2 is the power-cycle waste-heat temperature (arbitrarily assumed to be 400 K). The second convention corresponds to future technology and is calculated using a temperature-dependent coefficient of the Carnot efficiency —

$$\eta_w = \eta_T\ [(T_1 - T_2)/T_1]. \tag{24}$$

The values of η_T are dependent on T_1 as follows:

T_1, K	η_T
700	0.65
800	0.67
900	0.68
1000	0.69
1100	0.68
1200	0.68
1300	0.67
1400	0.66

Therefore, we calculate two values of the maximum attainable efficiency of cycles, via Equation 16. These values differ only by our assumption of current or future technology heat-to-work conversion efficiencies. Assumptions implicit in our analysis are listed below.

- All pertinent reactions attain equilibrium.
- The enthalpy output of an exothermic reaction is 100% heat.
- All reactions are carried out at 1-atm pressure.
- During heat matching we assume
  - Perfect heat transfer (that is, the close approach of the temperatures in the exchanges. We do not violate the second law, but as ΔT approaches zero, the heat exchanger areas must become very large.)
  - Negligible work requirements for gas flow, pressure drops, liquid pumping, and solids transfer.

- The reaction products were in different (separate) phases or gas separations were made with only the ideal work requirement.
- Energy for materials transport was negligible or was less than the excess entropy supplied to endothermic steps, which is always given both the total enthalpy (as heat) plus at least the free energy (as work).

The specific cycle under study, the EURATOM Mark-13, is given by Equations 9 through 11, and summarized below:

Reaction		T, K
1	$SO_2(g) + Br_2(g) + 2H_2O(g) \rightarrow H_2SO_4(\ell) + 2HBr(g)$	433
2	$2HBr(aq) \rightarrow H_2(g) + Br_2(\ell)$ (electrolysis)	298
3	$H_2SO_4(g) \rightarrow H_2O(g) + SO_2(g) + 1/2\ O_2(g)$	1150

Thermodynamic Quantities

Reaction No.	ΔG	ΔH	W	ΔG_{sep}
	kcal/mole			
1	−0.41	−30.85	4.86	4.86
2	25.57	17.42	31.96	--
3	−19.29	45.53	1.00	1.00

The energy requirement for work, therefore, is 37.82 kcal/mole H_2.

Material Flow Pattern

The reactions for the Mark-13 cycle and the streams for heat matching are identified in Figure 16.

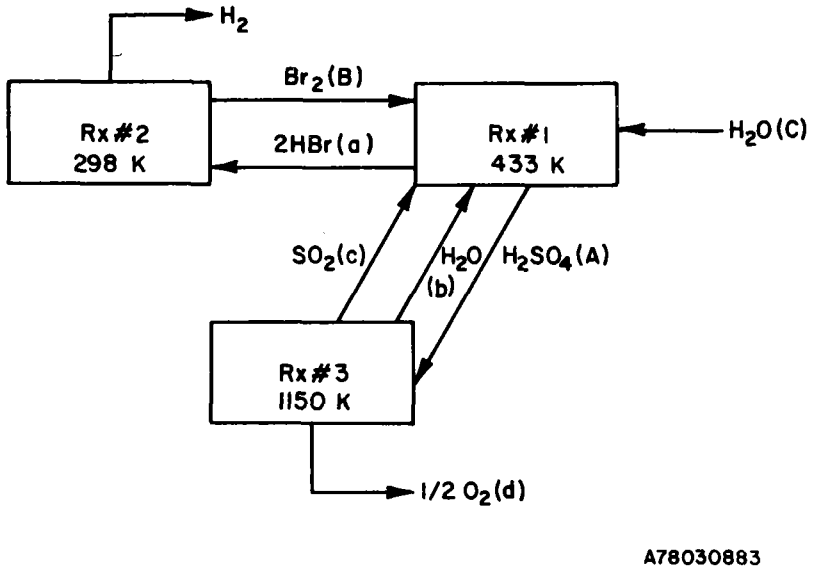

Figure 16. MATERIAL FLOW PATTERN FOR EURATOM CYCLE MARK-13

Summary of Required Heat

Reaction, Rx, or Stream	Temperature, K	kcal/mole
A_3	609	13.39
B_3	333	7.06
C_3	373	9.77
Rx 2	298	17.42
Rx 3	1150	45.53
C_{12}	298 → 373	
	373 → 433	1.84
B_{12}	298 → 333	
	333 → 433	1.51
A_{12}	433 → 609	
	609 → 1150	23.32
		119.84

The enthalpy balance — heat required plus heat available — is 119.84 − 51.47 = 68.37.

Heat Matching

The enthalpy of reaction for Rx#1 is used to heat the feedstocks to Reactor 1 (B_3, C_3, C_{12}, B_{12}), to leave a heat surplus of −10.67 kcal/mole.

The hot $O_2(g)$, $SO_2(g)$, and $H_2O(g)$ streams from Rx#3 are used to preheat the $H_2SO_4(\ell)$ stream (A_{12}) from the main solution reaction, Rx#1. If we account for −0.53 kcal/mole remaining in the vented oxygen, there is an unmatched heat of +5.05 kcal/mole, in the A_{12} stream. The remaining available heat [−0.53 kcal/mole from the vented O_2, the heat in the $Br_2(g)$ from Rx#1 and the remaining heat (-10.67 kcal/mole) from ΔH(Rx#1)] are used to match the demands of Rx#2 (17.42 kcal/mole), leaving an unmatched heat of 4.4 kcal/mole.

After matching, the required heats are:

Rx#2	4.4	kcal/mole
A_3	13.39	kcal/mole
Rx#3	45.53	kcal/mole
A_{12}	5.05	kcal/mole
	68.37	kcal/mole

and the required process heat for substitution into Equation 16 is 68.37 kcal/mole. The heat required for conversion to work, to be calculated for current technology (CT) and future technology (FT) is 37.82 kcal/mole. These modified values are —

CT: (37.82/0.5)(1150/1150-400) = 115.98 kcal

FT: (37.82/0.67)(1150/1150-400) = 86.55 kcal

Therefore, the calculated attainable efficiencies are —

CT: 68.32/(68.37 + 115.98) = 37.1%

FT: 68.32/(68.37 + 86.55) = 44.1%

Summary of Heat Available

Reaction, Rx, or Stream	Temperature, K	kcal/mole
1	433	−30.85
(a)	298 → 433	− 1.82
(b)	1150 → 433	− 6.62
(c)	1150 → 433	− 8.83
(d)	1150 → 298	− 3.35
		−51.47

TASK 4. DEVELOPMENT OF ELECTROLYZER ELEMENTS FOR H_2SO_3

The objective of this task is to investigate the electrolytic oxidation of sulfurous acid (H_2SO_3) to sulfuric acid (H_2SO_4) and hydrogen. Our study dealt with sulfuric acid concentrations less than or equal to 50 wt % in order to determine a range of sulfuric acid concentrations most appropriate for thermochemical water-splitting cycles involving this electrolytic step. We compared measured cell voltages with that of direct water electrolysis. Our work was also designed to identify potential problems for future study.

Background Information

The electrolytic oxidation of H_2SO_3 (Reaction 25) can be represented by the following half-cell reactions (Reactions 26 and 27):

$$H_2SO_3(aq) + H_2O(\ell) \rightarrow H_2SO_4(aq) + H_2(g) \quad (25)$$

$$H_2SO_3 + H_2O \rightarrow H_2SO_4 + 2H^+ + 2e^- \quad (26)$$

$$2H^+ + 2e^- \rightarrow H_2 \quad (27)$$

Reaction 26 takes place at the positive electrode, and Reaction 27 takes place at the negative electrode. The reversible cell voltage for Reaction 25 is 0.17 V, which corresponds to the potential for Reaction 25 with all species at unit activity. However, a practical cell voltage will exceed this value due to activation polarization at both electrodes, ohmic polarization, and concentration polarization. All of these polarizations will contribute to a working cell voltage in excess of the theoretical 0.17 V. In this program, we measured the anodic and cathodic activation polarizations as functions of sulfuric acid concentration.

Reaction 25 is part of the hydrogen-producing step in IGT's copper oxide-copper sulfate water-splitting cycle, H-5. In that cycle, the sulfuric acid produced at the positive electrode reacts with copper oxide to produce copper sulfate. Copper sulfate is thermally decomposed to regenerate copper oxide; $SO_3(g)$ is also a product of this decomposition. At a higher temperature, the $SO_3(g)$ decomposes to $SO_2(g)$ and product oxygen. SO_2 is returned to the electrolyzer to complete the cycle. A complete description of Cycle H-5 is provided in the discussion of Task 1 in this report.

Experimental Procedure

Sulfurous acid (or any other sulfite species) must be isolated from the negative electrode to avoid its reduction to elemental sulfur via Reaction 28.

$$H_2SO_3 + 4H^+ + 4e^- \rightarrow S + 3H_2O \qquad (28)$$

Therefore, our experimental cell has separate anode and cathode compartments, and SO_2 is only introduced into the anode (positive) compartment. The two compartments are separated by a relatively long distance (17 cm) with a fritted glass separator at the midpoint. H_2SO_3 diffuses from the positive to the negative compartment in 1 to 3 hours, but all data are generated before a white precipitate (elemental sulfur) begins to appear in the negative compartment. Figure 17 is a schematic diagram of the H-type cell used in our experiments.

The positive and negative electrodes are cylindrical, 45-mesh platinum gauze, each with an apparent area (circumference multiplied by height) of 39 cm^2. The actual surface area of each electrode is estimated to be 58 cm^2. Half-cell potentials were measured at various current levels using a mercury-mercurous sulfate reference electrode and Luggin capillary. The electrolyte in the reference was kept at the same sulfuric acid concentration as that in the cell during each experiment. Currents through the cell were maintained by a Hewlett Packard constant current-constant voltage power supply. Potentials were measured by a Keithley 616 electrometer, which has an input impedance of 10^{14} ohms. All measurements were made at 297 K ± 1 K.

The electrodes were thoroughly cleaned before use by heating them (red-hot) in a methane-oxygen flame to burn off all organic and volatile materials; they were then soaked in concentrated sulfuric acid for several hours and, finally, rinsed in deionized water. After inserting the electrodes into the cell, a current of 50 to 100 mA was impressed for at least 20 minutes to stabilize them before any data were generated.

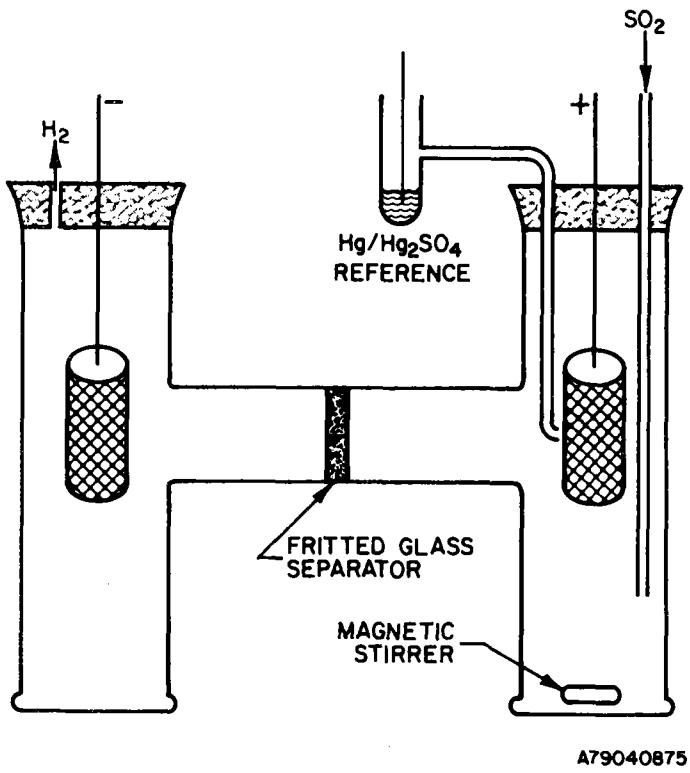

Figure 17. EXPERIMENTAL CELL FOR THE ELECTROLYTIC OXIDATION OF H_2SO_3

All measurements were made using 8%, 19%, 33%, and 50% (by weight) sulfuric acid solutions as the electrolyte. Half-cell potentials at the positive electrode were measured as a function of impressed current in SO_2-free solutions first. In the absence of SO_2, direct water-splitting was accomplished. Gaseous hydrogen was produced at the negative electrode, and oxygen was produced at the positive electrode. After these measurements were completed, the cell was set on open circuit for at least 2 hours to allow all oxygen to escape. The positive compartment was then saturated with $SO_2(g)$ [to form $H_2SO_3(aq)$], and the current versus half-cell potential measurements were repeated. During these measurements, a constant $SO_2(g)$ sparge was maintained to ensure saturation. The data presented in this report are average values of at least three experiments. The difference in measured half-cell potentials between duplicate experiments was only a few mV in most cases. The maximum difference was 15 mV.

Results and Discussion

In this program, we measured the anodic and cathodic activation polarizations in order to estimate the total cell voltage. The other major component of overall cell voltage, ohmic polarization, will be dealt with in future programs.

Half-cell potentials as functions of impressed currents at the positive electrode in 8%, 19%, 33%, and 50% (by weight) sulfuric acid solutions in the presence and absence of SO_2 are shown in Figures 18, 19, 20, and 21, respectively. It can be seen from these figures that, in all the solutions, the potential difference between the SO_2-free and SO_2-saturated solutions was about 1.3 V. This is due to the fact that the reaction going on at the electrode surface when the solution is SO_2-free is direct water-splitting, which produces oxygen at the positive electrode and has a more positive potential. When the solution is saturated with SO_2, the reaction at the electrode surface is oxidation of $SO_3^{=}$ to produce $SO_4^{=}$, which has a less positive potential. If an ordinary water electrolysis cell has a cell operating voltage of 1.8 to 2.0, our data show that, by introducing SO_2 into the cell, the cell voltage should drop to about 0.5 to 0.7. This is illustrated in Figure 22. This estimation is based on the assumption that the activation polarization at the negative electrode and ohmic polarization in the two systems (with and without SO_2) are the same. The energy consumed for hydrogen production via Reaction 25 is, therefore, only 28% to 35% that required for direct water-splitting (1.8 to 2.0 V) in conventional alkali or acid cells.

To show the effect of sulfuric-acid concentration on the potential of the positive electrode, we replotted the data from Figure 21 on a semi-logarithmic scale (Figure 23). The potential of the positive electrode in SO_2-saturated solution becomes less positive as the concentration of sulfuric solution decreases from 50% to 8%. This trend suggests that the least concentrated electrolyte, which yields the lowest activation polarization at the positive electrode, will also yield the lowest overall cell voltage. However, the decrease in activation polarization will be partially offset by an increase in ohmic polarization at very-low-acid concentrations. Also, experiments conducted in 8% sulfuric acid at an impressed current of 500 mA

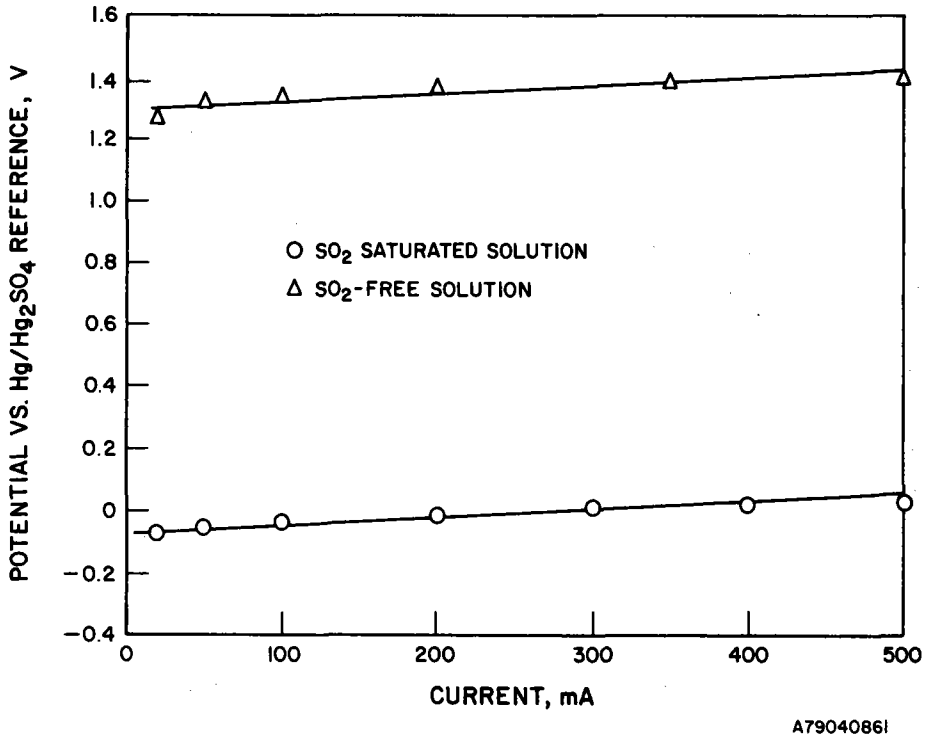

Figure 18. ANODIC POTENTIAL IN THE PRESENCE AND ABSENCE OF SO_2 IN 8% H_2SO_4 AT 298 K

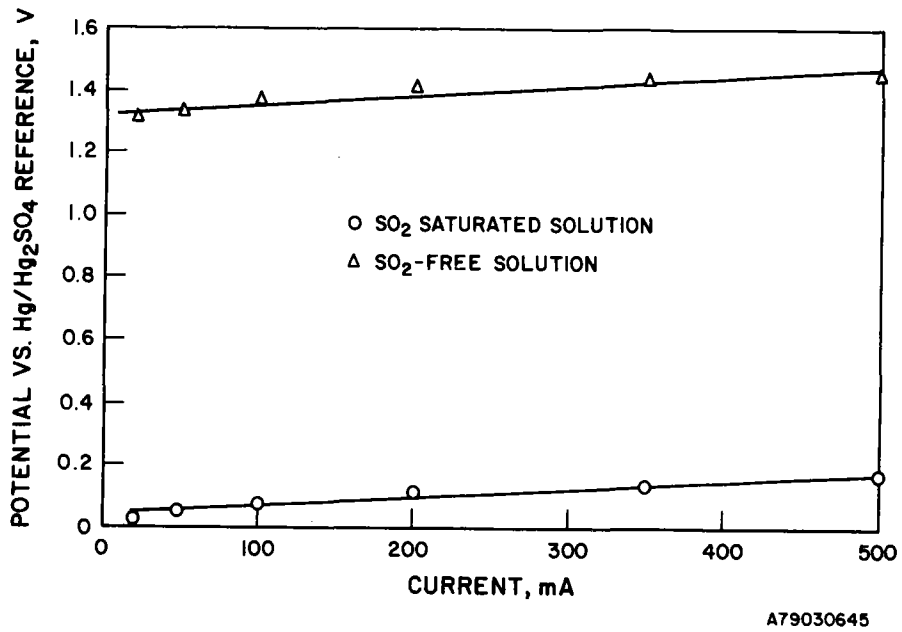

Figure 19. ANODIC POTENTIAL IN THE PRESENCE AND ABSENCE OF SO_2 IN 19% H_2SO_4 AT 298 K

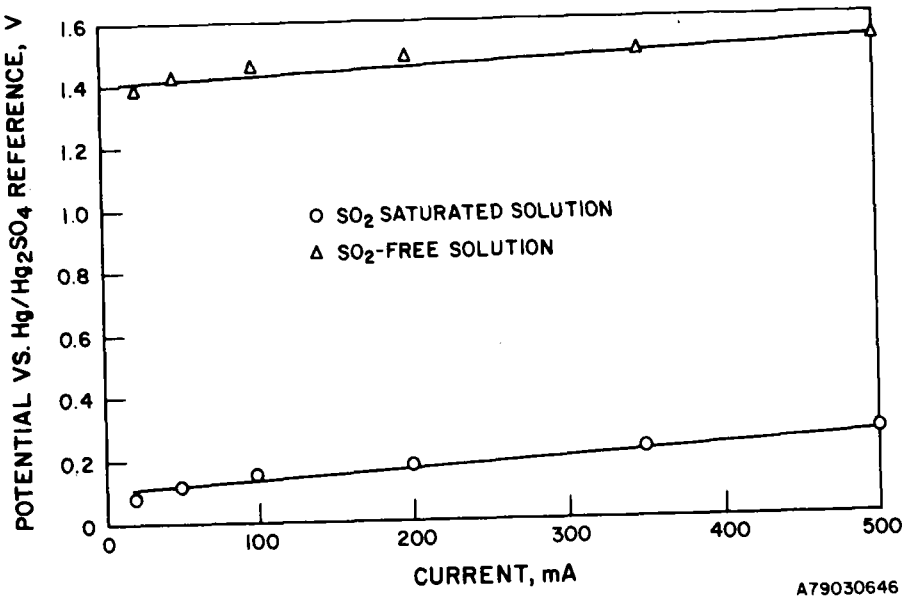

Figure 20. ANODIC POTENTIAL IN THE PRESENCE AND ABSENCE OF SO_2 IN 33% H_2SO_4 AT 298 K

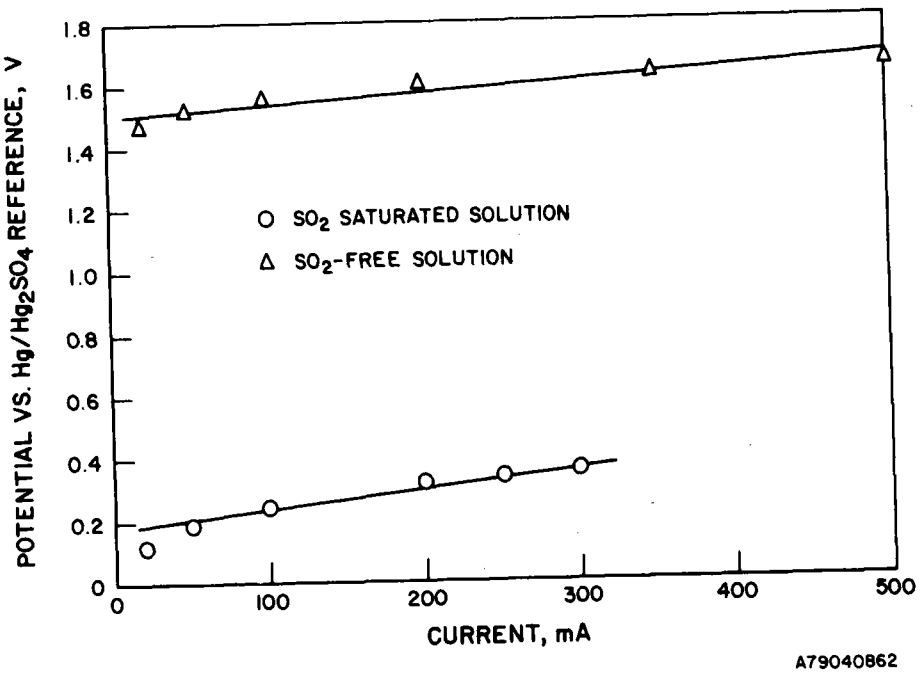

Figure 21. ANODIC POTENTIAL IN THE PRESENCE AND ABSENCE OF SO_2 IN 50% H_2SO_4 AT 298 K

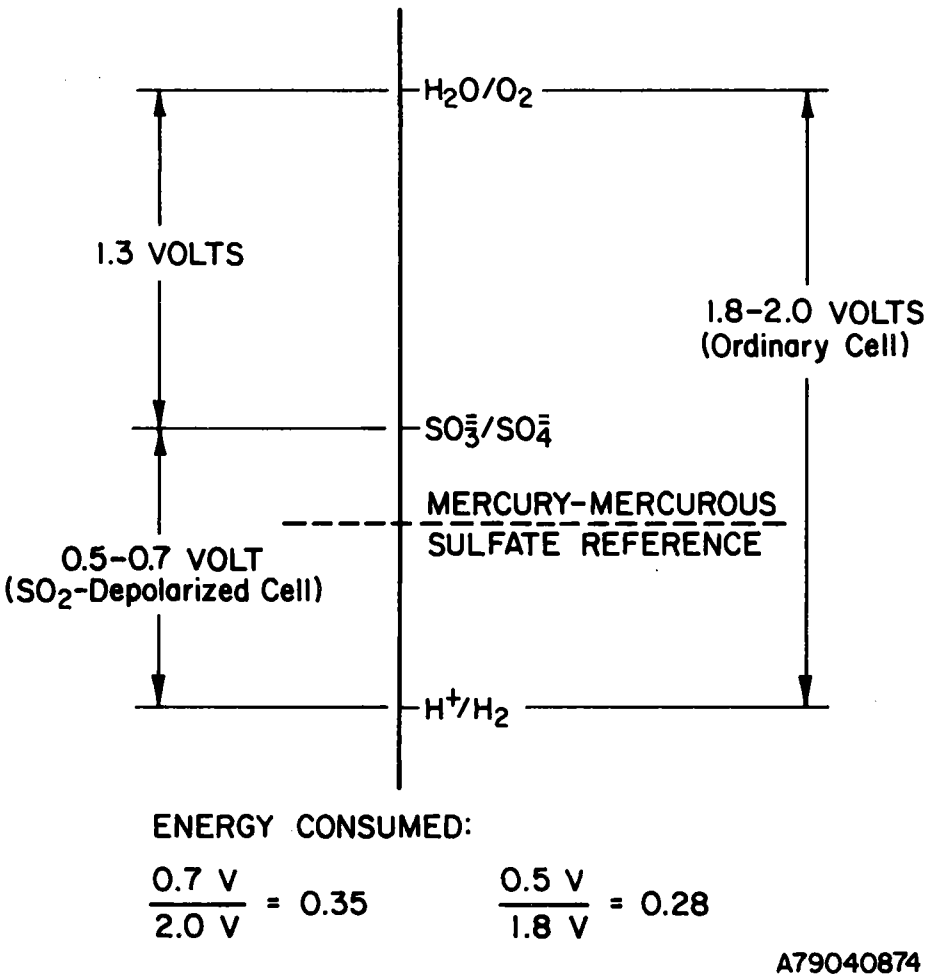

Figure 22. ORDINARY WATER ELECTROLYSIS CELL VOLTAGE AND SO_2-DEPOLARIZER CELL VOLTAGE

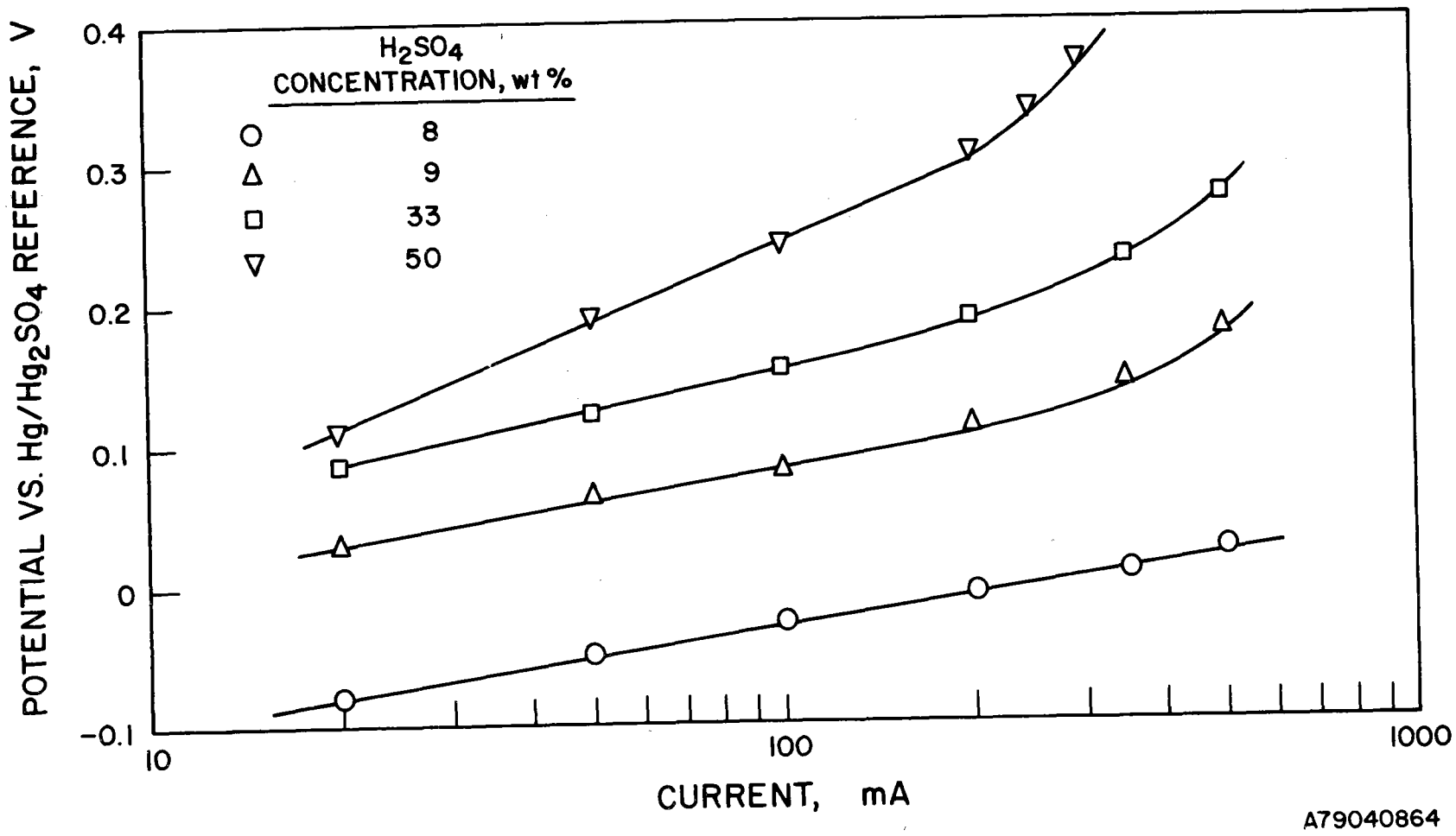

Figure 23. ANODIC OXIDATION OF SO_2 IN DIFFERENT CONCENTRATIONS OF H_2SO_4 AT 298 K

produced white precipitate (sulfur) in both positive and negative cell compartments in less than 5 minutes. Some sulfur production is expected in the negative compartment after H_2SO_3 diffuses there from the positive compartment, but this takes hours — not 5 minutes. Sulfur production in the positive compartment was not observed in the 19%, 33%, or 50% acid systems at any time. Although our data do not allow us to deduce the mechanism for sulfur production in the 8% acid system, it appears that there is a lower practical limit on sulfuric-acid concentration during the electrolytic oxidation of H_2SO_3.

Several experiments (at an impressed current of 500 mA) were conducted with initially SO_2-saturated positive compartments and no SO_2 sparge to examine the behavior of the positive half-cell potential as the SO_2 [H_2SO_4(aq)] concentration decreases. Figure 24 is a plot of half-cell potential versus time for 19% and 50% sulfuric acid electrolytes. Potential curves for both systems increase quickly, from less than 0.5 V to more than 1.4 V at some time. The higher potential indicates that the actual cell reaction was shifted from Reaction 25 to direct water-splitting as H_2SO_4 is depleted. That shift takes place in less than 10 minutes in 50% sulfuric acid, but it takes more than 40 minutes in 19% acid at the same 500-mA current. The most logical explanation for the time difference is that the initial concentration (solubility) of SO_2 is more than 4 times higher in 19% H_2SO_4 than in 50% H_2SO_4. Figure 25, a plot of SO_2 solubility versus H_2SO_4 concentration, indicates that the actual solubility ratio is only about 1.1. Therefore, the difference in the points at which the potential curves shift is influenced by something other than the different solubilities of SO_2 in 19% and 50% H_2SO_4. This phenomenon should be investigated in future work.

From Figure 23, we calculated the Tafel slopes for the anodic oxidation of SO_2 (Reaction 26) for all four sulfuric acid concentrations. In 8%, 19%, and 33% sulfuric acid, the Tafel slopes are all 88 mV per decade of applied current. In 50% H_2SO_4, the Tafel slope is much larger, 185 mV per decade, indicating that the half-cell reaction in more concentrated acid is more complex.

From the above discussion, it appears that the optimum anodic sulfuric acid concentration is between 8% and 50%. In that range, we have data only at two points, 19% and 33%. In order to determine a more exact optimum,

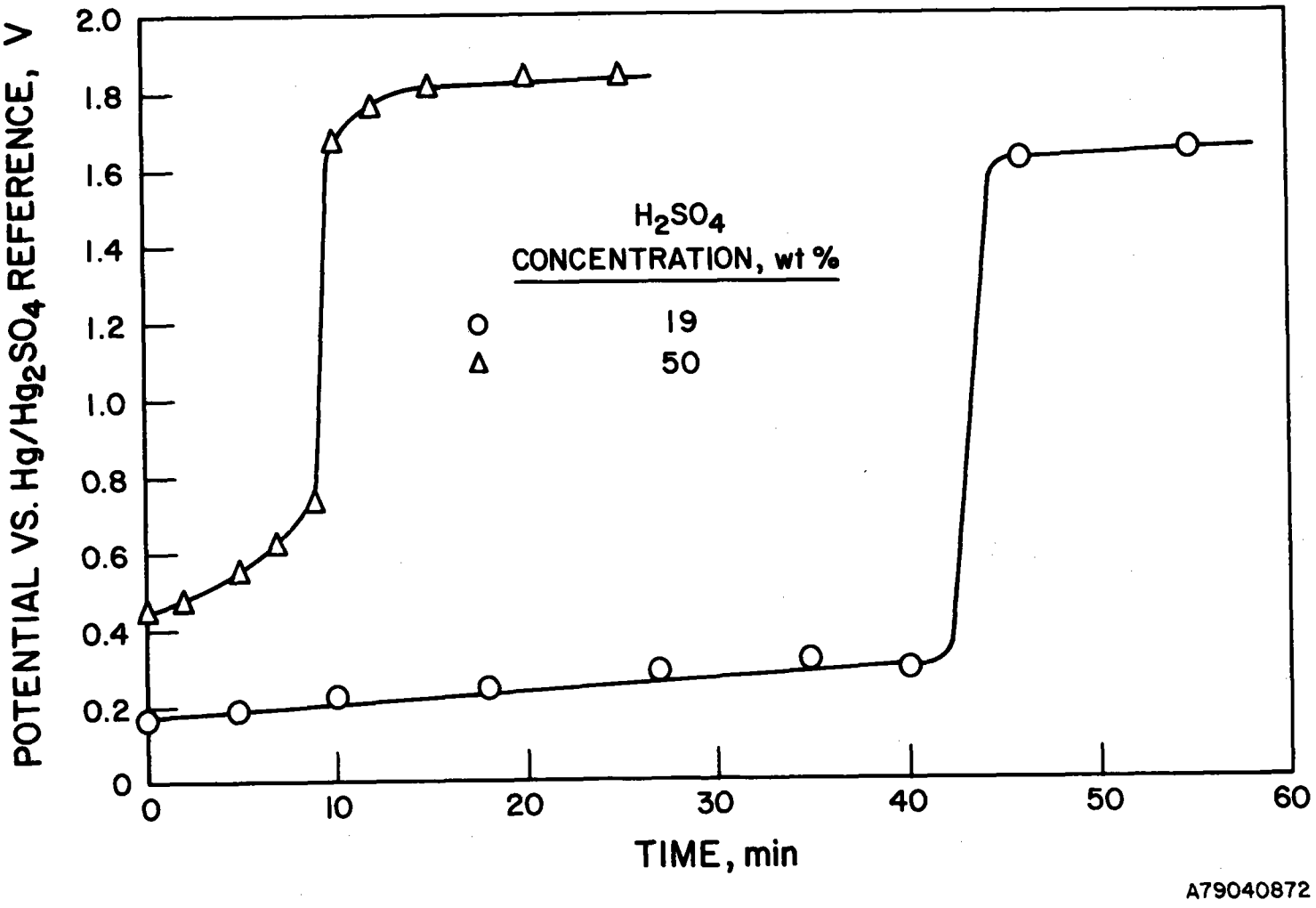

Figure 24. THE BEHAVIOR OF SO_2-SATURATED SULFURIC ACID SOLUTION UNDER 500 mA CURRENT AT 298 K

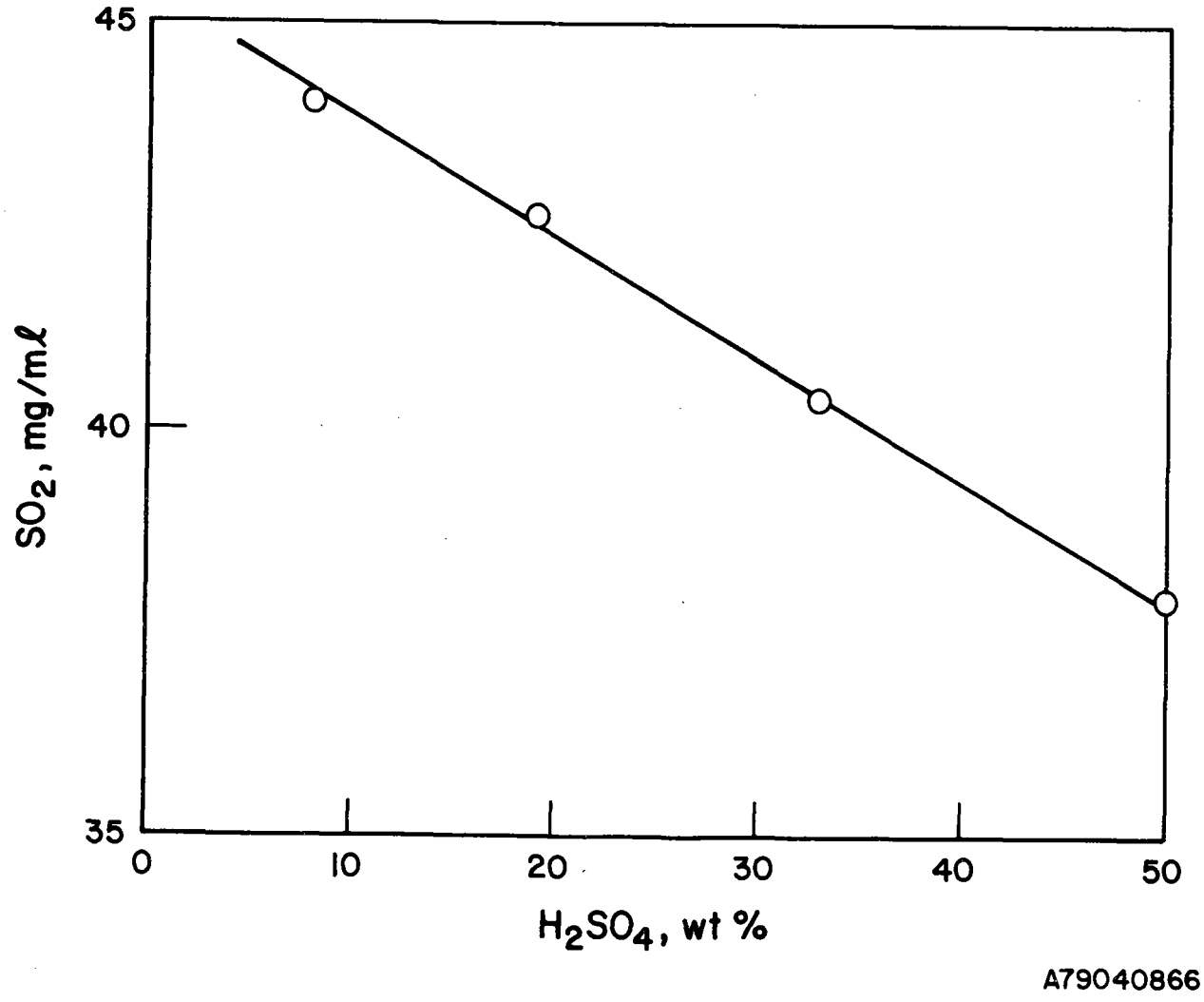

Figure 25. SOLUBILITY OF SO_2 IN VARIOUS CONCENTRATIONS OF SULFURIC ACID SOLUTION AT 298 K

one would need to obtain data at a few more H_2SO_4 concentrations and combine that data with the effect of acid concentration on ohmic polarization.

The activation polarization of the cathodic reaction (hydrogen production) was measured in 33 weight percent sulfuric acid using the techniques described above. Two types of cathodes were used in these experiments: In one set of experiments, we used a planar platinum screen with an apparent area of about 11 cm^2. In a second set of experiments, the cylindrical platinum gauze used before was retained (about 39 cm^2 apparent area). Figure 26 is a plot of cathodic half-cell potential versus current for these experiments. The polarization on the cylindrical gauze, which has the larger surface area, is lower than that on the flat screen. However, if we correct the difference in surface area by using current density per apparent unit surface area and compare the potential on the two electrodes, the one with cylindrical gauze is still lower. It appears that the shape of the cathode may affect polarization for the hydrogen-producing reaction, and, therefore, overall cell performance. We plan to investigate parameters that affect cathode polarization in future work.

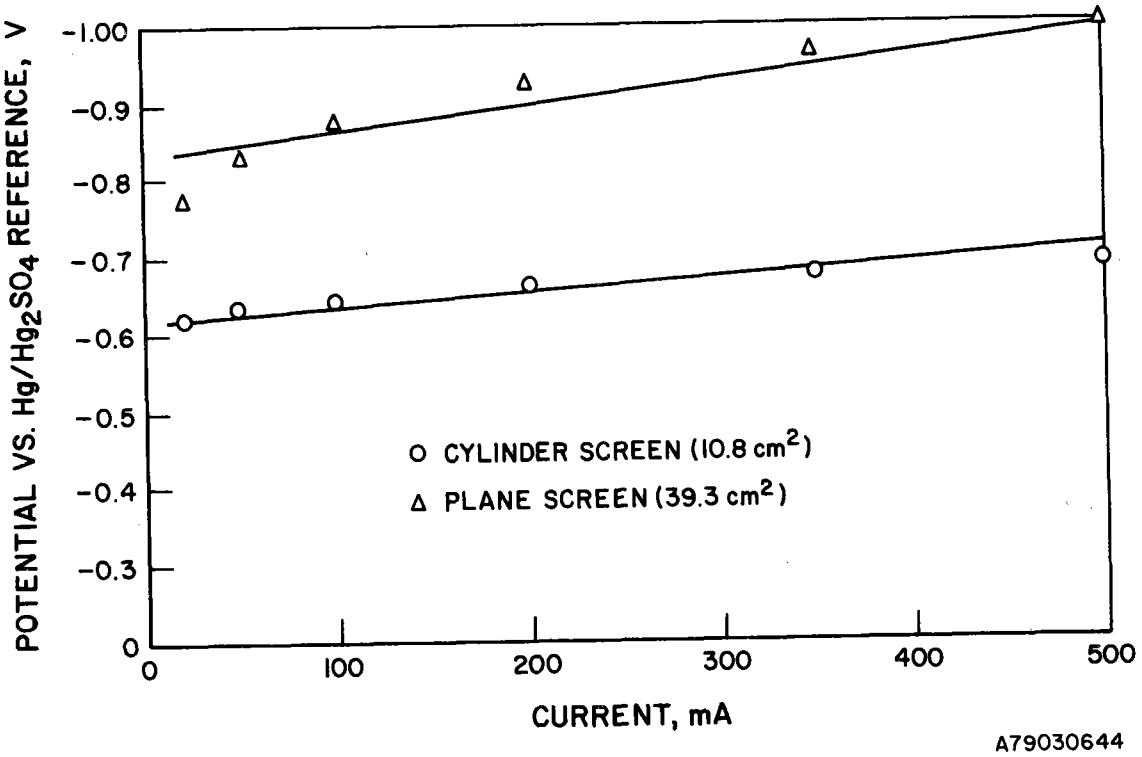

Figure 26. CATHODIC POTENTIALS WITH DIFFERENT ELECTRODES IN 33% H_2SO_4 AT 298 K

TASK 5. FEASIBILITY OF HIGH-TEMPERATURE REFERENCE-STATE THERMOCHEMICAL CYCLES

We examined lists of thermodynamics data and derived seven members of the metal-metal oxide class of cycles, and six members of the metal oxide-metal sulfate class of cycles. These cycles require heat inputs at temperatures above the level (1150 K) considered achievable by high-temperature nuclear-fission reactors (HTR's), and might, therefore, be driven by a high-temperature solar (or nuclear fusion) primary heat source.

Metal-Metal Oxide Cycles

A general metal-metal oxide is shown below as Reactions 29 and 30:

$$M + H_2O \rightarrow MO + H_2 \qquad (29)$$

$$MO \rightarrow M + \tfrac{1}{2}O_2 \qquad (30)$$

where M denotes a metal or reduced metal oxide and MO denotes the oxidized form of M. No known member of the metal-metal oxide class of cycles is feasible at the temperatures available from HTR's. A metal or reduced metal oxide (M) reactive enough to split water forms an oxide too stable to be thermally decomposed below 1150 K. We used IGT's computerized program (HYDRGN) to assess the maximum attainable efficiencies of the seven newly derived cycles. As expected, these high-temperature, two-step processes have very attractive efficiencies.

Pure Thermochemical Cycles

Three of the seven cycles derived are feasible with thermal-driving forces only (pure thermochemical). The tin oxide cycle (Reactions 31 and 32) has been designated Cycle R-1.

$$SnO(s) + H_2O(g) \rightarrow SnO_2(s) + H_2(g) \qquad (31)$$

$$SnO_2(s) \rightarrow SnO(g) + \tfrac{1}{2}O_2(g) \qquad (32)$$

The zinc cycle (Reactions 33 and 34) has been designated Cycle Q-2.

$$Zn(g) + H_2O \rightarrow ZnO(s) + H_2(g) \qquad (33)$$

$$ZnO(s) \rightarrow Zn(g) + \tfrac{1}{2}O_2(g) \qquad (34)$$

The iron oxide cycle (Reactions 35 and 36) has been designated Cycle B-17.

$$3FeO(s) + H_2O(g) \rightarrow Fe_3O_4(s) + H_2(g) \quad (35)$$

$$Fe_3O_4(s) \rightarrow 3FeO(\ell) + \tfrac{1}{2}O_2(g) \quad (36)$$

Table 15 is a summary of the thermodynamic properties of Cycles R-1, Q-2, and B-17. The temperatures listed for each reaction correspond roughly to the point where their Gibbs free-energy changes are zero. (These are the temperatures used in our maximum attainable efficiency calculations.) Table 15 also summarizes enthalpy changes and the theoretical work of separation for each reaction.

Table 15. THERMODYNAMICS DATA FOR CYCLES R-1, Q-2, AND B-17

Cycle	Reaction	Temp, K	ΔG	ΔH	Work Required
			kcal		
R-1	$SnO(s) + H_2O(g) \rightarrow SnO_2(s) + H_2(g)$	937	−0.38	−9.49	1.10
	$SnO_2(s) \rightarrow SnO(g) + \tfrac{1}{2}O_2(g)$	2325	−0.03	125.32	0.76
Q-2	$Zn(g) + H_2O(g) \rightarrow ZnO(s) + H_2(g)$	1489	0.00	−50.70	2.12
	$ZnO(s) \rightarrow Zn(g) + \tfrac{1}{2}O_2(g)$	2245	4.05	107.49	2.10
B-17	$3FeO(s) + H_2O(g) \rightarrow Fe_3O_4(s) + H_2(g)$	684	0.08	−12.28	1.10
	$Fe_3O_4(s) \rightarrow 3FeO(\ell) + \tfrac{1}{2}O_2(g)$	2257	0.02	89.10	0.02

The free-energy changes of the high-temperature, oxygen-producing reactions (Nos. 32, 34, and 36) decrease with increasing temperatures. Temperatures of at least 2200 to 2400 K will be required to produce oxygen at 1 atmosphere, avoiding the necessity of providing work to drive reactions with unfavorable equilibria. The thermal decomposition of zinc oxide in Cycle Q-2 (Reaction 34) has been successfully demonstrated using direct solar heat from the solar furnace at Odiello, France.

The free-energy changes for the lower-temperature, hydrogen-producing steps (Reactions 31, 33, and 35) increase with increasing temperatures. These reactions can, therefore, be operated at temperatures ranging from ambient to the temperatures indicated in Table 15, where ΔG_{rx} is equal to zero. If operated at temperatures lower than those indicated in Table 15, these reactions will have a negative free-energy change and will produce equilibrium

hydrogen pressures in excess of 1 atmosphere. Therefore, Cycles R-1, Q-2, and B-17 should be capable of producing pressurized hydrogen to at least partially avoid the cost of hydrogen compression to pipeline pressures.

Table 16 is a summary of the maximum attainable efficiency calculations performed for Cycles R-1, Q-2, and B-17. The maximum attainable efficiencies (ranging from 66% to 86%) are all attractive. The heat requirements shown in Table 16 are primarily for high-temperature isothermal heat to drive the endothermic (oxygen-producing) steps. An interesting feature of all three cycles is that they produce more work than is required for gas separations; this results from the fact that the exothermic (hydrogen-producing) reactions reject heat at temperatures much higher than our normally assumed heat-sink temperature of 400 K. Therefore, unlike cycles with lower temperature exothermic steps, essentially all of the heat rejected can be used for work generation. Maximum attainable efficiencies for these cycles were calculated by dividing the process outputs (hydrogen's HHV and the excess work generated) by the primary source heat requirements.

Table 16. MAXIMUM ATTAINABLE EFFICIENCIES FOR CYCLES R-1, Q-2, AND B-17

Cycle	Heat Required as Heat	Work Required	Work Available		Efficiency	
			CT	FT	CT	FT
	kcal				%	
R-1	135.8	1.9	23.4	30.9	66.2	71.7
Q-2	111.7	4.2	15.8	20.9	71.5	76.1
B-17	91.4	1.1	8.7	11.5	83.0	86.1

Overall, Cycles R-1, Q-2, and B-17 are attractive solar cycles: Efficiencies are high, chemical processing is relatively simple, gas-phase separations are minimal and involve species with large differences in boiling points, and all are capable of producing hydrogen at elevated pressure.

Hybrid Thermoelectrochemical Cycles

We derived four hybrid members of the metal-metal oxide class of cycles, which are similar to the high-temperature solar cycles already discussed except that their hydrogen-producing reactions will require an electrochemical driving force. The maximum attainable efficiencies of the four cycles were assessed. We discovered that two of the cycles, the cerium oxide cycle and

the selenium oxide cycle, were unfeasible because of unstable products; these were not pursued further.

The manganese oxide cycle (Reactions 37 and 38) has been designated Cycle F-8.

$$3MnO(s) + H_2O(\ell) \rightarrow Mn_3O_4(s) + H_2(g) \quad (37)$$

$$Mn_3O_4(s) \rightarrow 3MnO(s) + \tfrac{1}{2}O_2(g) \quad (38)$$

The iron oxide cycle (Reactions 39 and 40) has been designated Cycle B-18.

$$2Fe_3O_4(s) + H_2O(\ell) \rightarrow 3Fe_2O_3(s) + H_2(g) \quad (39)$$

$$3Fe_2O_3(s) \rightarrow 2Fe_3O_4(s) + \tfrac{1}{2}O_2(g) \quad (40)$$

Table 17 is a summary of the thermodynamic properties of Cycles F-8 and B-18. Free-energy and enthalpy changes, work requirements, and temperatures (used in the efficiency calculations) are shown for each reaction. In calculating a cycle's maximum attainable efficiency, we assume electrolysis at 80% efficiency; therefore, the work requirements for the electrochemical hydrogen-producing steps (Reactions 37 and 39) are shown as the free-energy change of the reaction divided by 0.8. Because the pressure coefficient of the cell voltage (from the Nernst equation) is small (~0.003 V/atm), production of hydrogen at elevated pressures should not lower the calculated cycle efficiencies (which assume 1 atmosphere) significantly. The free-energy changes of the high-temperature, oxygen-producing Reactions 38 and 40 decrease as temperatures increase. Therefore, temperatures equal to or greater than those shown in Table 18 will be required to produce oxygen partial pressures of 1 atmosphere or greater.

Table 17. THERMODYNAMICS DATA FOR CYCLES F-8 AND B-18

Cycle	Reaction	Temp, K	ΔG	ΔH	Work Required
			kcal		
F-8	$3MnO(s) + H_2O(\ell) \rightarrow Mn_3O_4(s) + H_2(g)$	298	11.10	2.41	11.10/0.8
	$Mn_3O_4(s) \rightarrow 3MnO(s) + \tfrac{1}{2}O_2(g)$	1825	−5.51	52.80	0.00
B-18	$2Fe_3O_4(s) + H_2O(\ell) \rightarrow 3Fe_2O_3(s) + H_2(g)$	298	9.91	12.22	9.91/0.8
	$3Fe_2O_3(s) \rightarrow 2Fe_3O_4(s) + \tfrac{1}{2}O_2(g)$	1735	0.35	55.27	0.35

Table 18 is a summary of the maximum attainable calculations performed for Cycles F-8 and B-18. Heat requirements (as heat) are primarily those needed to drive the high-temperature reactions. The ranges of efficiencies calculated (64% to 71%), although lower than those reported in Table 15 for the pure thermochemical cycles, are attractive. Unlike the pure thermochemical cycles, heat rejected by the exothermic reactions is at 298 K, so there are significant work requirements for the electrochemical steps. Therefore, Cycles F-8 and B-18 will require heat from the primary source to fulfill process work requirements, and the only energy output will be the hydrogen produced.

Table 18. MAXIMUM ATTAINABLE EFFICIENCIES FOR CYCLES F-8 AND B-18

Cycle	Heat Required as Heat	Heat Required for Work		Efficiency	
		CT	FT	CT	FT
	kcal			%	
F-8	73.1	33.6	25.1	64.0	69.6
B-18	73.7	30.8	22.7	65.4	70.9

Metal Oxide-Metal Sulfate Cycles

A general metal oxide-metal sulfate cycle is represented by Reactions 41 through 43 —

$$MO(s) + SO_2(g) + (x+1)H_2O(\ell) \rightarrow MSO_4 \cdot xH_2O(s) + H_2(g) \quad (41)$$

$$MSO_4 \cdot xH_2O(s) \rightarrow MSO_4(s) + xH_2O(g) \quad (42)$$

$$MSO_4(s) \rightarrow MO(s) + SO_2(g) + \tfrac{1}{2}O_2(g) \quad (43)$$

where M denotes a metal. Because thermodynamics data on hydrated sulfates are not very complete, in some cases we were forced to consider only unhydrated metal sulfates and to simply note the existence of stable hydrates. Also, thermodynamics data on metal oxysulfates and complex sulfates and oxides (possible products from the high-temperature sulfate decomposition, Reaction 43) are scarce; therefore, we relied primarily upon experimental data to determine the presence of other stable products from Reaction 43.

Six members of this class of cycles were derived and labeled as Z-32 through Z-37. Although the free-energy changes for the hydrogen-producing reactions in Cycles Z-32 through Z-37 are all negative, these cycles are considered hybrid (thermoelectrochemical) cycles. Note that it is sulfur that changes valence during Reaction 41; the valence of the other metal species (M) does not change. In effect, the hydrogen-producing step in these cycles (Reaction 41) can be written as the sum of Reactions 41a and 41b.

$$SO_2(g) + 2H_2O(\ell) \rightarrow H_2SO_4(\ell) + H_2(g) \qquad (41a)$$

$$H_2SO_4(\ell) + MO(s) \rightarrow MSO_4(s) + H_2O(\ell) \qquad (41b)$$

$$MO(s) + SO_2(g) + H_2O(\ell) \rightarrow MSO_4(s) + H_2(g) \qquad (41)$$

Reaction 41a has a positive free-energy change (+7.8 kcal/mole H_2) that must be supplied as work in the form of an electrical potential even though the sum of the free-energy changes for Reactions 41a and 41b is negative. Because the hydrogen-producing steps of Cycles Z-32 through Z-37 will be driven electrochemically in (presumably) an aqueous electrolyte, we also report solubility data for both reactant (MO) and product (MSO_4) species. An insoluble metal oxide may make cell design difficult, and a very soluble metal sulfate might be difficult to separate from a spent electrolyte. Ideally, the reacting metal oxide should be more soluble in a slightly acidic electrolyte (dissolved sulfur dioxide) than the produced metal sulfate.

Cycle Z-32, a calcium oxide-calcium sulfate cycle, is shown below as Reactions 44 through 46.

$$CaO(s) + SO_2(g) + 3H_2O(\ell) \rightarrow CaSO_4 \cdot 2H_2O(s) + H_2(g) \qquad (44)$$

$$CaSO_4 \cdot 2H_2O(s) \rightarrow CaSO_4(s) + 2H_2O(g) \qquad (45)$$

$$CaSO_4(s,\ell) \rightarrow CaO(s) + SO_2(g) + \tfrac{1}{2}O_2(g) \qquad (46)$$

The hydrogen-producing step, Reaction 44, has a free-energy change of −43.2 kcal at 298 K. $CaSO_4 \cdot 2H_2O$ will dehydrate (produce 1 atmosphere partial pressure of steam) at 360 K, where the free-energy change for the reaction equals zero. According to free-energy data, $CaSO_4$ should decompose (Reaction 46) at temperatures near or above its melting point of 1673 K. $CaSO_4 \cdot 2H_2O$ has a solubility in water of 2.41 g/ℓ at 298 K and 2.22 g/ℓ at 373 K. CaO has a

solubility of 1.31 g/ℓ at 283 K and only 0.70 g/ℓ at 353 K. CaO will exist in solution as $Ca(OH)_2$, which should react with sulfuric acid, in a step similar to Reaction 41b, to form $CaSO_4 \cdot 2H_2O$.

Cycle Z-33, a strontium oxide-strontium sulfate cycle, is shown below as Reactions 47 and 48.

$$SrO(s) + SO_2(g) + H_2O(\ell) \rightarrow SrSO_4(s) + H_2(g) \quad (47)$$

$$SrSO_4(s,\ell) \rightarrow SrO(s) + SO_2(g) + \tfrac{1}{2}O_2(g) \quad (48)$$

The hydrogen-producing step, Reaction 47, has a free-energy change of −53.0 kcal at 298 K. We found no evidence of stable hydrates of strontium sulfate. Free-energy data indicate that $SrSO_4$ will decompose (Reaction 48) at temperatures near or slightly above its melting point of 1873 K. $SrSO_4$ is only slightly soluble in water, 0.11 g/ℓ at 273 K and 0.14 g/ℓ at 303 K; SrO has a higher solubility of 6.9 g/ℓ at 293 K and 228.5 g/ℓ at 373 K. The relative solubilities of SrO and $SrSO_4$ make this system attractive because $SrSO_4$, formed from a concentrated solution of SrO (and sulfuric acid), should form an easily recoverable precipitate. This is the only oxide-sulfate pair examined where the sulfate is less soluble than the oxide.

Cycle Z-34, a cobalt oxide-cobalt sulfate cycle, is shown below as Reactions 49 and 50.

$$CoO(s) + SO_2(g) + H_2O(\ell) \rightarrow CoSO_4(s) + H_2(g) \quad (49)$$

$$CoSO_4(s) \rightarrow CoO(s) + SO_2(g) + \tfrac{1}{2}O_2(g) \quad (50)$$

The hydrogen-producing step, Reaction 49, has a free-energy change of −2.0 kcal at 298 K. Free-energy data predict that $CoSO_4$ will decompose (Reaction 50) at temperatures greater than or equal to 1300 K. Three stable hydrates of $CoSO_4$ (heptahydrate, hexahydrate, and monohydrate) are reported in the literature, but complete thermodynamics data are not available for these species. Reaction 49 will actually produce $CoSO_4 \cdot 7H_2O$ (analogous to Reaction 41 with M equal to Co and x equal to 7), which would have to be dehydrated in a separate reaction step (analogous to Reaction 42). $CoSO_4$ is very soluble in water, 362 g/ℓ at 293 K and 830 g/ℓ at 373 K; CoO is insoluble in water and soluble in acid. Another stable cobalt sulfate, $Co_2(SO_4)_3$, and corresponding hydrate, $Co_2(SO_4)_3 \cdot 18\ H_2O$, are reported in the literature, but no thermodynamics data are available.

Cycle Z-35, a magnesium oxide-magnesium sulfate cycle, is represented below by Reactions 51 and 52.

$$MgO(s) + SO_2(g) + H_2O(\ell) \rightarrow MgSO_4(s) + H_2(g) \quad (51)$$

$$MgSO_4(s,\ell) \rightarrow MgO(s) + SO_2(g) + \tfrac{1}{2}O_2(g) \quad (52)$$

The hydrogen-producing step, Reaction 51, has a free-energy change of −15.0 kcal at 298 K. Free-energy data predict that $MgSO_4$ will decompose (Reaction 52) at temperatures greater than or equal to its melting point of 1400 K. Two stable hydrates of $MgSO_4$ (heptahydrate and monohydrate) are reported in the literature, but complete thermodynamics data are not available for these species. Reaction 51 will actually produce $MgSO_4 \cdot 7H_2O$ (analogous to Reaction 41 with M equal to Mg and x equal to 7), which would have to be decomposed in a separate reaction step (analogous to Reaction 42). $MgSO_4$ is very soluble in water, 260 g/ℓ at 273 K and 738 g/ℓ at 373 K; MgO is only very slightly soluble, 0.09 g/ℓ at 303 K.

Cycle Z-36, a manganese oxide-manganese sulfate cycle, is represented below by Reactions 53 and 54.

$$MnO(s) + SO_2(g) + H_2O(\ell) \rightarrow MnSO_4(s) + H_2(g) \quad (53)$$

$$MnSO_4(s) \rightarrow MnO(s) + SO_2(g) + \tfrac{1}{2}O_2(g) \quad (54)$$

The hydrogen-producing step, Reaction 53, has a free-energy change of −13.7 kcal at 298 K. Free-energy data predict that $MnSO_4$ will decompose (Reaction 54) at temperatures greater than 1360 K. Many stable hydrates of $MnSO_4$ (between a heptahydrate and a monohydrate) are reported in the literature, but complete thermodynamics data are not available for these species. Reaction 53 will probably produce $MnSO_4 \cdot 7H_2O$, which would have to be decomposed in a separate reaction step. $MnSO_4$ is very soluble in water, 520 g/ℓ at 278 K and 700 g/ℓ at 343 K; MnO is insoluble in water but soluble in acid.

Two basic criteria were used to determine which of the six cycles described above are the most attractive candidates for further development. First, solubility characteristics are important for the following reasons: a) The metal oxide that reacts in the hydrogen-producing step should be soluble in order to facilitate the reaction, and b) the sulfate that is the product of that reaction should be relatively insoluble in order to facilitate

the separation of the sulfate from the electrolyte. Ideally, the oxide should be more soluble in the electrolyte than the sulfate. Also, the metal sulfate (or a hydrated sulfate) must be completely anhydrous before it is decomposed back to the oxide at high temperature. Because the amount of low-temperature heat required to dehydrate a metal sulfate is directly proportional to the degree of hydration, the sulfate that forms the lowest order hydrate is the most attractive. Ideally, we desire a sulfate that does not form a hydrate at all.

Based on these criteria, the strontium oxide-strontium sulfate cycle (Z-33) appears to be the most attractive. Strontium sulfate is over one order of magnitude less soluble (in water) than strontium oxide. In addition, strontium sulfate does not hydrate. The calcium oxide-calcium sulfate cycle (Z-32) is the next most attractive candidate for further development. Although $CaSO_4 \cdot 2H_2O$ is slightly more soluble than CaO, its solubility is still two orders of magnitude lower than any other sulfate (except $SrSO_4$). The thermal burden associated with removing two moles of water per mole of $CaSO_4$ should not be excessive. To date, our search for metal oxide-metal sulfate cycles has been limited to those cycles involving compounds whose thermodynamics properties are readily available. Researchers at LASL, for example, are developing an analogous bismuth oxide-bismuth sulfate cycle, but have been forced to measure thermodynamic properties for some of the chemical species involved.

Maximum attainable efficiencies were calculated for Cycles Z-32 and Z-33 using two assumed operating modes for their hydrogen-producing steps. In the first mode (a), we assumed electrochemical production of hydrogen at 298 K from $SO_2(g)$, $H_2O(\ell)$, and either CaO(s) or SrO(s). In the second mode (b), we assumed thermochemical production of hydrogen at elevated temperatures (corresponding to the temperature at which $\Delta G_{rx} = 0$) from $SO_2(g)$, $H_2O(g)$, and either CaO(s) or SrO(s). Thermodynamics data for the reaction steps in both cycles are presented in Table 19. Maximum attainable efficiencies for cycle operation in Modes a (298 K) and b (elevated temperatures) are presented in Table 20. In Table 19, the reactions corresponding to Modes a and b are labeled.

Table 19. THERMODYNAMICS DATA FOR CYCLES Z-32 AND Z-33

Cycle	Mode	Reaction	Temp, K	ΔG	ΔH	Work Required
				kcal		
Z-32	a	$CaO(s) + SO_2(g) + 3H_2O(\ell) \rightarrow CaSO_4 \cdot 2H_2O(s) + H_2(g)$	298	−43.15	−55.36	9.75
	b	$CaO(s) + SO_2(g) + H_2O(g) \rightarrow CaSO_4(s) + H_2(g)$	1150	0.00	−55.27	2.12
	a	$CaSO_4 \cdot 2H_2O(s) \rightarrow CaSO_4(s) + 2H_2O(g)$	375	−0.75	23.54	0.00
	a,b	$CaSO_4(\ell) \rightarrow CaO(s) + SO_2(g) + \frac{1}{2}O_2(g)$	1880	0.00	94.62	0.76
Z-33	a	$SrO(s) + SO_2(g) + H_2O(\ell) \rightarrow SrSO_4(s) + H_2(g)$	298	−55.60	−64.54	9.75
	b	$SrO(s) + SO_2(g) + H_2O(g) \rightarrow SrSO_4(s) + H_2(g)$	1360	0.00	−69.23	2.12
	a,b	$SrSO_4(\ell) \rightarrow SrO(s) + SO_2(g) + \frac{1}{2}O_2(g)$	2038	0.00	109.90	0.76

Table 20. MAXIMUM ATTAINABLE EFFICIENCIES FOR CYCLES Z-32 AND Z-33

Cycle	Mode	Heat Required as Heat	Work Required	Work Available		Efficiency	
				CT	FT	CT	FT
		kcal				%	
Z-32	a	145.1	10.5	--	--	40.0	41.6
	b	117.4	2.9	16.0	21.8	69.4	74.3
Z-33	a	145.0	10.5	--	--	41.9	43.7
	b	132.6	2.9	19.8	27.5	66.5	72.3

The efficiencies of Cycles Z-32 and Z-33 are strong functions of the temperatures and operating modes assumed for their hydrogen-producing steps. The efficiencies calculated for Cycles Z-32 and Z-33 operated in Mode a (40.0% to 41.6% for Cycle Z-32, and 41.9% to 43.7% for Cycle Z-33) are lower than one might expect for two-step cycles with a high-temperature step in the 1880 to 2038 K (2924° to 3210°F) range. The substantial exothermic heats of reaction for the hydrogen-producing steps of Cycles Z-32 (−55.36 kcal) and Z-33 (−64.54 kcal) are too low in quality to be useful at 298 K (77°F). Operating these cycles in Mode b, the exothermic heat from their hydrogen-producing steps are available at 1150 K (1610°F for Cycle Z-32) and 1360 K (1990°F for Cycle Z-33) and constitute high-quality heat that can be used to drive a heat-to-work cycle. In fact, the amount of work generated is in excess of cycle needs in both cases, and the actual output of Cycles Z-32 and Z-33 is both hydrogen and small amounts of work.

The maximum obtainable efficiencies calculated for Cycles Z-32 and Z-33 (69.4% to 74.3% and 66.5% to 72.3%, respectively) operated in Mode b indicate that these cycles are only attractive as thermochemical, rather than hybrid thermoelectrochemical, cycles.

TASK 6. INTERFACING CHARACTERISTICS: SOLAR HIGH-TEMPERATURE HEAT SOURCES

In thermochemical water-splitting processes, generally, the higher the temperature at which the process operates (the reaction temperature of the endothermic steps), the fewer intermediate steps that are required in the sequence. A thermochemical water-splitting cycle can only recover, or merit, part of the available second-law efficiency. For two similar cycles with the same heat rejection temperature, T_L, that cycle operating at the higher heat acceptance temperature, T_H, will have the higher energy efficiency and, presumably, the better overall process efficiency, because the Carnot function $(T_H - T_L/T_H)$ increases as T_H increases.

In most research programs, the larger part of early thermochemical water-splitting development has been aimed at interfacing the endothermic reaction steps with the secondary helium-coolant streams of high-temperature nuclear fission reactors (HTR's). Currently, the upper temperature anticipated for such coolant streams is about 1150 K, limiting the energy efficiency of a process to a second-law efficiency (Carnot function) of less than 0.69. For nonisothermal process heat temperatures available from solar concentrators, which are in the range of 1500 to 2500 K, the second-law efficiency limitations range from 0.78 to 0.86.

There is also a fundamental difficulty in mating processes to a nuclear reactor energy source (HTR). The most efficient thermochemical processes take in heat isothermally for high-temperature endothermic reactions and reject heat at low temperatures. HTR's offer a high-temperature interfacing capability of severely limited capacity. The temperatures of the secondary heat-exchange loops (usually helium-filled) are high enough for many cycles, but the capacity for transfer of high-temperature isothermal heat is low because large amounts of heat are delivered only with the concomitant penalty of downward cascading temperatures. The supply of heat at several decreasing temperatures calls for either a cycle with several isothermal heat requirements, rather than one requirement at high temperature, or for "hybrid" cycles, where generated electricity drives an electrochemical step. Disregarding energy sources, such isothermal-requirement cycles are inherently more

efficient than cycles with multiple reaction sequences. However, where a nonisothermal heat source is specified, the most efficient load-line efficiency will likely be associated with a hybrid or multiple-step cycle.

Solar concentration sources also are capacity-limited, but they are expected to be capable, through engineering design, of yielding near-isothermal heat at higher temperatures than HTR's. The upper limit for certain types of solar concentrators appears to be 2000 K, and isothermal heat at temperatures as high as 1600 and 1800 K may be available during periods of insolation.

When compared with a nuclear heat source, there are inherent advantages in using solar concentrators. The applicability of solar process heat at higher temperatures will result in cycles that merit a higher second-law efficiency and perhaps a higher process efficiency. Also, the energy availability (the thermodynamic equivalent of work) is higher for an isothermal device than for a temperature-cascaded (nonisothermal) device operating with the same upper temperature. In principle, some chemical reactants could be circulated through the solar "furnace" without the need for an intermediate heat exchanger or coolant medium. When this is possible, it adds to the efficiency of converting heat into stored chemical energy.

Further research is required to determine whether the potential advantages of high-temperature solar primary heat sources can be realized when used to drive real chemical processes. Two basic options are available when interfacing solar heat with chemical processes: First, the chemical reactants may be used to absorb solar flux directly. Second, an intermediate coolant may be employed. For the second case, the use of a coolant that transfers only sensible heat to a chemical process (as does the helium coolant of an HTGR) should be avoided in order to retain the advantage of high availability for solar primary sources. Instead, heat recovered from the intermediate coolant should be either latent heat or the heat of a reversible chemical reaction (as in a chemical heat pipe), both of which can supply heat relatively isothermally.

Most of the high-temperature metal-metal oxide cycles (R-1, Q-2, B-17, F-8, and B-18) and metal oxide-metal sulfate cycles (Z-32 through Z-37), derived and analyzed in Section 5, have one common trait: Their high-temperature endothermic steps involve a solid reactant to which heat must be transferred. The movement of large amounts of solid materials to the focal point of a high-temperature solar collector may be difficult enough to rule out the use of these solid reactants as direct absorbants and require the use of an intermediate coolant. We investigated the use of an intermediate coolant that supplies chemical heat to a particular process (Cycle H-5, Reactions 55-58) and compared it with the use of a second intermediate coolant that supplies only sensible heat.

$$CuO(s) + 6H_2O(\ell) + SO_2(g) \rightarrow CuSO_4 \cdot 5H_2O(s) + H_2(g) \quad (55)$$

$$CuSO_4 \cdot 5H_2O(s) \rightarrow CuSO_4(s) + 5H_2O(g) \quad (56)$$

$$CuSO_4(s) \rightarrow CuO(s) + SO_3(g) \quad (57)$$

$$SO_3(g) \rightarrow SO_2(g) + \tfrac{1}{2}O_2(g) \quad (58)$$

The $SO_3(g)$ decomposition step (Reaction 58) used to close Cycle H-5, lends itself to reasonably direct interfacing between a solar collector and the high-temperature endothermic steps (Reactions 57 and 58). This concept is adapted from an idea suggested by Bowman and Cox at LASL. Chubb, Nemecek, and Simmons have provided conceptual designs of high-temperature solar energy systems using $SO_3(g)$ as the heat-absorbing working fluid.[25,26] It should be feasible to operate the $SO_3(g)$ decomposition step in a solar reactor at temperatures near the 1300 K temperature proposed for Reaction 58. The hot effluent from this step [$SO_2(g)$, $O_2(g)$, and traces of $SO_3(g)$] can provide the feedstocks required to close the cycle and sensible heat for use in the lower-temperature processes (Reaction 56). The bulk of the decomposed $SO_3(g)$ could be used cyclically as a heat source (sensible heat) for work generation and in the $CuSO_4(s)$ decomposition (heat of recombination). The hot $SO_2(g)/O_2(g)$ mixture would be directly contacted with $CuSO_4(s)$ feed for sulfate decomposition Reaction 57 where it should catalytically recombine, releasing the high-temperature heat required to drive Reaction 57. Chubb's work[25] indicates that the $SO_2(g)/O_2(g)$ mixture is stable enough to give up its sensible heat

over a temperature range of around 770 K (1420°F); thus, the use of the dissociated gas mixture for both high-quality sensible heat and for chemical reaction heat (23.42 kcal per mole of SO_3) is feasible. Figure 27 shows a schematic diagram of the system for transmitting heat to the high-temperature steps. In effect, solar heat absorbed by the endothermic decomposition of $SO_3(g)$ (Reaction 58) is supplied isothermally to a solid decomposition step (Reaction 57) as the heat of recombination of $SO_2(g)$ and $\frac{1}{2}O_2(g)$.

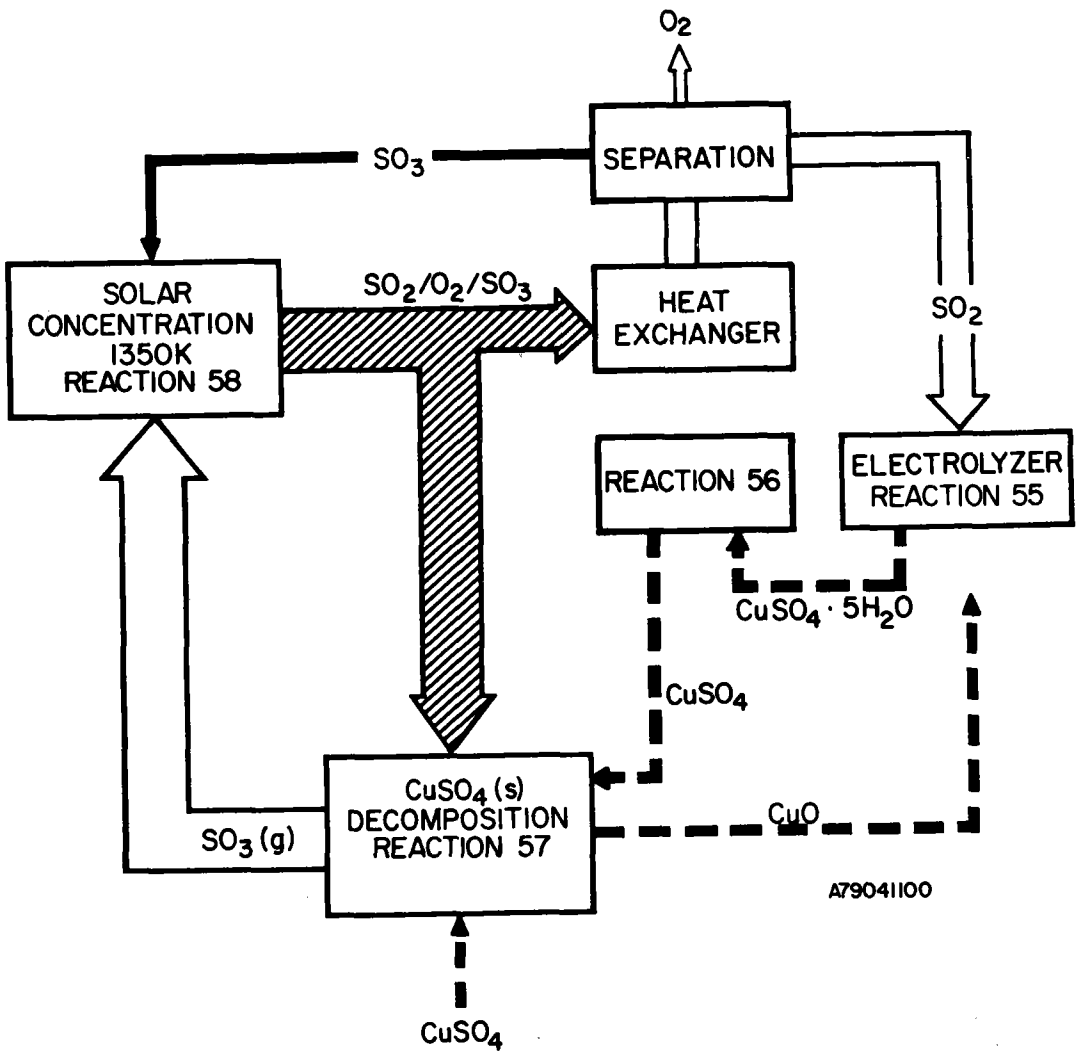

Figure 27. CONCEPTUAL SOLAR HEAT SUPPLY FOR CYCLE H-5

There are other possible choices for supplying the required high-temperature heat. Sanders Associates are currently testing a central receiver air heater that should reach temperatures in the heated fluid as high as 1366 K (2000°F).[27] Using air as a heat transfer medium should raise fewer materials problems than using $SO_2(g)/O_2(g)$ mixtures, but the absence of a chemical-energy heat-releasing step [$SO_2(g) + \frac{1}{2}O_2(g) \rightarrow SO_3(g)$] means the heat is "paid for" by constant lowering of the quality. The preferred version of the Chubb "Solchem" system has the enormous advantage of supplying the larger high-temperature endothermic heat requirement virtually at constant temperature (isothermal heat). The use of a central receiver "fired" air heater would entail much less "direct" heat transfer to the $CuSO_4(s)$ decomposition step and probably require larger heat transfer surfaces than the $SO_2(g)/O_2(g)$ mixture.

TASK 7. ANALYSIS OF SOLAR AND SOLAR HYBRID HEAT SOURCES

Analysis of Solar Heat Sources

In the August through November 1978 monthly reports, we reported capital cost and performance data for various types of solar collectors. Subsequently, we discovered and corrected errors in our analyses; the cost data presented in this report are the corrected figures.

Our principal source of information on low- to medium-temperature collectors was a recent IGT study[28] comparing costs of several types of collectors applicable to residential solar total energy systems. Data for collectors by different manufacturers are presented in Tables 21 and 22. The flat plate (FP), evacuated tube (ET), and compound parabolic collectors (CPC) are capable of using total inflation; the tracking (and focusing) collectors make use of only the direct component of the insolation.

Capital costs for low- to medium-temperature collectors, C_H [in units of $\$/(10^6$ Btu/day)], were calculated from given costs, C_A (in units of $\$/ft^2$), according to Equation 59, where η is the collector efficiency (dimensionless) and I is either total or direct solar insolation [in Btu/(ft^2·day)] depending upon the type of collector.

$$C_H = \frac{C_A}{\eta I} \tag{59}$$

Collector efficiency is calculated from Equation 60, where η_{opt} (the optical efficiency), A, and B are experimentally determined properties of a given collector.

$$\eta = \eta_{opt} - \frac{A(T_c - T_a) + B(T_c^4 - T_a^4)}{I} \tag{60}$$

The A term represents heat losses due to convection and conduction, the B term represents losses due to reradiation, and T_c and T_a are the collector and ambient temperatures, respectively.

To compare collectors on an equivalent basis while still providing realistic results, we used a single value each for total and direct insolation which corresponds roughly to the annual daily averages for Phoenix, Arizona. In our original calculations of C_H, solar insolation values were taken from a

Table 21. COSTS AND CAPACITIES OF SOLAR COLLECTORS

Collector	Insolation Used	Temperature Range, °F	C_A, Collector Cost, $/ft^2	Installed Cost, $/ft^2	Collector Capacity, ηI, Btu/(day-ft^2)*	Collector Cost, C_H, $/($10^6$ Btu/day) T_{min}	T_{max}
Flat Plate (FP1)	T	135-210	15	NA	5706.6-7.2 T_c	10,500	16,900
(FP2)	T	100-200	9	NA	6604.7-9.0 T_c	5,700	13,400
(FP3)	T	100-150	5	NA	9576.2-14.6 T_c	3,600	7,600
Evacuated Tube (ET1)	T	150-330	20	31.15	2611.9-1.9 T_c	13,700	17,800
(ET2)	T	135-210	12	23.15	3787.0-4.2 T_c	9,300	12,300
Compound Parabolic Coll.							
(CPC1) [1.5X]	T	200-400	25	36.25	2209.3-1.6 T_c	21,200	28,800
(CPC1A) [1.5X]	T	200-400	32.5	43.75	2464.9-1.4 T_c	21,400	26,500
(CPC2) [5X]	T	300-500	25	39.35	1870.6-1.4 T_c	32,200	51,100
(CPC2A) [5X]	T	300-500	32.5	46.85	2072.9-1.0 T_c	24,900	29,400
One-Axis Tracking							
(T1)	D	200-350	20	31.45	2012.0-0.9 T_c	13,800	15,100
(T2)	D	200-900	NA	NA	1735.4-0.7 T_c	11,900	19,800
(T3)	D	200-300	19	NA	2801.7-2.3 T_c	14,600	17,700
Parabolic Trough (PT1)	D	150-600	25	37.25	2146.3-0.8 T_c-5.5 X 10^{-11} T_c^4	15,100	20,200
(PT2)	D	140-350	14	26.25	1982.7-1.0 T_c-6 X 10^{-10} T_c^4	10,500	14,800
(PT3)	D	150-250	8	20.00	5144.4-6.6 T_c	7,100	17,200
Two-Axis Tracking							
(TT1)	D	500-1200	40	NA	1877.9-0.09 T_c-8.8 X 10^{-12} T_c^4	22,400	24,100
(TT2)	D	500-1300	22	NA	1958.3-0.16 T_c	12,200	13,100

* $\eta I = \eta_{opt} I - A(T_c - T_a) - B(T_c^4 - T_a^4)$

$\eta_{opt} = 0.9\ \eta_{opt,clean}$

T_a = 25°C = 298 K = 77°F = 537°R

Table 22. CURRENT AND FUTURE TECHNOLOGY COSTS OF COLLECTORS[28]

Collector	Collector Cost		Installed Cost		Operating and Maintenance Cost	
	CT	FT	CT	FT	CT	FT
	$/ft^2		$/ft^2		$/ft^2-yr	
Flat Plate (FP1)	15					
(FP2)	9					
(FP3)	5					
Evacuated Tube						
(ET1)	20	15	31.15	20.58	1.00	0.10
(ET2)	12	9	23.15	14.58	1.00	0.10
Compound Parabolic						
(CPC1)	25.0	14.0	36.25	19.63	1.25	0.16
(CPC1A)	32.5	15.4	43.75	21.03	1.25	0.16
(CPC2)	25.0	14.0	39.35	21.18	1.50	0.20
(CPC2A)	32.5	15.4	46.85	22.58	1.50	0.20
One Axis Tracking						
(T1)	20	14	31.45	19.73	0.75	0.15
(T2)	NA					
(T3)	19					
Parabolic Trough						
(PT1)	25	14	37.25	22.13	1.00	0.20
(PT2)	14	12	26.25	20.13	1.00	0.20
(PT3)	8	7	20.00	15.13	1.00	0.20
Two Axis Tracking						
(TT1)	40					
(TT2)	22					

bar graph presented by Denton.[29] The units on Denton's graph are shown as KWH/M^2 (kWhr/m^2), which we divided by an assumed 10 hours of useful sunlight per day to yield the required units [kWhr/(m^2·day), or the equivalent, Btu/(ft^2·day)]. The value of I (direct insolation) used in Equations 59 and 60 was 0.8 kWhr/(m^2·day) in our original calculations. The values in Denton's graph are, in fact, daily averages and already have the desired units of kWhr/(m^2·day). They should have been used directly (with appropriate units conversions) without division by assumed length of a sunlit day; therefore, our original calculations resulted in values of capital cost, C_H, that are roughly an order of magnitude too high. The values of total and direct solar insolation used in our revised calculations are —

$$I_T = 8.0 \text{ kWhr/(m}^2\text{·day)} = 2540 \text{ Btu/(ft}^2\text{·day)}$$

$$I_D = 5.9 \text{ kWhr/(m}^2\text{·day)} = 1870 \text{ Btu/(ft}^2\text{·day)}$$

We also revised the values of η_{opt} downward by 10% to account for collector deterioration due to weathering.

The collector capacity, ηI, is tabulated in Table 21 as a function of collector temperature, T_c (in degrees Rankine). The costs of uninstalled collectors with a daily capacity of 10^6 Btu are shown for the minimum and maximum operating temperatures.

Collector costs, C_H, vary widely, not only among different types but also among collectors of a single design. This is largely because this technology is still in the early stages of development. In Table 22, estimates of future technology costs are compared with current technology; both the absolute costs and the range of costs are expected to be significantly reduced in the future.

Costs of low- and medium-temperature collectors were plotted versus design (operating) temperatures in Figure 28. The capital cost of nontracking collectors (flat plate, evacuated tube, and compound parabolic collectors) escalates rapidly as the operating temperature of the collector increases. One-axis tracking collectors (SLATS, parabolic troughs) are somewhat more cost-effective when higher temperatures [up to about 900 K (1160°F)] are desired.

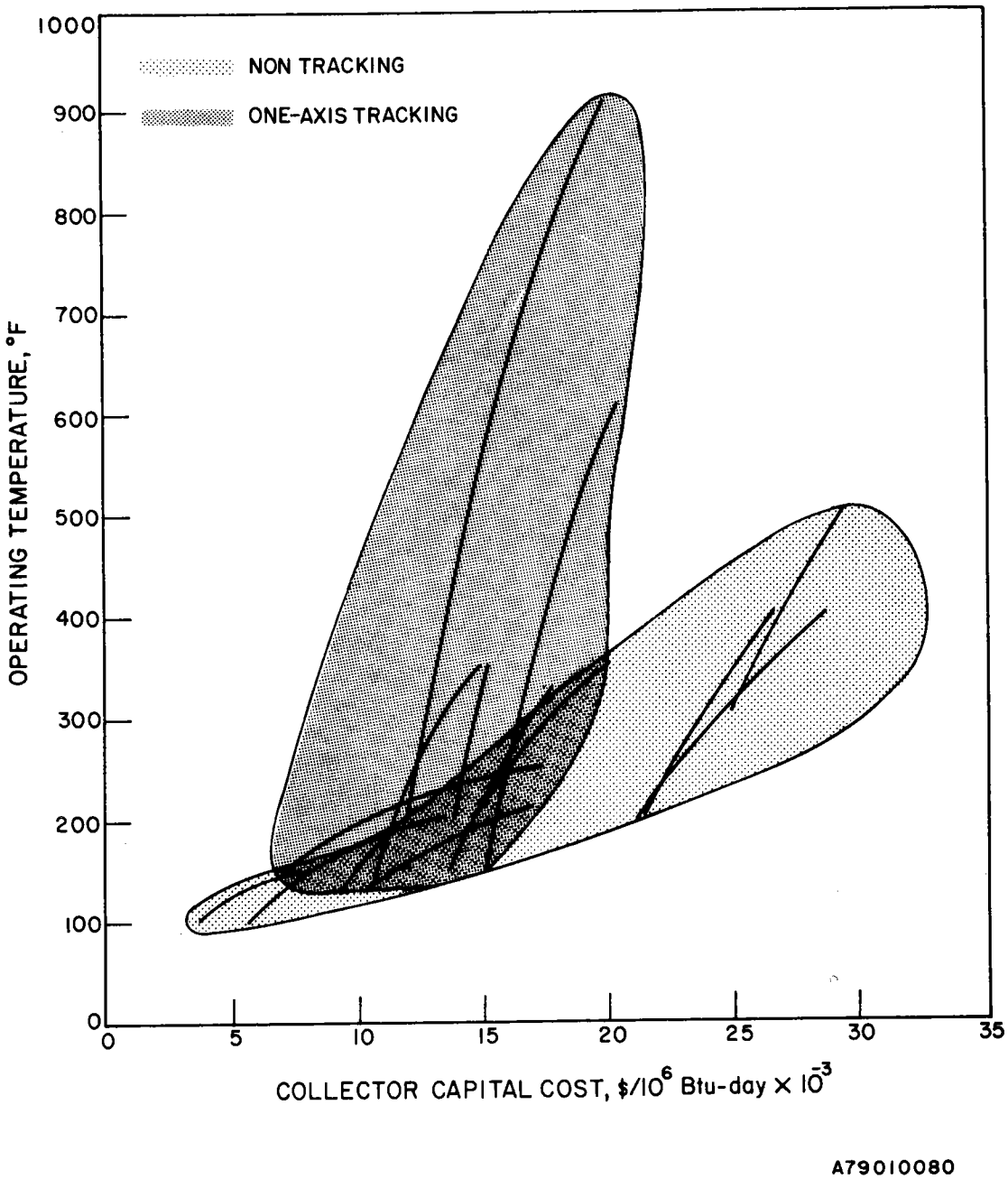

Figure 28. COSTS OF COLLECTORS VERSUS DESIGN TEMPERATURE

Capital costs [in $/($10^6$ Btu/day)] of high-temperature [> 700 K (800°F)] solar collectors are presented in Table 23. All of these collectors are of the heliostat/central receiver design, except for the 100 kW_e ANSALDO/Messerschmidt, which is a parabolic dish. These costs are for collector and receiver hardware only. The amounts presented in Table 24 also include the cost of land, structures and facilities, miscellaneous plant equipment, contingency and spare parts, and indirect costs, but not interest during construction. Only the Sandia Solar Thermal Test Facility (STTF) is an existing operational facility; the ANSALDO/Messerschmidt collectors are "ready for order,"[30] but the rest represent paper studies. Therefore, most of these cost figures are rather speculative. In many cases, however, the price is expected to be less when in mass production.[30] Operating and maintenance costs for these collectors are not available, but are expected to be no more than a "normal" fraction of initial capital costs.

Except for the cost of the Sandia/Barstow central receiver, which remains unchanged, the costs presented in Tables 23 and 24 are revised values. The same error in the use of insolation figures that was made in calculating the costs of lower-temperature collectors was also made in calculating costs of the ANSALDO/Messerschmidt and the DOE Contractors collectors. In the cases of Black and Veatch, Boeing, and Sandia STTF central receivers, the rated, or peak, capacity had been used to determine costs; the average daily capacity is actually 1/3 to 1/5 of the rated capacity. Thus, using the 1/3 factor, the revised costs for these receivers are three times the original figures.

Costs are expected to drop, but when or whether they will become competitive with the cost of nuclear heat cannot be predicted. Light-water reactor power plants of 1200 MW_e capacity (or about 4000 MW_{th}) currently cost about \$1270 kW_e.[35] Assuming that turbines and electric generating equipment account for 10% of this figure, the capital cost of nuclear heat plants is then roughly \$4200/(10^6 Btu/day). Though this is about one-third of the cost of the least expensive solar plant, the nuclear plant has a rated capacity of more than one order-of-magnitude greater than that of the solar plants; some of the difference in costs might therefore be explained in terms of economics-of-scale.

Table 23. CAPITAL COSTS OF HIGH-TEMPERATURE SOLAR COLLECTORS

Company	Plant Size	Design Temp, K	Cost, $/($10^6$ Btu/day)	Reference
ANSALDO/ Messerschmidt	5 MW_{th}/ 1 MW_e	870	27,300 [a,b]	30
ANSALDO/ Messerschmidt	100 kW_e	820	108,500 [a,b]	30
Black and Veatch	166 MW_{th}/ 60 MW_e	1340	8,350-12,410 [b]	31
Boeing	100 MW_e	1090	11,020 [c]	32
DOE Contractors	--	750	30,900-34,890 [a]	30
Sandia/ Barstow	100 MW_e	810	14,910-10,230 [d]	33
Sandia STTF	5 MW_{th}	790	153,760 [d,e]	34

[a] Assumes collector efficiency of 70% and direct insolation of 5.9 kW/m^2-day.
[b] 1976 dollars.
[c] 1975 dollars.
[d] 1977 dollars.
[e] Complete cost of operational facility.

Table 24. INSTALLED COSTS OF HIGH-TEMPERATURE SOLAR PLANTS

Company	Plant Size, MW_{th}	Cost, $/($10^6$ Btu/day)	Reference
Black and Veatch	166	10,380-15,050*	31
Boeing	269	13,830**	32
Sandia/ Barstow	~290	20,180-12,570*	33
Sandia STTF	5	153,760**	34

* 1976 dollars.
** 1975 dollars.

Analysis of Nuclear Heat Sources

We investigated both conventional, low-temperature nuclear (fission) heat sources, based on existing BWR-PWR technology, and high-temperature nuclear sources, based on high-temperature gas-cooled reactor (HTGR) technology. In order to compare these sources with the solar systems presented earlier, capital cost per 10^6 Btu per day data were compiled for the various systems.

Capital costs (given in 1975 dollars) for nuclear facilities are summarized in Table 25. The capital costs reported for the low-temperature nuclear designs are from a summary of actual BWR-PWR costs compiled by The Mitre Corporation.[36] The referenced cost is an average value for all plants constructed in 1975 and is in units of $/kWe. The portion of that cost attributable to the electric generation system and overall plant efficiency were not presented. Therefore, we simply assumed an average 33% heat-to-electricity efficiency and no cost for power generation equipment. Both assumptions are conservative and yielded costs for heat (reported in Table 25 as $/kW$_{th}$) that are undoubtedly higher than actual. The capital costs reported for the high-temperature HTGR are from an Oak Ridge National Laboratory (ORNL) assessment of nuclear process heat and do not include electric generation facilities.[37]

Table 25. INSTALLED CAPITAL COSTS FOR NUCLEAR HEAT SOURCES

Source Type	Maximum Process Temp, K	Coolant	Installed Capital Cost	
			1975 $/kW$_{th}$	1975 $/($10^6$ Btu/day)
PWR	625	H_2O	110	1320
BWR	650	H_2O		
HTGR	1150	He	270	3260

The last column in Table 25 presents capital costs per million Btu per day thermal output, the same units as those presented earlier for solar primary heat sources in Tables 21, 23, and 24. The solar costs presented thus far are not directly comparable with the nuclear costs for the following reasons:

a. The nuclear capital costs are for completely installed facilities and include 8%/year interest during construction (for 8 years). The solar costs presented in Tables 21 and 23 are for hardware only (uninstalled), while the figures in Table 24 include installation but not interest during construction.

b. The nuclear capital costs are for 3000 MW_{th} (HTGR) and 300 to 3000 MW_{th} (average PWR-BWR) facilities. The solar facilities are all below 300 MW_{th}.

c. Nuclear costs are all in 1975 dollars. Solar costs are in 1975 dollars in Table 21, but in 1975 to 1977 dollars in Tables 23 and 24.

In order to make nuclear and solar costs more directly comparable, we adjusted all of the solar costs to 1975 dollars. Uninstalled costs for the low-temperature solar collectors (Table 21) were increased by 50% to account for installation charges. Installed costs for both high- and low-temperature solar collectors were adjusted to account for 8%/year interest during construction (4 years as opposed to 8 years for nuclear plants). No attempt was made to scale solar systems to 3000 MW_{th}. Because the costs of solar systems are likely to be directly proportional to capacity (except for very small capacity systems),[38] we chose the largest capacity solar systems and did not scale their capital costs per million Btu per day figures. Comparable costs for high- and low-temperature nuclear and solar primary sources are summarized in Table 26. It is evident that the capital investment required for solar process heat is much higher than that required for nuclear heat. The cost quoted for low-temperature solar source ($\$26{,}200/10^6$ Btu/day) appears to be out of line. Our original data source presented costs for residential scale solar systems, which are about 4 to 5 orders-of-magnitude smaller than the low-temperature nuclear sources. We suspect that economics-of-scale could be realized for these solar systems, and that the actual cost would be lower than that quoted for the high-temperature solar sources.

Table 26. COMPARISON OF SOLAR AND NUCLEAR CAPITAL COSTS

Heat Quality	Capital Cost, $/($10^6$ Btu/day) Solar	Nuclear	Solar/Nuclear Cost Ratio
Low-Temperature (< 650 K)	26,200	1320	19.8
High-Temperature (> 650 K)	16,100	3260	4.9

Cycle Mating and Hybrid Sources

The large capital cost advantage of nuclear primary heat sources (compared with solar sources) simplifies the choice of a proper heat source for both high- and low-temperature cycle demands. Nuclear heat is preferred for all cycles providing that the quality of heat is adequate. Two types of cycle heat demands must, however, be met by solar heat. First, demands for heat above 1150 K, which is the upper limit for HTGR's, will require solar heat (or possibly nuclear fusion if it is successfully developed). All of the high-temperature metal-metal oxide and metal oxide-metal sulfate cycles derived and analyzed in Task 5 fall into this category. Second, the primary coolant must be cooled to 700 K before it is reinjected into the core, and coolant temperature cascades downward as sensible heat is extracted. Therefore, cycles that require large amounts of isothermal heat (particularly at high temperatures) may not mate with nuclear sources. The most plausible hybrid source would be solar for high-temperature heat, and nuclear for low-temperature heat (> 1150 K). Cycles B-1 and H-5 are candidates for this type of hybrid source, as reported in Task 1.

TASK 8. LABORATORY ASSESSMENT (Workability) OF CYCLE WITH HIGH-TEMPERATURE STEP

The strontium oxide-strontium sulfate cycle, Z-33 (Reactions 61 through 63), is an attractive high-temperature solar cycle (Task 5):

$$SrO(s) + SO_2(g) + H_2O(\ell) \rightarrow SrSO_4(s) + H_2(g) \quad (61)$$

$$SrSO_4(s) \rightarrow SrO(s) + SO_3(g) \quad (62)$$

$$SO_3(g) \rightarrow SO_2(g) + \tfrac{1}{2}O_2(g) \quad (63)$$

The temperature predicted by thermodynamics data for the decomposition of strontium sulfate (> 2000 K, 3140°F) is higher than the temperature we can reach with our laboratory furnaces, 1775 K (2735°F). Because we could not test the workability of the strontium sulfate decomposition directly, we measured the rate of decomposition at temperatures up to 1775 K and extrapolated that data to indirectly determine reaction workability. Normally, we conduct rate studies to provide the engineering data necessary to estimate reactor volume requirements, but, in this case, it was necessary to measure the rate to determine workability.

Thermodynamics of the Strontium Sulfate Decomposition

Thermodynamics data are available only for solid $SrSO_4$, which melts at 1873 K (2912°F). By extrapolating to higher temperatures, we find that the Gibb's free energy of Reaction 62 is zero at 2550 K (4130°F). Reaction 63 has a negative free energy above 1060 K (1445°F), so the net reaction, 64, has a free energy change of zero at 2020 K (3175°F), well above the melting point of $SrSO_4$. Based on known thermodynamic properties of other alkaline earth sulfates, we estimated the heat capacity and enthalpy of fusion of liquid $SrSO_4$ which enabled us to calculate free energy of formation data for liquid $SrSO_4$. The free-energy change for Reaction 65 is zero at 2038 K (3209°F).

$$SrSO_4(s) \rightarrow SrO(s) + SO_2(g) + \tfrac{1}{2}O_2(g) \quad (64)$$

$$SrSO_4(\ell) \rightarrow SrO(s) + SO_2(g) + \tfrac{1}{2}O_2(g) \quad (65)$$

Because the maximum temperature attainable in our furnace is 1775 K (2735°F) we were restricted to studying the workability and rate of Reaction 62 below that temperature. We assume that if solid $SrSO_4$ decomposes, then liquid $SrSO_4$ would also. However, the rate of decomposition of a liquid is likely to differ substantially and unpredictably from that of a solid, not only because the rate is so dependent upon reactant morphology but because different mechanisms control the reaction rate, and these mechanisms are quite sensitive to temperature.

Experimental Apparatus and Procedure

The most commonly used method of measuring the rate of decomposition of a solid is by thermogravimetric analysis, where the weight of a sample is monitored as it decomposes. Because the equipment needed for this type of analysis is specialized (and expensive) and generally not suited for operating under the conditions in which we are interested — very high temperature and corrosive product gases — we monitored, instead, the rate of production of gaseous sulfur oxides produced by decomposition. We used two techniques to measure the amount of sulfur oxides (SO_x) produced, both of which involved scrubbing the product and carrier gases with a sodium hydroxide solution. In one method, scrubbing solutions are switched at set time intervals as the reaction proceeds. The amounts of SO_2 and SO_3 (SO_x) in each sample are found by titration. This method involves tedious work and is as accurate as the titrations. To reduce the amount of labor involved and perhaps increase the accuracy of our results, we investigated a second method in which the pH of a single scrubbing solution is continuously and automatically measured and recorded over the course of the reaction. A discussion of this method is contained in the following two paragraphs; however, the method was not completely successful and was not used to develop data.

To correlate a pH with total SO_x in solution, it is necessary to know the ratio of SO_3 to SO_2 in the product gas at each point in time. Although the amount of SO_3 present at equilibrium at the temperature of interest (1675 to 1775 K, [2550° to 2735°F]) is virtually nothing (Figure 29), it is unlikely that this equilibrium can be maintained as the reaction products are cooled and dissolved. The reaction products must be flushed from the reactor quickly with minimal backmixing if the measured rate is to accurately represent

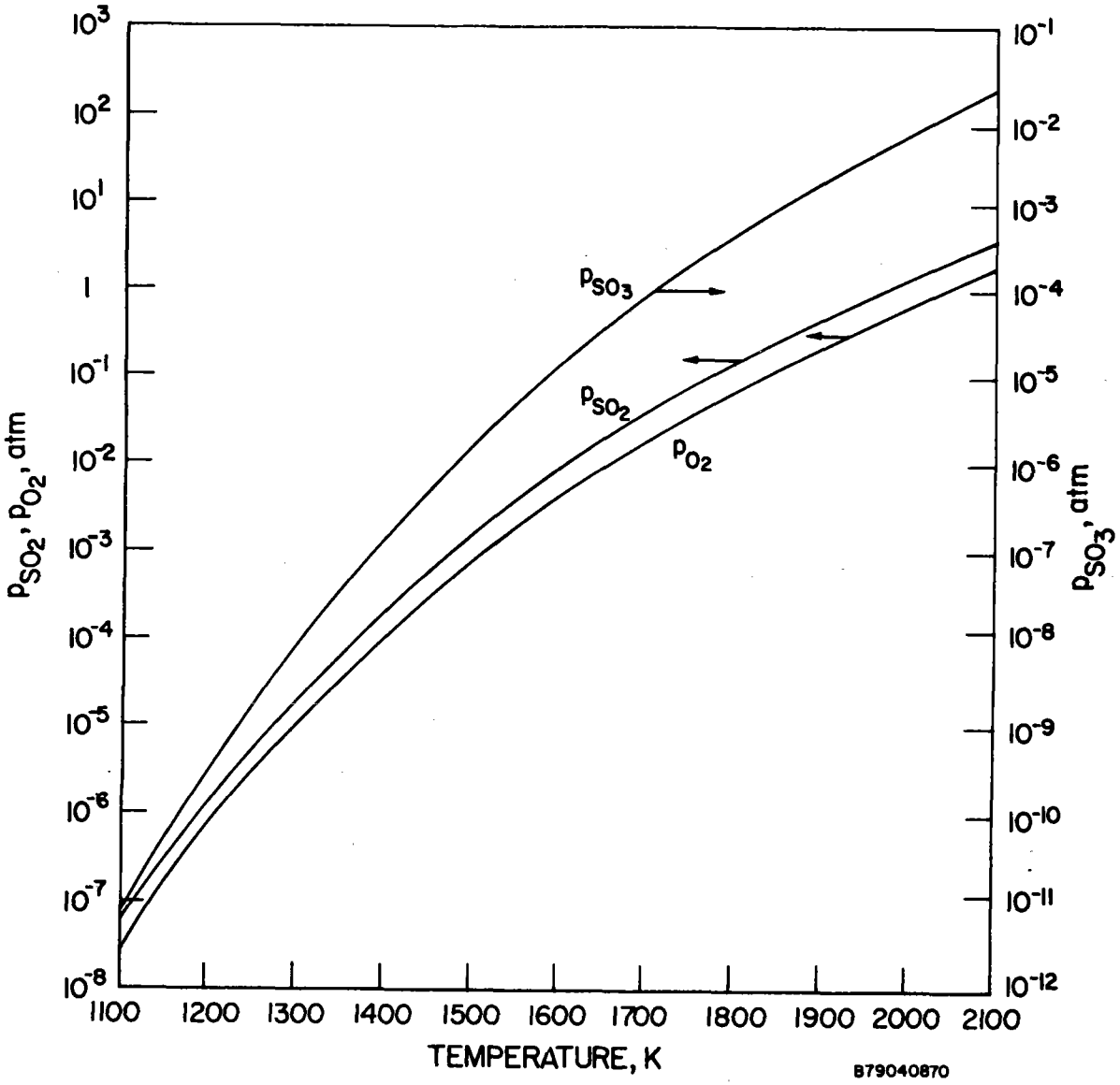

Figure 29. EQUILIBRIUM PARTIAL PRESSURES OF SO_3, SO_2, AND O_2 OVER $SrSO_4$(s)

the actual rate of SO_x production. At the lower temperatures outside the reactor, SO_3 is the thermodynamically favored oxide, so conversion of SO_3 to SO_2 will not take place once the products have left the reactor. In contrast, because SO_3 is favored at low temperatures, it should be possible to completely reoxidize SO_2 to SO_3 as it leaves the reactor by using a suitable catalyst.

In order to test conversions of SO_2 to SO_3, we passed mixtures of SO_2 (2 to 6 mole percent), argon, and oxygen through a catalyst bed, consisting of a tube 0.5 cm in diameter and 5 cm in length filled with platinum gauze. Gas flow rates between 50 and 150 cm^3/min (STP) and catalyst temperatures between 625 and 725 K (665° and 845°F) were used. The highest conversion of SO_2 to SO_3 that we obtained was 65%. A second catalyst configuration, consisting of a tube 0.3 cm in diameter and 30 cm in length packed with platinum-on-alundum (nonporous) catalyst and plugged at both ends with the platinum gauze used earlier, was tested. However, conversions no higher than 85% were obtained. At this time, we decided to abandon this approach and return to the method of using timed scrubbing solutions.

$SrSO_4$ decomposition reactions were carried out in a Lindberg box furnace with a maximum temperature capability of 1775 K (2735°F). The reaction vessel was a 9/16-in. ID tube of Coors AD-998 alumina placed inside a 1-3/4-in. ID tube of the same material. Figure 30 is a schematic diagram of the experimental apparatus. Argon carrier gas (preheated as it flowed through the annular space between the tubes) was used to sweep the SO_x produced out of the reactor. A solid ½-in. diameter rod of Coors AD-99 alumina filled most of the space inside the reactor tube downstream of the reactant bed to minimize residence time of the product gases. An aluminum collar with silicone rubber O-rings sealed the end of the larger tube, and a stainless steel reducer with O-ring seals connected the reactor to a three-way stopcock that permitted switching between two gas scrubber heads.

The furnace, with the closed-end tube in place, was preheated to 975 K (1295°F) to reduce heating time for the reactor. The reactor was purged with argon before it was placed into the furnace. Argon flow was stopped during the time the reactor was heated to reaction temperature (about 2½ hours) so that the reaction would proceed no farther than equilibrium, a fairly low

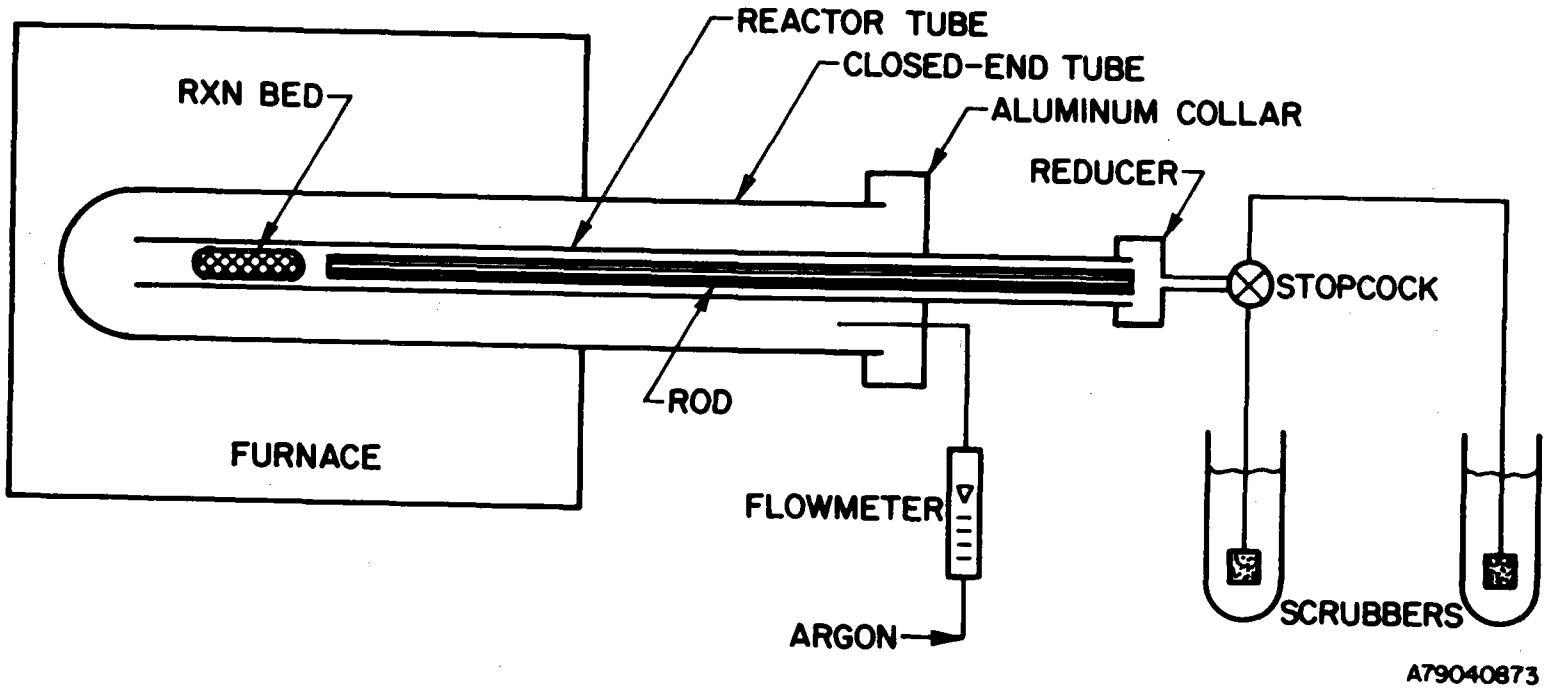

Figure 30. EXPERIMENTAL APPARATUS FOR THE $SrSO_4$ DECOMPOSITION

conversion even at 1773 K. When the system reached the desired temperature, the argon flow was reestablished (at about 50 cm^3/min) to "start" the reaction. During the reaction, 50 mℓ of 0.1 N NaOH solution was used to scrub SO_x from the product gas for a set period of time. At the end of that time period, the gas flow was switched to a new scrubbing solution.

Five experiments were completed, two using the pH measurement method and three using the switched scrubber method. Table 27 summarizes the conditions in each experiment.

Table 27. REACTION CONDITIONS: $SrSO_4$ DECOMPOSITION

Experiment Number	Temp, K	Weight of Starting Material, g	$SrSO_4$ in Starting Material, mmol	Length of Run, min	Final Conversion, %
1	1673	8.80	45.37	5520	85.1
2	1773	2.09	10.78	260	75.5
3	1773	5.05	26.04	260	45.1
4	1748	5.06	26.09	300	26.2
5	1723	3.20	16.50	600	53.0

In the first experiment, at 1673 K (2550°F), 8.8 grams of starting material filled the reactor tube between plugs of refractory wool. The wool plugs fused to the reaction product to form a solid mass that interfered with the analysis of the product. In the second reaction, at 1773 K (2735°F), we attempted to form the reactant into a hard pellet by compressing 2.1 grams of powder in a ½-in. diameter die under 8000 psig. The pellet broke apart before it could be inserted into the reactor, and only the fragments were used. The use of the pellet fragments eliminated the need for wool plugs. However, after four hours at 1773 K, most of the product was fused to the wall of the reactor. In the last three experiments, the reactant was simply spread in the tube, filling about half its diameter. At 1773 K, the product was again fused, although it was recovered for analysis. At 1748 K, the product was a vitrified mass that did not adhere to the reactor tube. After the last experiment, at 1723 K, it was again difficult to remove the product.

The product that adhered to the tube walls was extremely difficult to remove, possibly because the strontium reacted with the alumina. X-ray diffraction analysis of the product showed traces of $Sr_3Al_2O_6$; the only source of aluminum in the reactor was the aluminum oxide tube itself. (Used reactor tubes were cleaned in hot aqua regia.)

Results and Conclusions

In experiments 1 and 2, the rate was measured by monitoring the pH of the scrubbing solution. These data were rendered unusable by our inability to determine the relative proportions of SO_2 and SO_3 in the gaseous product as a function of time. In experiments 3, 4, and 5, the product gas was scrubbed with 50 mℓ of 0.1 mole sodium hydroxide solution for time increments of 20, 30, and 60 minutes, respectively. Each timed sample was analyzed to determine the amount of SO_2 and SO_3 collected. Total SO_x (SO_2 plus SO_3) is plotted versus reaction time in Figures 31 through 33. A straight line fits each of these plots very well. The reaction rate, which is proportional to the slope of each line, is therefore constant at all three temperatures. Dividing each slope by the amount of $SrSO_4$ initially charged yields the reaction rate in units of (moles $SrSO_4$ decomposed)$(min)^{-1}$(moles $SrSO_4$ charged)$^{-1}$.

We postulated an Arrhenius-type dependence of reaction rate on temperature:

$$r = k_o \exp(-E/RT) \qquad (66)$$

where k_o is the frequency factor having the same units as the reaction rate, r; E is the activation energy; and R is the gas constant. A plot of ℓn r versus 1/T should be linear with slope -E/R and intercept k_o. Figure 34 is such a plot for our data and is relatively linear. Substituting the slope and intercept from Figure 34 into Equation 66 gives the rate expression for the decomposition of strontium sulfate —

$$r = 3.6 \times 10^6 \exp(-3.8 \times 10^4/T) \qquad (67)$$

The calculated activation energy is, therefore, 76 kcal/mol.

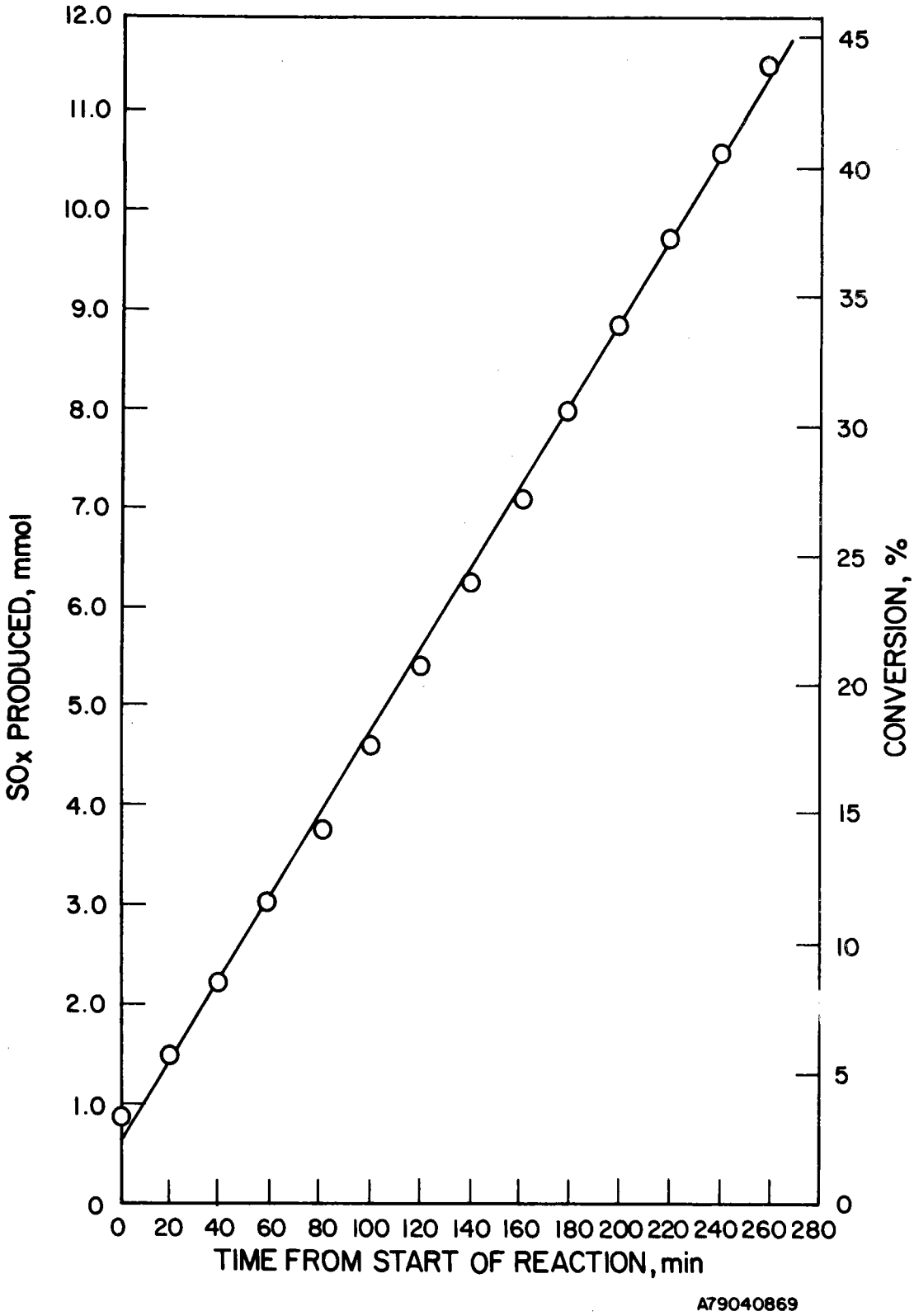

Figure 31. $SrSO_4$ DECOMPOSITION: SO_x PRODUCTION vs TIME (1773 K)

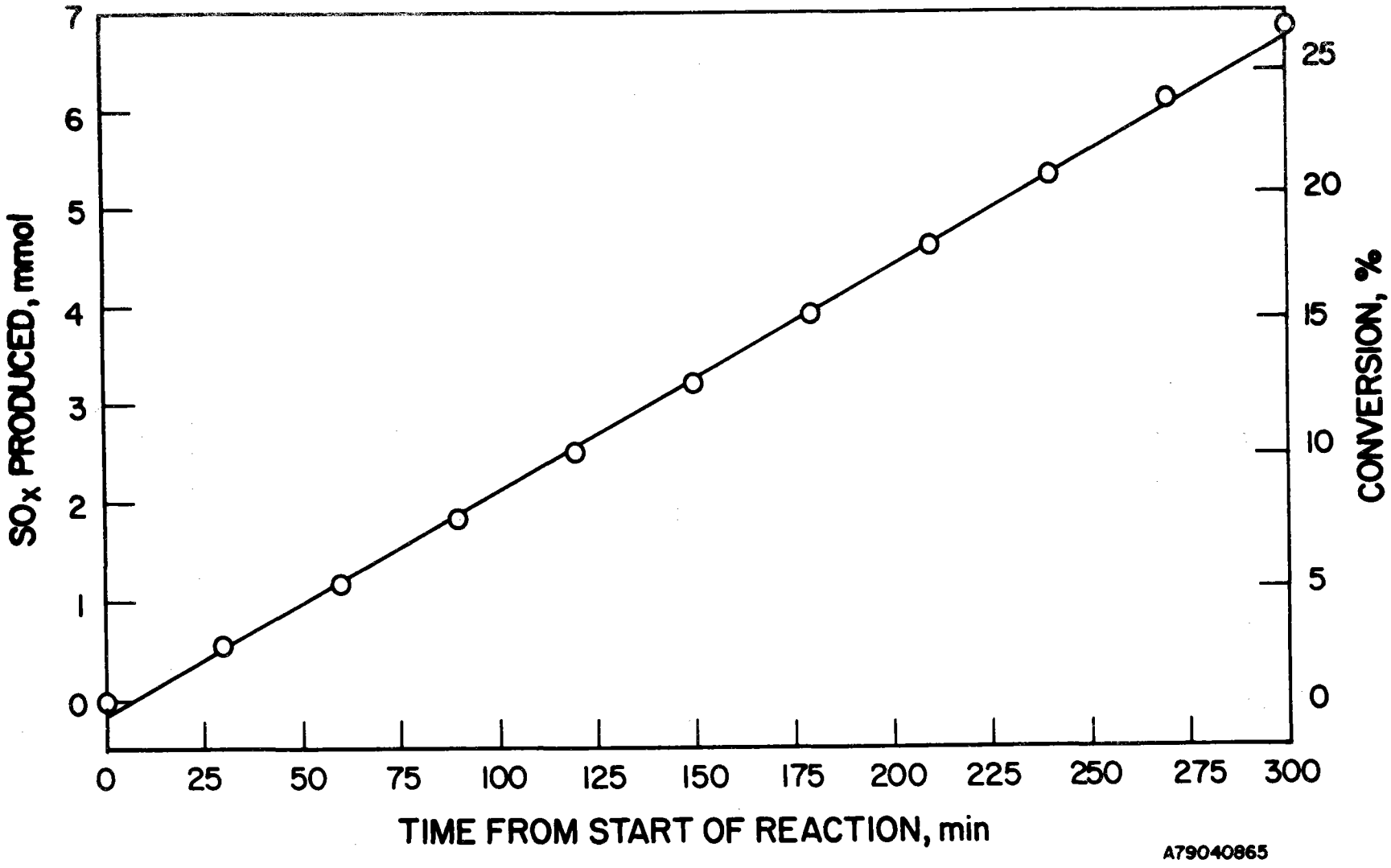

Figure 32. $SrSO_4$ DECOMPOSITION: SO_x PRODUCTION vs TIME (1748 K)

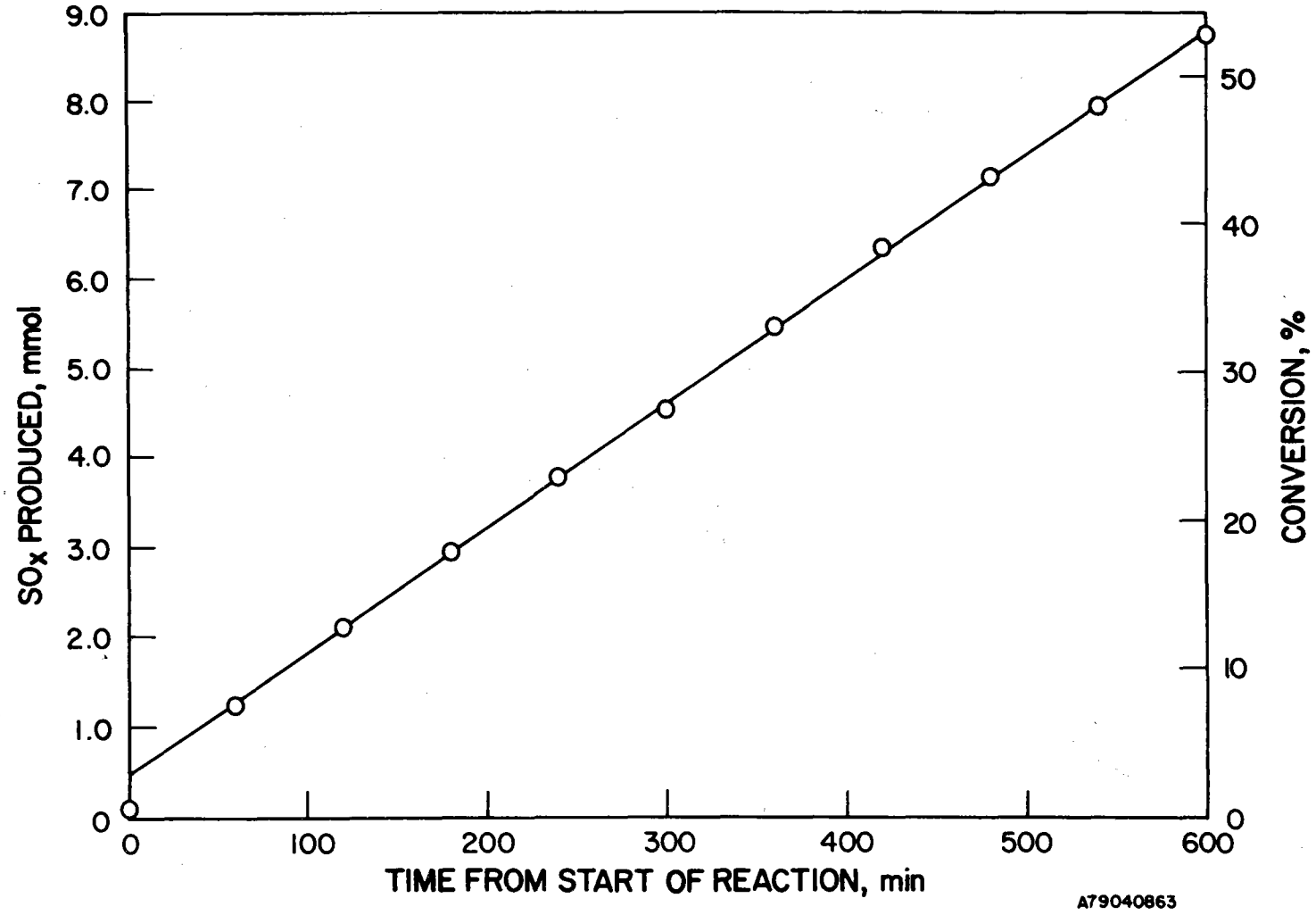

Figure 33. $SrSO_4$ DECOMPOSITION: SO_x PRODUCTION vs TIME (1723 K)

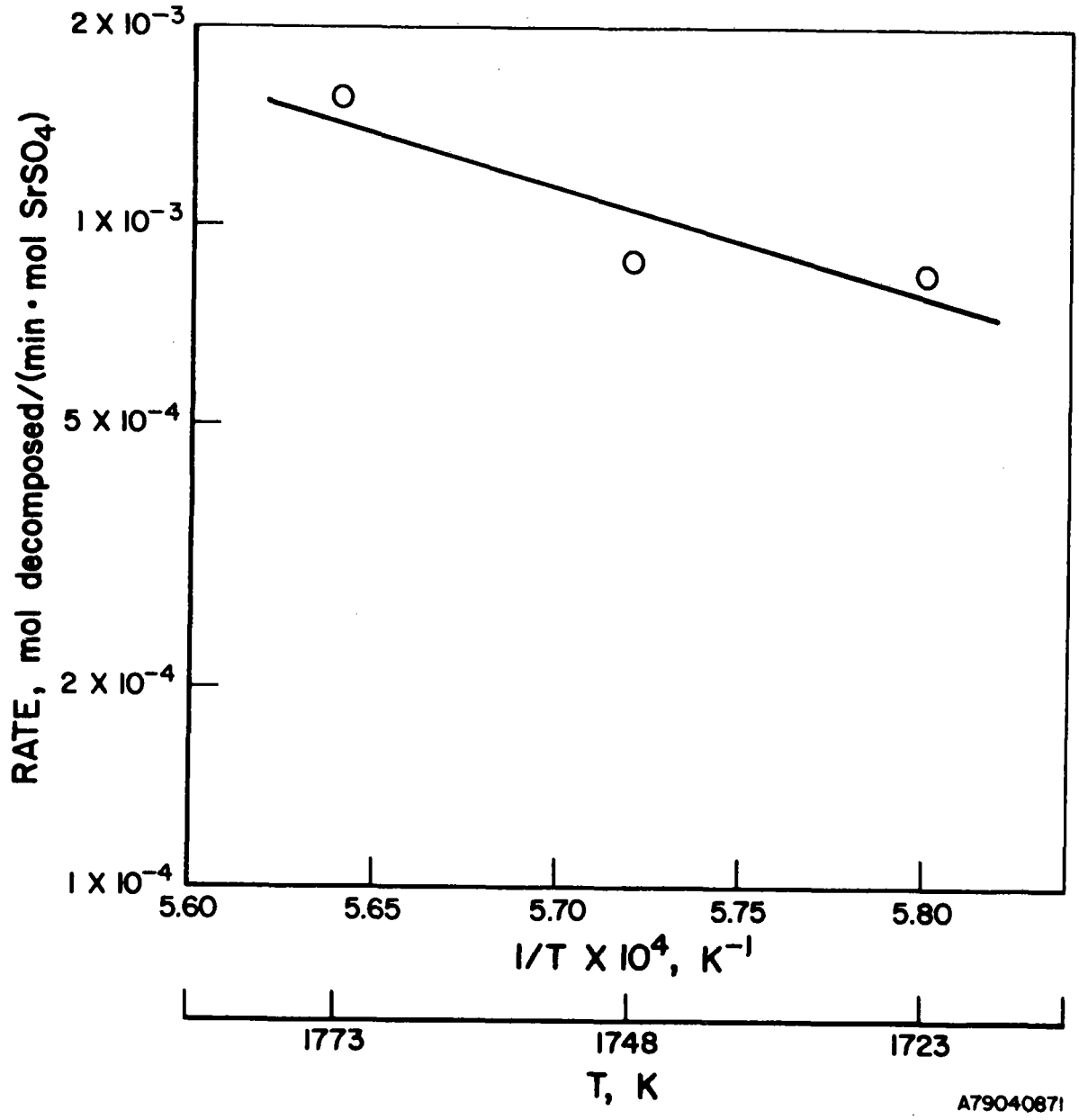

Figure 34. ARRHENIUS PLOT FOR THE $SrSO_4$ DECOMPOSITION

The fact that the rates measured are constant (zero-order) implies that reaction kinetics, rather than heat or mass transfer, controls the rate at temperatures in the range 1673 to 1773 K. If mass transfer was the rate controlling process, it should have been quite apparent considering the changes in morphology of the reactant that took place during any experiment.

By extrapolating Equation 67 to the proposed decomposition temperature (2038 K), the rate is (0.02 moles $SrSO_4$ decomposed)(min)$^{-1}$(moles $SrSO_4$ charged)$^{-1}$. This figure must be viewed with a great deal of caution, of course, because we extrapolated 250 K higher than the highest temperature at which we were able to take measurements, and because there is a phase change at 1873 K. We would not base reactor design on the data presented, but are confident that the reaction is workable at or above 2000 K.

REFERENCES CITED

1. Gahimer, J., Mazumder, M. and Pangborn, J.B., "Exeperimental Demonstration of an Iron Chloride Thermochemical Cycle for Hydrogen Production," 11th IECEC Proceedings, 933-939. New York: AIChE, 1976.

2. Konopka, A.J. and Wurm, J., "Transmission of Gaseous Hydrogen," 9th IECEC Proceedings, 405-412. New York: ASME, 1974.

3. Icerman, L., "Relative Costs of Energy Transmission for Hydrogen, Natural Gas, and Electricity," Energy Sources 1, 435-446 (1974).

4. Cox, K. E., Private Communication.

5. Broggi, A., DeBeni, G. and Van Velzen, D., "Definition and Analysis of Thermochemical Processes for Hydrogen Production Based on Iron-Chlorine Reactions," in Veziroglu, T.N., Ed., Proceedings of the 1st World Hydrogen Energy Conference, Vol. 1, 8A-69 - 8A-82. Coral Gables, Florida:

6. Farbman, G. et al., "Development of a Sulfur Cycle Water Decomposition System," 12th IECEC Proceedings, 928-932. LaGrange Park, Ill.: ANS, 1977.

7. Schuster, J. R. et al., "Development of a Sulfur-Iodine Thermochemical Water-Splitting Cycle for Hydrogen Production," 12th IECEC Proceedings, 920-927. LaGrange Park, Ill.: ANS, 1977.

8. Mellor, J. W., "A Comprehensive Treatise on Inorganic and Theoretical Chemistry, Vol. III, 234-248. London: Longmans, Green and Co., 1923.

9. Schuetz, E. H., "Hydrogen Producing Cycles Using Electricity and HXat-Hydrogen Halide Cycles: Electrolysis of HBr," Int. J. Hydrogen Energy, 4, 379-388, 1974.

10. Faita, G., Mussini, T. and Oggioni, R., "Thermodynamic Functions of Aqueous Hydrobromic Acid at Various Concentrations and Temperatures," J. Chem. Eng. Data 11, 162-165 (1966).

11. Schuetz, G. and La Londe, D., "Electrolytic Decomposition of HBr," Progress Report No. 7, 29-50. Ispra, Italy: Joint Research Center, December 1976.

12. Funk, J., "Thermodynamics of Multi-Step Water Decomposition Processes," Am. Chem. Soc. Div. Fuel Chem. 16, No. 4, 49-87 (1972).

13. Funk, J., Conger, W. and Carty, R., "Evaluation of Multi-Step Thermochemical Processes for the Production of Hydrogen From Water," in Veziroglu, T.N. Ed., Hydrogen Energy, 457-470. New York: Plenum Press, 1975.

14. Riekert, L., "The Efficiency of Energy Utilization in Chemical Processes," Chem. Eng. Sci. 29, 1613-1620 (1974)

15. Blackman, L. C., Saunders, G. and Ubbelohde, A. R., "Defect Structure and Properties of Pyrolitic Carbons," Proc. Roy. Soc. A264, 19-40 (1961).

16. Leitch, L. C., "Preparation of Concentrated Deuteriobromic Acid," J. Labelled Compd. 6, 203 (1970).

17. Puri, B. R., Sandle, N. K. and Mahijan, O. P., "Fixation of Bromine From Aqueous Solution by Outgassed Charcoals," J. Chem Soc. 4880-4884 (1963).

18. Latimer, W. H., The Oxidation States of the Elements and Their Potentials in Aqueous Solution, 2nd Ed., 33. New York: Prentice Hall, 1952.

19. Bejerano, T. and Gileadi, E., "Formation of Thick Layers of Iodine During the Anodic Oxidation of Iodide on a RDE. Part II. Open-Circuit Behavior," J. Electrochem. Soc. 124, 1720-1723 (1977).

20. Abraham, B. and Schreiner, F., "General Principles Underlying Chemical Cycles Which Thermally Decompose Water and the Elements," Ind. Eng. Chem. Fundam. 13, No. 4, 305-310 (1974).

21. Chao, R., "Thermochemical Water Decomposition Processes," Ind. Eng. Chem. Prod. Res. Dev. 13, 94-101 (1974).

22. Pangborn, J. and Sharer, J., "Analysis of Thermochemical Water-Splitting Cycles," in Veziroglu, T. N., Ed., Hydrogen Energy, 499-515. New York: Plenum Press, 1975.

23. Pangborn, J., "Laboratory Investigations on Thermochemical Hydrogen Production," in Veziroglu, T. N., Ed., Proceedings of the 1st World Hydrogen Energy Conference, Vol. 1, 7A-59. Coral Gables, Florida: University of Miami, 1976.

24. Fueki, K., "Efficiency of Thermochemical Production of Hydrogen," Int. J. Hydrogen Energy 1, 129-131 (1978).

25. Chubb, T. A., "Analysis of Gas Dissociation Solar Thermal Power System," Solar Energy 17, 129 (1975).

26. Chubb, T. A., Nemecek, J. J. and Simmons, D. E., "Application of Chemical Engineering to Large Scale Solar Energy." Solar Energy 20, 219-24 (1978).

27. Poirier, A., "One-Fourth Megawatt Solar Air Cycle Receiver." Paper presented at the DOE/DST Advanced Thermal Power Program Review, Golden, Colorado, May 9-11, 1978.

28. Biederman, N. P. and Yudow, B. D., et al., "Application Analysis of Solar Total Energy to the Residential Sector," Draft Final Report, U. S. Department of Energy Contract No. EG-77-C-04-3787, Vols. III and IV, Chicago: Institute of Gas Technology, 1978.

29. Denton, J. C., "Solar Power Systems," Energy Conversion 16, 184 (1977).

30. Office of Technology Assessment, Application of Solar Technology to Today's Energy Needs, Vol. I, 289. Washington, D. C., June 1978.

31. Grosskreutz, J. C., McBride, E. J. and Gray, D. C., "Solar Thermal Conversion to Electricity Utilizing a Central Receiver, Open Cycle Gas Turbine Design." Proc. of the 12th IECEC, 1209-17, Washington, D. C.: American Chemical Society, 1977.

32. Beverly, W. D., Engle, W. W. and Mahony, F. O., "Integration of High Temperature Thermal Energy Storage into a Solar Thermal Brayton Cycle Power Plant." Proc. of the 12th IECEC, 1195-1202, Washington, D. C.: American Chemical Society, 1977.

33. Sandia Laboratories, "Recommendations for the Conceptual Design of the Barstow, California, Solar Central Receiver Pilot Plant — Executive Summary," Sandia Laboratories Energy Report, SAND77-8035. Albuquerque, October 1977.

34. Darcey, D. M., et al., "Solar Thermal Test Facility Experiment Manual," Sandia Laboratories, SAND77-1173. Albuquerque, October 1977.

35. Reichle, L. F. C., "The Economics of Nuclear Power," Public Utilities Fortnightly 99, 24-32 (1977) February 3.

36. Blake, C., Cox, D. and Fraize, W., "Analysis of Projected Vs. Actual Costs for Nuclear and Coal-Fired Power Plants," Report by The Mitre Corporation for ERDA under Contract No. E(49-18)-2453, Report FE-2453-2, September 1976.

37. Wiggins, D. S. and Williams, J. J., "Assessment of Very High-Temperature Reactors in Process Applications. Appendix III," prepared by ORNL for ERDA, Report No. ORNL/TM-5411, April 1977.

38. Private communication with J. Ionnucci of Sandia Laboratories, November 1978.

☆U.S. GOVERNMENT PRINTING OFFICE:1980 -640 -258/ 1468